The Dissertation Committee for Federico Guido Gallo Certifies that this is the approved version of the following dissertation:

EFFECT OF ELECTRO-MECHANICAL LOADING IN METALLIC CONDUCTORS

Committee:

Krishnaswamy Ravi-Chandar,Supervisor

Mark E Mear

Sikhanda S Satapathy

Kenneth M Liechti

Chad M Landis

EFFECT OF ELECTRO-MECHANICAL LOADING IN METALLIC CONDUCTORS

by

Federico Guido Gallo, M.S.

Dissertation

Presented to the Faculty of the Graduate School of
The University of Texas at Austin
in Partial Fulfillment
of the Requirements
for the Degree of

Doctor of Philosophy

The University of Texas at Austin
December, 2010

Dedication

To my wife Mandy for inspiring and supporting me in all these years and for gifting me with our beautiful daughter Celeste.

Acknowledgements

I would first like to thank Dr. Ravi-Chandar for his tireless support and patience in assisting me in my academic and research efforts. Our interesting conversations over lunch are the highlight of my week.

I would also like to express my gratitude to Dr. Sikhanda Sataphaty for his patience and promptness in responding to my questions.

I would also like to express thanks to the following people:

To all my professors and in particular Dr. Rodin and Dr. Mear for the enthusiasm in teaching which has been an inspiration for my curiosity.

To my parents and my sister for supporting my decisions and for always considering my happiness above their personal interests.

To Robert for being a constant source of challenges and distractions in our shared love for mechanics.

To the Communion and Liberation and in particular to Jonathan, Tim, Eveline, Paolo and Elisabetta and their children Giulia and Tommaso for welcoming me in their homes and for guiding me and helping me become the person I am today.

To Chris and Mary for teaching me patience and humility.

To Daniel for being a witness of the beauty of freedom and service in living one’s life.

To the Austin CL community for looking beyond my own limitations and for allowing me to grow through their friendship.

To all the exchange students who I met at UT for allowing me to help them and in doing so to discover my love for service.

To my fellow graduate students, especially Ali, Nate, Aaron, Nicolas, Theo, Shravan and Robin for extending their friendship beyond the workplace.

To my friends across the ocean: Chris, Miky, Maria, Martino and many more for messaging me while I was typing my thesis and giving me an opportunity to delay my work.

To all the undergraduate students who had the privilege of having me as their TA over this years and in particular Ammar, Nathan, Tawnee, Henry and Dax for making me discover my love for teaching.

To Fausto, Ale, and Fabrizio for making me feel like I belong despite the distance.

Effect of Electro-Mechanical Loading in Metallic Conductors

Federico Guido Gallo, PhD

The University of Texas at Austin, 2010

Supervisor: Krishnaswamy Ravi-Chandar

The development of high powered electro-magnetic devices has generated interest in the effect of combined electromagnetic and mechanical loading of such structures. Materials used in high-current applications – aluminum alloys and copper – are subjected to heat pulses of short duration (in the range of a few hundred microseconds to a few milliseconds); immediately following or along with such heat pulses, these materials are also subjected to large mechanical forces. In previous work reported in the literature, ejection of material from the vicinity of preexisting defects such as cracks, notches or discontinuities have been observed resulting from short-duration high-intensity current pulses; after a series of pulses, permanent deformation and weakening of intact material has also been reported. But a lack of complete understanding of the effects of short duration current pulses hinders the assessment of the reliability of such conductors in high energy applications. Therefore, an investigation was undertaken to examine the behavior of electromagnetically and mechanically loaded conductors. This work investigates the effects of short-duration, high-current-density pulses in combination with mechanical loading. The aim is to develop a theoretical model to describe the resulting mechanical response. The model is to provide a characterization of the possible effects of thermally-induced plastic strains on metals loaded beyond or just below their yield strength or below the critical stress intensity factor.

In the experiments reported here, two types of specimens, undamaged and damaged, were subjected to combined electromechanical loads. Undamaged specimens were used to observe thermally-induced plastic strains - strains not caused by an increase in mechanical loading, but rather resulting from the reduction of yield strength and post-yield stiffness due to the increase in temperature. The experiments were conducted such that it would be possible to develop a model that would conclusively account for the observed material behavior. The second sets of specimens were weakened a priori by the introduction of a crack in order to study the influence of such crack-like defects on the electrical and mechanical fields, and to produce a safe design envelope with respect to the loading conditions. Failure was found to occur due to melting triggered by joule heating; a quantitative criterion based on current concentration and heat accumulation near the crack tip has been developed based on these experimental results.

Table of Contents

List of Tables

List of Figures

1. INTRODUCTION

Electrical conductors subjected to high current densities sustain significant Joule heating; when such conductors, which in some cases may contain cracks or crack-like defects, are also subjected to external mechanical loads, the combined effect could possibly result in accumulation of plastic deformation, damage accumulation, modification of mechanical properties, and in the case of cracked conductors, extension of the crack and catastrophic failure. Understanding such effects of electric current on mechanically loaded metallic conductors is important in many applications; this is especially true in rail-guns where the durability of the rails is significantly influenced by Joule heating and the growth of cracks or notches. Other applications include microelectronic circuit lines with possible defects and other structures subjected to high current densities such as high-voltage power supplies, superconducting magnets and high-current devices, where the nominal current densities are likely to be on the order of 10^8 A/m^2 or greater. Lightning strikes on some structures could also generate local current densities of this order of magnitude.

The effect of electric current on mechanically loaded metals was first reported by Soviet scientists in the late 1960's. The first such observation was reported by Kravchenko (1967), who theorized that the moving dislocations in a metal could be accelerated or decelerated by the movement of free electrons. This acceleration or deceleration is the result of impacts between the moving electrons in the current and the dislocation boundaries in the material. However, he also reported that most of the energy transmitted to the material by the moving electrons would be in the form of Joule heating and that only a small portion of the energy would be transferred into the kinetic energy of a moving dislocation. Soon thereafter, Troitskii and Rozno (1970) tested the effects of current pulses on zinc, lead, cadmium, tin and indium. They reported that applying short duration (100-150 μs) current pulses with current densities on the order of 10^9 A/m^2 to tensile specimens undergoing constant strain rate deformation ($\dot{\varepsilon} \approx 10^{-4}$ s^{-1}) generated an acceleration of plastic flow in the material. This was reportedly due to the drag-like influence of moving electrons on mobile dislocations in a plastically deforming material, which decreased the amount of energy required to further deform the material. They termed this phenomenon the “electroplastic effect” (EPE). The area of EPE became a subject of greater interest in the late 1970’s. Okazaki *et al*. (1978) reported that under constant strain rate conditions, stainless steel wires subjected to current pulses varying in intensity between 0 and 8×10^9 A/m^2 experienced stress relaxations during the pulses. In addition, they also noted that the upper envelope of the stress-strain curve was the same for both pulsed and non-pulsed specimens. They concluded that this demonstrated that the motion of the mobile dislocations observed during plastic deformation was facilitated by the presence of the current pulse. Later, they reported that the EPE depended very little on strain rate and performed tests on specimens that were forcibly cooled or very thin. Thin specimens and forced cooling were used to reduce the effects of temperature on deformation. Theoretical analyses were performed later, showing that the skin, pinch and heating effects were not sufficient to account for the stress reductions measured during current pulsing and that the remaining stress reductions must have been due to the influence of electron drag on mobile dislocations (see for example Conrad, 2002, Okazaki et al, 1979a, 1979b, 1980, Sprecher et al., 1986). Galligan and Pang (1979) performed experiments on the EPE by applying magnetic fields to pure copper and aluminum at temperatures near 0 K while plastically deforming them. These low temperatures limited not only the effects of temperature, but also phonon drag, which is negligible at these temperatures. They concluded that the electron drag experienced by mobile dislocations is independent of temperature at low temperatures. The work of Silveira *et al.* (1981) focused on the difference between electroplastic behavior under alternating current and direct current. They reported that there was a measurable EPE, even at low current densities, and that direct current produced a larger effect than alternating current. Most recently, research has been conducted to investigate the advantages of using current pulses in stainless steel wire drawing applications (Tang et al., 2000, Yao et al., 2001). These reports showed that the EPE allowed wire drawing to be done with much lower drawing forces and eliminated the need for annealing stages in the drawing process. However, using current pulses in this process also appeared to lower the ultimate tensile strength of the drawn wires. Cao *et al.* (1989) performed experiments on niobium to determine how the EPE was affected by current density and strain rate prior to current pulse application. They determined that plastic strain due to electron drag was only detectable for the larger strain rates used in their experiments ($\dot{\varepsilon} \approx 10^{-4}$ s^{-1}). However, at those strain rates, variations in the current density did have an appreciable effect. Challenging some results regarding EPE, Timsit (1981) showed, by thermodynamic calculations, that the temperature readings offered by Okazaki *et al.* (1979b) were overly conservative and therefore the effects of electroplasticity could be overstated. In addition, Goldman *et al.* (1981) conducted experiments similar to those of

Okazaki *et al.* (1978, 1979a) on superconducting lead, which does not experience Joule heating. Under these conditions, they were unable to detect any effects of electroplasticity. Bilyk et al., (2005) examined the results of Okazaki et al., (1978) and showed that a viscoplastic model was capable of reproducing most of the observed response. Considering the conflicting results reported in these studies, the effects of short duration current pulses on the life of these systems is unknown at present. Therefore, we undertook further investigation regarding the behavior of mechanically loaded conductors.

Experiments on cracked conductors reported in the literature have demonstrated that the concentration of electromagnetic energy in the vicinity of a notch or crack can result in localized melting and ejection of the metal (Finkel et al, 1977, Doelp, 1984, Satapathy et al 2005). While estimates of the stress fields, the electromagnetic fields and temperature fields can be obtained, at least through numerical simulations, three essential ingredients are missing: (i) a proper understanding of the sequence of events to be simulated (since the overall response appears to be a complex mix of mechanical deformation, electric field concentration, joule heating, heat conduction, melting and expulsion), (ii) appropriate constitutive description of the material that incorporates phase transitions such as melting and the resultant changes in the mechanical and physical material properties, and (iii) an understanding of the interaction between the mechanical and electromagnetic effects on the process of crack growth. In other words, while it has been shown in the references cited that melting occurs near the crack tip, a systematic study of the phenomenology has not been reported.

In this work, we focus on an experimentally motivated investigation of the combined effect of electromagnetic and mechanical loads on conducting materials. The objectives of our investigation include the measurement of the effects in tensile specimens of short duration current pulses and the development of a theoretical model to describe the resulting mechanical behavior in electrical conductors without and with cracks. The experiments are conducted such that it would be possible to develop a model that would conclusively account for the observed material behavior.

This thesis is organized as follows. The experimental methods used in this investigation are described in Chapter 2. This is followed by a description in Chapter 3 of the response of Al 6061-T6 and Cu-102 specimens to combined mechanical and electrical loads. In particular, the development of plastic strains is examined through direct experimental measurements. A viscoplastic model is calibrated for the materials investigated and used in Chapter 4 to generate a model of the experiment; this provides a complete description of the material response in terms of viscoplasticity. The response of conductors with cracks is discussed in Chapter 5. Specifically, motivated by experimental observations of crack tip melting, and supported by an analysis of the current field near the crack tip, a failure criterion is presented for the onset of melting near the crack tip. A failure envelope under combined mechanical and electrical loading is generated for a number of different alloys. Furthermore, issues related to scaling of the results are discussed. Finally, the conclusions are summarized in Chapter 6.

2. EXPERIMENTAL METHODS

The aim of this investigation is to develop an understanding of the response of metals and alloys to short duration high current pulses and to identify the appropriate constitutive model to capture such response. This is accomplished through careful experiments with multiple diagnostic tools that reveal the mechanical behavior and detailed numerical modeling of the response.

2.1. Material Studied

The main materials considered in this work are Al 6061-T6 and Cu 102; in some special cases, a few other alloys have been examined. These materials were selected because of their widespread use in electrical applications and in rail-guns. Both materials have similar basic mechanical properties; at about 24 C their yield strength is around 276 MPa and they both display low hardening as shown in Figure 2.1.

Despite this similarity in mechanical properties, these metals present strong differences in electrical and thermal properties; a complete set of the most relevant properties for both materials is listed in Table 2.1. Copper displays lower electrical resistivity, and higher melting temperature and thermal conductivity than the aluminum alloy and is usually preferred as an electrical conductor. On the other hand, the density of copper is three times greater than that of aluminum and this makes it unattractive in structural applications. For the rail-gun applications, where one experiences combined mechanical and electrical loading, it is important to study the coupled effect on the deformation and structural response.

One outcome of the coupling between the mechanical and electrical loading is that the properties of both metals are a function of temperature and most of the limitations in using these materials derive from the large drop in properties with such coupling. First, there is a significant drop in yield strength with increase in temperatures; the magnitude of the drop can be found from isothermal stress strain curves. The yield strength obtained from those curves at various temperatures are shown in Figure 2.2 while the complete set of curves is reported in Appendix II. These data show that the yield stress of both aluminum and copper decays rapidly past 400 K. Second, the electrical resistivity depends nearly linearly on temperature until close to melting; at this point the resistivity increases more rapidly. The linear portion of this dependence can be written as $\Omega_{(T)} = \Omega_0 \left(1 + k\Delta T\right)$ where k is the gain factor and is a material property (Simmons and Baluffi, 1959); this quantity is ~0.0043 for both materials (NDT Resource Center, 2010). Despite the slow increase in resistivity given by this factor, it can have a large impact on Joule heating and has to be included in the analysis.

Experiments involving combined electrical and mechanical loading present many significant challenges: first, since an electrical current is discharged through the specimen material, adequate electrical insulation between the mechanical loading device and the specimen is required to prevent damage to the mechanical loading frame and its electronic instrumentation. The specimen has to be designed with tabs to facilitate connection to the power supply. Second, the electrical current generates a magnetic field that interacts with the conductor, producing Lorentz's force; this force must be reacted appropriately to ensure uniaxial loading conditions in the specimen. Third, the current

Table 2.1. Physical and mechanical properties of Al 6061-T6 and Cu-102*

Constants	**Al 6061-T6**	**Cu-102**	**Units**
Young's Modulus – E	70	104	GPa
Yield Stress – σ_Y	300	280	MPa
Specific Heat – C_p	899	385	J/(kg K)
Thermal Conductivity – k	167	391	W/m-K
Coeff. of Thermal Expansion	24	17	µm/m-K
Density – ρ	2700	8900	kg/m^3
Resistivity – Ω	3.99E-08	1.73E-08	ohm-m
Melting Temperature - T_M	855	1356	K
Fracture Toughness – K_c	21.4	19.2	MPa m$^{1/2}$

* Fracture toughness values were measured in this work; all other material properties are taken from www.matweb.com.

and electromagnetic field interact with the measuring system – especially when contact probes are used – and a special set of non-contact devices is needed to measure the electrical and mechanical fields.

An experimental arrangement that overcomes those challenges has been designed and used in this work; the details of this design follow.

2.2. Mechanical Loading Apparatus

A special set of fixtures was designed to insulate the custom built loading system from currents of up to 100 kA that flow through the specimen. The custom load frame was deemed necessary to prevent the large magnetic field from interacting with any circuitry. In fact, in a regular Instron machine the motion of the crosshead is controlled by a computer through microelectronics sensors and electrical actuators; even if those devices are insulated, large interferences were registered during medium intensity pulses, prompting the change to the custom-built load frame. The design chosen was a manual loading frame with an ACME threaded screw connected to the crosshead through a set of conical bearings. This configuration allows for minimal compliance once the bearings are preloaded and allows for the crosshead to be locked in place at a desired position with a locknut. The geometry of this device is shown in Figure 2.3.

The fixture for attaching the specimen to the loading frame is composed of two blocks of steel bolted together in order to produce the necessary pressure and therefore friction to transfer loads to the specimen (Figure 2.4a). Due to the thin section of the specimen, the load carried by the grips is relatively low - in the range of 100 to 200 lb. These grips are subsequently bolted to a base connector. This connector is a standard Instron coupling, allowing the grips to be mounted on a standard Instron loading frame when electric insulation is not needed. To provide electrical insulation, a special coaxial mechanism shown in Figure 2.4b was designed. This is made of three parts: an external steel sleeve, ceramic insulators and a load bolt. The inner part of the sleeve was also lined with mylar film to prevent any arcing. In this mechanism, the ceramic cylinders are loaded axially between the bolt and the sleeve, allowing high load transfer capabilities while maintaining electrical insulation and minimizing compliance.

The load bolt arrangement was chosen to provide a direct reading of the forces on the specimen; the double reading arrangement allows for dynamic measurement of the load on either side of the specimen when necessary. The signal from the load bolts are processed through a Vishay model 2210 strain-gage signal conditioner and the readings are recorded on a Tektronix TDS 420 digital oscilloscope for short time at a high sampling rate of 25000 samples per second. To obtain longer measurement times a desktop computer combined with a National Instruments Data Acquisition Card PC-MIO-16E was used to record the signal at a rate of 200 samples per second.

2.3. Power Supply and Current Measurement

A capacitor bank capable of sustaining a 20 kV potential was used to generate the short duration current pulses sent into the specimen. The bank is composed of 11 capacitors (25 µF, 20 kV rating, Maxwell Series C High Energy Capacitors, Model: 33506) connected in a transmission line circuit with inductors (≈5 µH each) as shown in Figure 2.5. A charging power supply (Lambda 152A-20KV-POS) and a safety dump circuit complete the pulse power supply. The whole system was wired so as to be operated remotely with the option of an automated charging procedure through a LabView computer program, or by a remote control station operated manually. The leads of the capacitor were then connected to the specimen through copper wiring and separated by an Ignitron-Thyraton fast switch system that was used to dump the current through the specimen quickly. This device is an insulated, sealed container with a pool of mercury; when a small current is applied at its lower end the mercury evaporates creating a bridge between the poles of the switch. At this point the current running through it keeps the mercury in temperature allowing the poles to remain connected. When the current drops below a certain threshold the mercury cools down and is redeposited at the bottom of the cell; this breaks the circuit.

In order to measure the current passing through the circuit it was necessary to rely on an indirect reading method, because the high currents running through the specimen would damage any instrument in direct contact. The Rogovski coil provides a simple method of indirect current measurement by utilizing a toroidal winding around a metal core (Figure 2.6a). This coil was placed around one of the feeding wires of the pulsed power supply to provide current measurements. The induced voltage in the Rogovski coil is independent of the location of the feeding wire within the toroid and is proportional to the rate of change of current in the conductor; a typical output from the Rogovski coil is shown in Figure 2.6b. Integration of this signal results in an estimate of the current passing through the specimen.

Direct integration of the Rogovski coil output provides the actual value of current once a proper calibration constant is found; such a constant is found discharging a single capacitor through a test resistor and computing the Rogovski signal properties such as frequency and damping coefficient. Due to the simplified circuit it is possible to compute the theoretical current using the parameters found with this test; therefore the calibration constant is the ratio between the current found through direct integration and the calculated value. The procedure is repeated at various charging voltage and the average of the calibration constants is found in order to increase accuracy. For the coil used in this work, the calibration factor is 3.15×10^{7} A/V. The time variation of the current obtained from discharging the capacitor bank is shown in Figure 2.7a; it can be expressed as a simple damped sine wave:

$$j^{\infty}(t) = j_{\max}^{\infty} e^{-\zeta \omega t} \sin\left(\omega t + \phi\right) \tag{2.1}$$

where ω, the natural frequency of the pulse power supply, ϕ the phase angle and ζ, the nondimensional damping ratio, are chosen to fit the actual coil signal shown in Figure 2.7a. For the particular power supply used in the present study, $f = \omega / \left(2\pi\right) = 4.4$ kHz and $\zeta = 0.06$. The amplitude $j_{\max}^{\infty}$ determines the maximum current intensity of the sinusoidal pulse and is the quantity that is varied from one experiment to another. The largest $j_{\max}^{\infty}$ used in the present work was 42 kA[1]; for specimens with a cross-sectional area of 2.58 mm^2 this corresponds to a peak current density of 1.6×10^{10} A/m^2. This value is within the range of current desities obtained in railguns, microelectronic circuits, superconducting devices and other applications.

An important aspect of current propagation through a conductor is geometric dispersion. At high frequencies, current is carried through a thin layer near the surfaces of the conductor; this is referred to as the "skin-effect". The distance over which the current density falls to 1/e of its original value is called the skin depth δ and can be calculated as follows (Jackson, 1987):

$$\delta = \sqrt{\frac{2\Omega}{\omega \mu_0 \mu_r}} \tag{2.2}$$

---

[1] In some tests on large specimens, a special power supply at the Institute for Advanced Technology delivering 200 kA was used; this was an overdamped system and the details are provided in Section 5.3.

where Ω is the material resistivity, ω is the frequency of the current, μ_0 is the permeability of free space ($4\pi \times 10^{-7}$ N/A^2) and μ_r is the relative permeability of the conductor. For the 4.4 kHz current pulse shown in Figure 2.7, the skin depth was calculated to be 1.5 mm for aluminum and 1 mm for copper; since the skin depth is larger than the thickness of the specimen used in the experiments, the current can be considered to be uniformly distributed across the cross-section of the specimens.

Determination of the temperature of the specimen is an important issue because Joule heating and the associated thermal expansion alter the mechanical response significantly; however, attempts to make measurements of the temperature with non contact infrared probes were not successful due to complications arising from electromagnetic interference from the pulse discharge. Therefore, the temperature was estimated by simply calculating the Joule heating from the current pulse. Thus, integrating the current signal in Figure 2.7a one more time and using Joule's law relating the current to the change in temperature through material constants (resistivity, cross sectional area, density and specific heat) the temperature of the specimen as a function of time was determined to be:

$$T(t) = \frac{1}{A^2 \rho C_P} \int \Omega(t) I^2(t) dt \tag{2.3}$$

An estimate of the temperature variation with time is shown in Figure 2.7b for a Cu-102 specimen; a temperature rise of ~170 K is observed in this case. For the highest $j_{\max}^{\infty}$ used in the present work, the maximum temperature reached was ~640 K for both materials. This is $0.6T_M$ for aluminum and $0.5T_M$ for copper.

This approach to temperature calculation is valid for short duration pulses where heat transfer can be neglected. It is important to note that the resistivity of the material is a function of temperature as well; this becomes more relevant as higher temperatures. Omitting this dependence leads to an erroneously low estimate of the maximum temperature achieved and may cause an overly conservative estimate of the contribution of viscoplasticity. The above calculations were validated during the experiments by measuring the thermal strain right after the discharge in the case where no plastic strain was recorded, and equating it to the expected value.

Following the discharge, the specimen cooled down in ambient conditions over a few seconds; for this portion, the temperature variation was estimated from the load and strain readings and it was found that it can be modeled quite well by a logarithmic decay.

$$T(t) = T_{\max}\left(1 - \frac{1}{\ln(5)}\ln(t + 0.7)\right) \quad \text{for} \quad 0.3s \le t \le 3s \qquad (2.4)$$

Due to the specimen geometry, when the current flows through the specimen, the central portion of the conductor experiences Lorentz's forces as illustrated in Figure 2.8a, which cause the specimen to bend out of plane. A backing mechanism is provided to react this force and to ensure that the specimen is loaded axially during the test as shown in Figure 2.8b. The backing plate is connected solely to the upper portion of the mount to ensure that no load is carried by this mechanism.

2.4. Digital Image Correlation Technique

Due to the high current and electromagnetic fields generated by the discharges it was not possible to mount strain gauges to the specimen. Therefore, the digital image correlation (DIC) method was adopted (Sutton, 2008). This technique enables a direct measurement of the displacement field on the surface of an object with high accuracy. Due to the small thickness of the specimens it is safe to assume that this surface reading is representative of the displacement fields averaged through the thickness. DIC consists in comparing two digital images of the specimen one taken at the unloaded state and the other at different loading/displacement conditions and computing the variation in positioning of a pattern on its surface.

For this technique to work properly the specimen has to be coated with a randomly generated speckle pattern as shown in Figure 2.9 so that motions of the speckle can be detected. In this case, this pattern was generated by lightly spray painting the specimens with thermally resistive paint; this choice was dictated by the high temperatures reached during the discharge. The reference frame used for all of the pictures is the position of the camera, which is considered fixed at all times. This choice allows for a rigid body motion of the specimen to appear in the readings; however, the average strains can be obtained by post-processing the displacement field, and eliminating any rigid rotation and translation. To perform this correlation a third-party software called ARAMIS was used to optimize the processing time. The advantage of this software is its automated pre and post processing interfaces, which allow evaluation of a large number of pictures in a short time.

The only downside of this technique is that its accuracy depends on the pattern size and quality, and on the picture resolution and quality; however, this quantity can be evaluated by comparing two identical snapshots and computing the strain field. If the average strain – which should be zero – is less than 0.0001 accurate estimate of the strain is guaranteed. In order to time resolve the strain measurements, a Phantom v7.3 high speed video camera with a Nikon macro zoom lens was used to sample the digital images at twenty-thousand samples per second with a picture size of 256 pixels in the axial direction and 128 pixels across giving a resolution of 1 pixel per 0.001 in.

All the pictures were correlated to the one taken right before the discharge occurred, giving the strain variation from the state immediately preceding discharge. This choice was made to achieve higher accuracy in the calculation of the absolute strain due to the comparison with the initial picture which avoids accumulations of error with a large number of pictures. A typical result of this scheme is shown in Figure 2.10 where the displacement is monitored by DIC during a current discharge and subsequent cooling. Observing the images it is clear that the vertical displacement field is linear, resulting in a constant strain field along the axis of the specimen. This was to be expected due to the uniaxial nature of the test; to simplify the strain calculation a linear fit of the vertical displacement field was obtained and the slope was used as the measured strain. These strain measurements turn out to be extremely important in identifying the material response as discussed in the subsequent sections.

Some more observations must be made on the limitations of this technique; first to resolve the speckled pattern better, the images need strong contrast; this limits the minimum shutter opening time and the highest sampling rate. Furthermore the high power lamps used to illuminate the specimen caused a significant increase in temperature which required the installation of a cooling fan to achieve a steady state before the experiment. All this can be improved using a better camera and set of lenses to increase the amount of light collected by the CCD.

2.5. LabView Automated Program

In order to achieve a complete set of readings during the discharge which lasts no more than two milliseconds, a LabView program was developed capable of triggering the high speed camera, the oscilloscope to record the load and the electrical discharge system. The flow diagram for control of the experiment is shown in Figure 2.11. To meet those requirements a PCI-MIO 16E has been used combined with a desktop computer; LabView was chosen as the coding language for the compatibility with the measuring instrumentation, the variety of dedicated libraries which allow for a simpler connection to the above mentioned device and for the possibility to carry out multiple operations in parallel.

Limits for the setup are set by the low response speed and memory of the computer and by the rate of data exchanged in between the DAQ and the desktop itself which did not allow for sampling rates greater than 200 samples per second of the load. The DAQ card used is equipped with 16 analog inputs, 2 analog outputs with variable range and 16 digital I/O working on a saturation voltage of 5 V. For this part of the experiment two analog input channels were used to monitor the load bolts signal and two digital outputs were used to trigger the high speed camera and the ignitron.

The program itself is divided in three parts; first it simply monitors at 10 samples per second the load cell signal during the specimen loading phase, allowing visualization of the specimen conditions in real time and estimation of the maximum load and strain reached. At the end of this stage, the grip displacement was fixed and the load train was allowed to reach a steady state; the data for this part was saved containing all the loading process information. The second stage consisted in charging the capacitor bank; through a relay system incorporated in the control station, the LabView program was able to control charging of the bank of capacitors to a preset voltage level, enabling a fully automated experimental procedure.

The third stage is the discharge procedure. At fixed grip displacement the load signal is recorded for approximately ten seconds. One second after the initiation of the recording procedure a single 10 V pulse is sent to the camera to start the picture capturing sequence which lasts approximately two seconds with a sampling rate of 20000 samples per second. Three hundred milliseconds later, another pulse is sent to the ignitron to trigger the electrical discharge through the specimen. The current flowing through the circuit triggers the oscilloscopes which record the Rogovski coil signal for 2 milliseconds at 200 thousand samples per second, and the load bolts signal for two seconds at forty-thousand samples per second. After the load has been recorded, the Rogovski coil output and load bolt output data files are saved. The high speed images are downloaded to the computer for further analysis. Note that this procedure may be repeated to obtain multiple discharges through the same specimen.

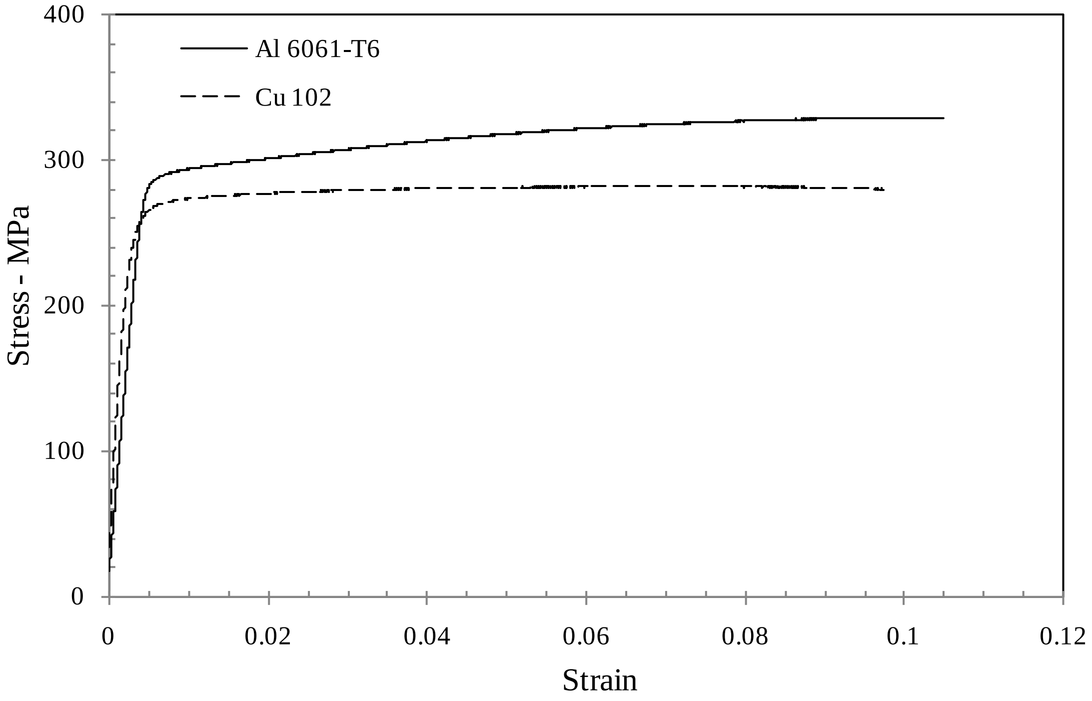

Figure 2.1. Stress-strain curves for Al 6061-T6 and Cu-102.

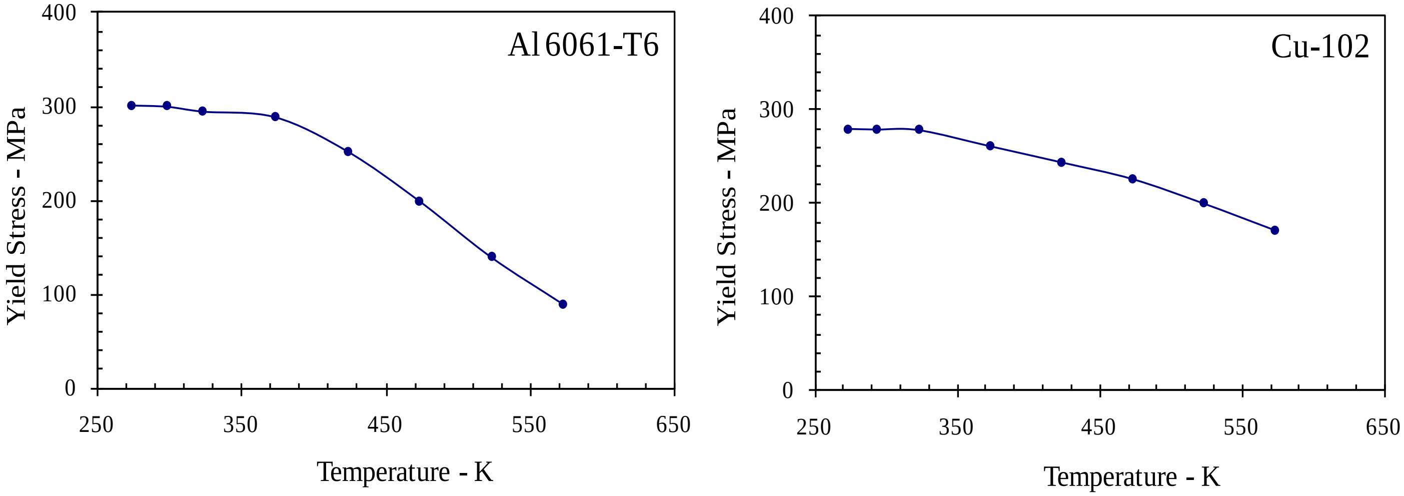

Figure 2.2. Yield stress as a function of temperature for Al 6061-T6 and Cu-102.

Figure 2.3. Images showing front and side views of the loading frame. The crosshead is moved by turning the handle connected to the ACME threaded screw.

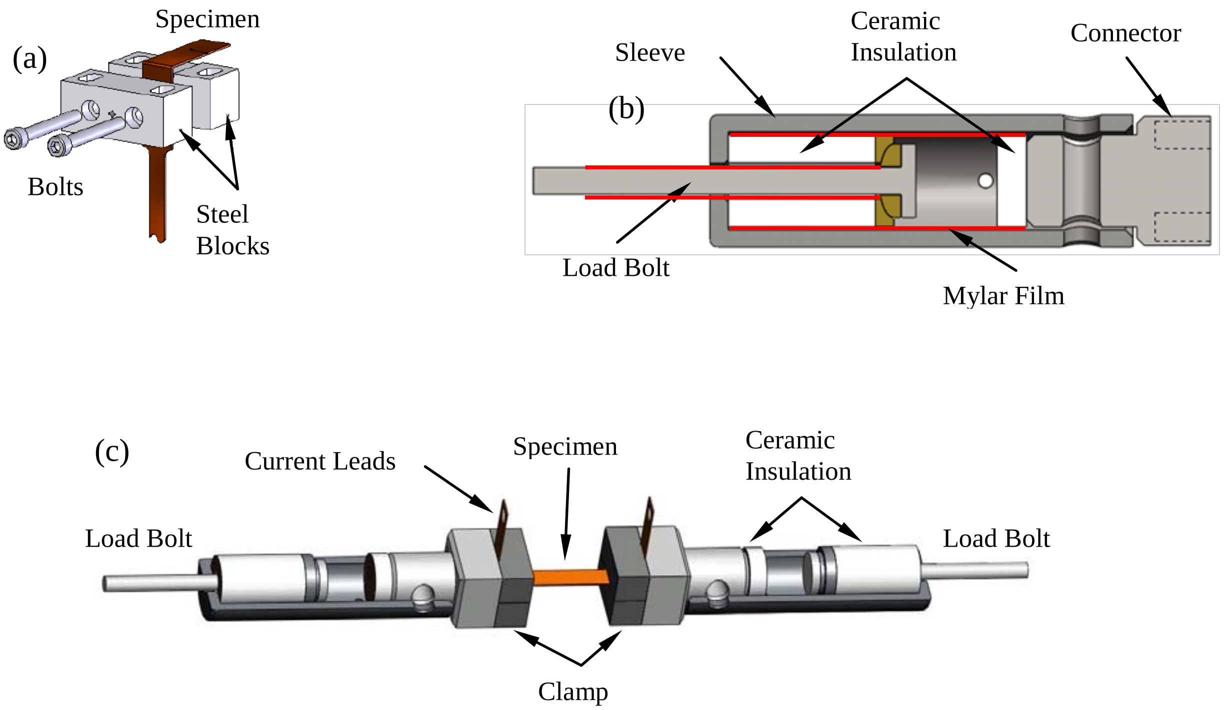

Figure 2.4. Schematic diagram of the specimen with details of mechanical clamping and electrical connections.

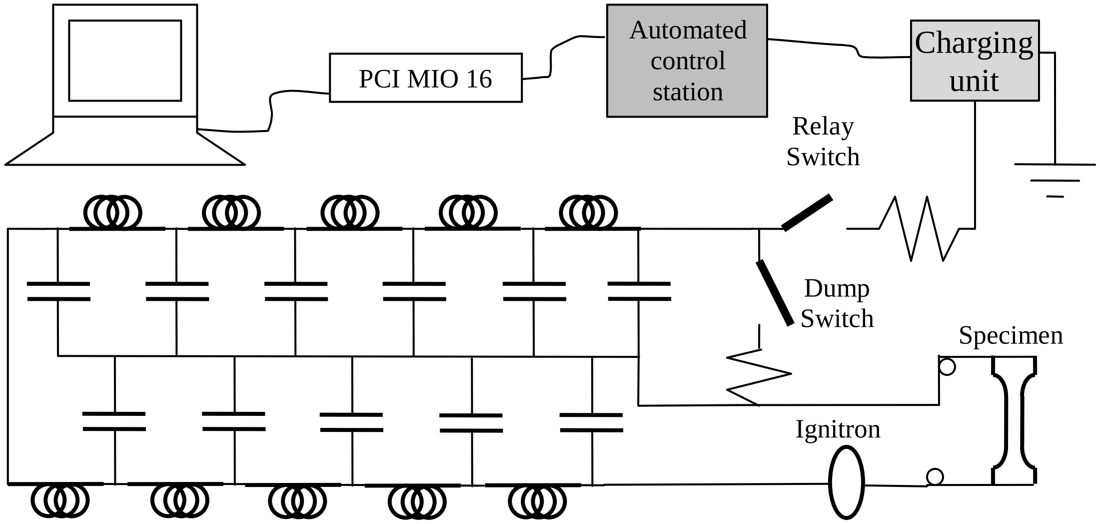

Figure 2.5. Schematic representation of the capacitor bank wiring along with the loading and discharging mechanism. The system is controlled by a personal computer through a National Instrument Data Acquisition Card.

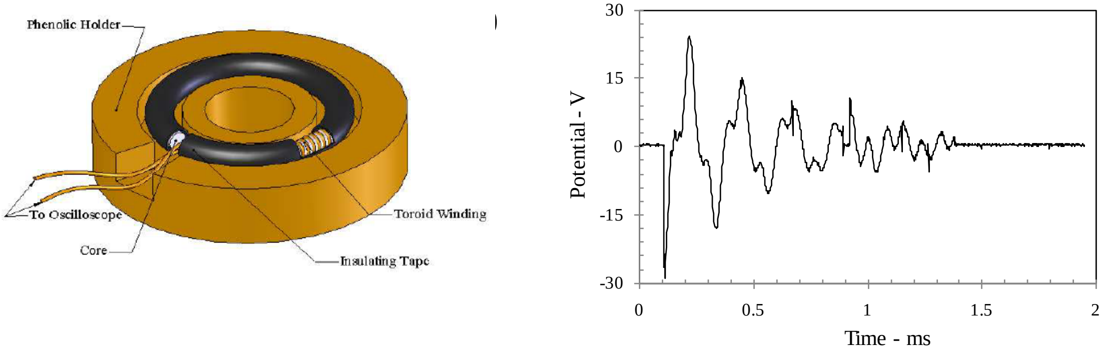

Figure 2.6. Rogovski coil assembly (a), and typical output (b) are shown.

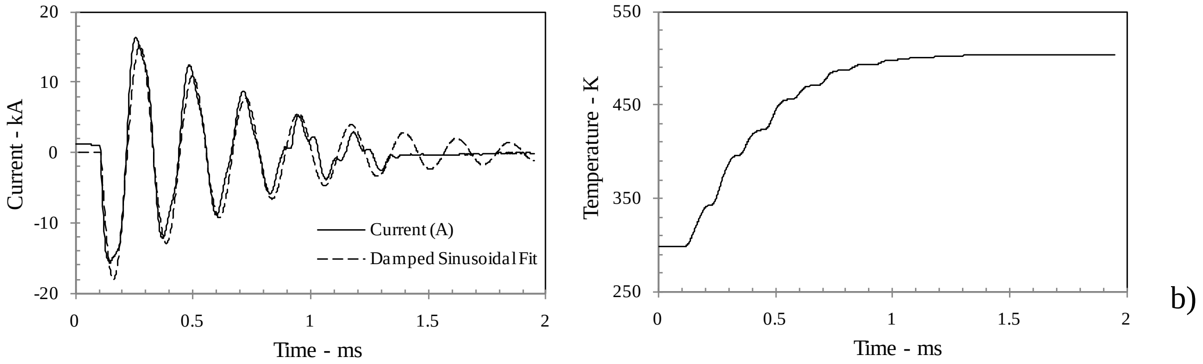

Figure 2.7. Current (a) and temperature (b) variation with time obtained from the Rogovski coil signal.

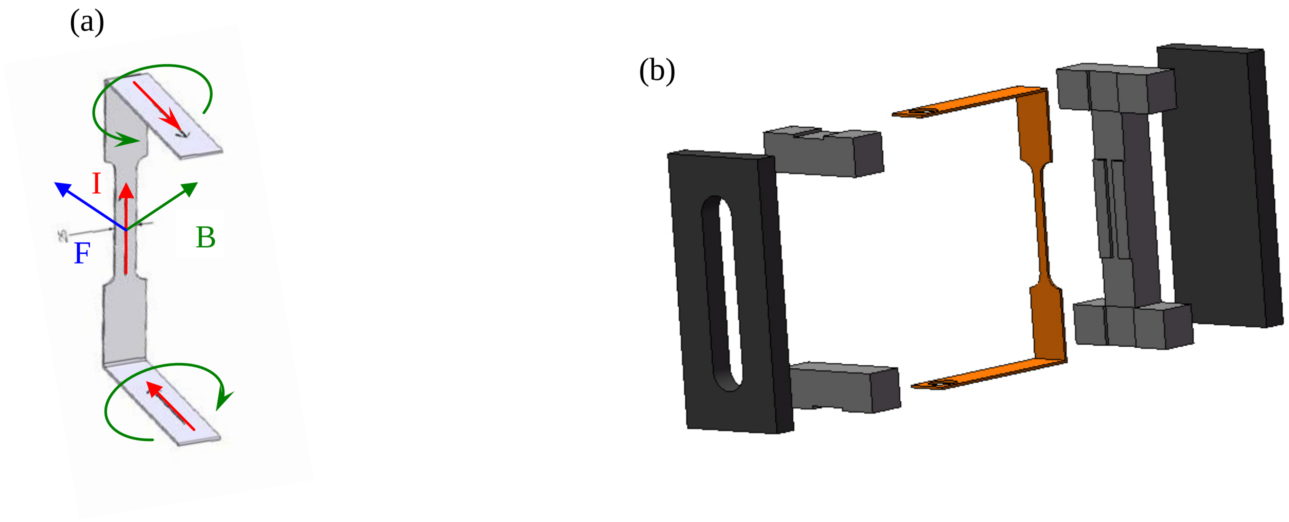

Figure 2.8. (a) Electromagnetic field interaction in the dog bone specimen. The resulting Lorentz force on the specimen is indicated. (b) A drawing of the support used to react the Lorentz force and prevent bending.

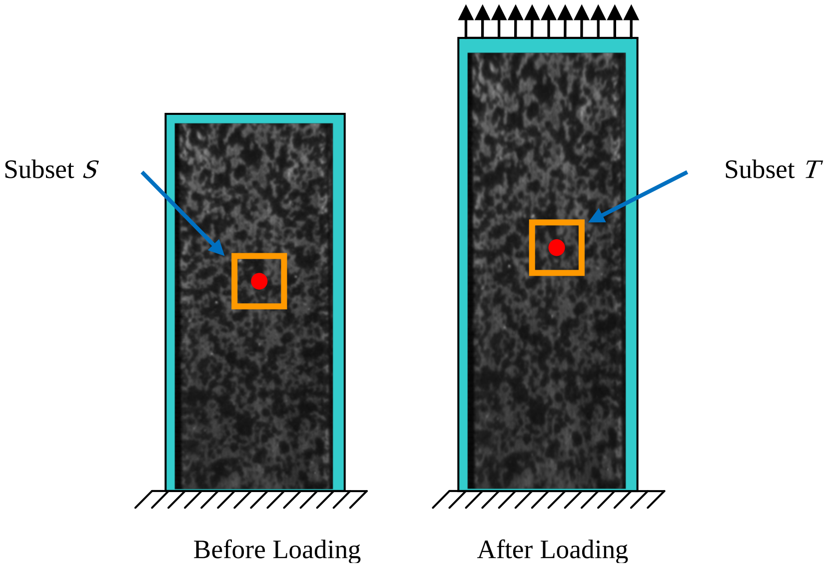

Figure 2.9. Images of the specimen with a speckle pattern in the undeformed and strained state.

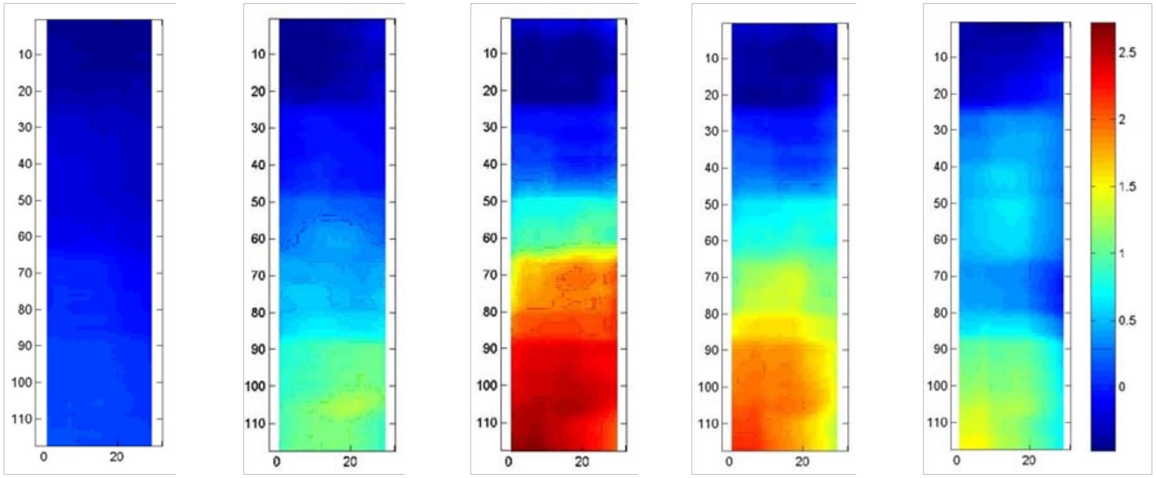

0.5 ms 1 ms 2 ms 1 s 3 s

Figure 2.10. Displacement field determined from digital image correlation. Scale bar indicates displacement level in pixels. The initial heating (0 – 2 ms) and the subsequent cooling over 3 s can be observed in these images.

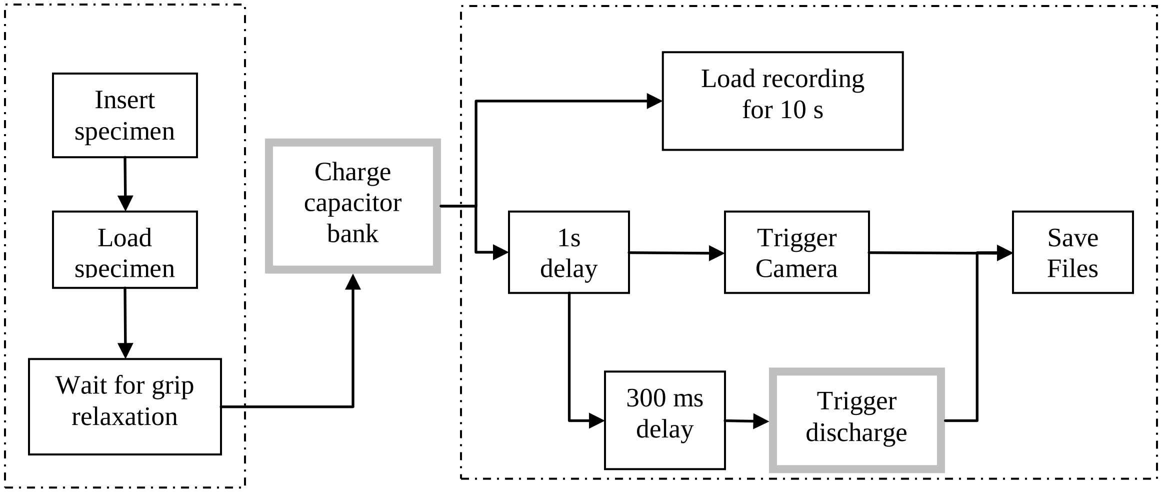

Figure 2.11. Block diagram for control of single pulse discharge.

3. EFFECT OF PULSED CURRENT THROUGH A PRISTINE CONDUCTOR

The response of Al 6061-T6 and Cu-102 to current pulses under constant displacement and constant load conditions are examined in this chapter.

3.1. Single Current Pulse with Fixed Grip Loading

The results of subjecting the specimens to a single current pulse at fixed grip loading are examined first.

3.1.1. ELASTIC LOADING

The first test performed was to discharge a low current through a specimen loaded below the yield stress. The material used was Al 6061-T6. The test was conducted following the procedure described above and the resulting load variation with time is presented in Figure 3.1. The stress in the specimen was increased to about 200 MPa and allowed to settle down as indicated in this figure. After about 20 seconds the capacitors were discharged through the specimen, generating a nearly sinusoidal current pulse with $j_{\max}^{\infty} = 8.3 \times 10^{9}$ A/m^2 as indicated in Figure 2.7a. As expected, the metal heats up to a temperature of 470 K and the load drops as a consequence of the thermal expansion. Under these conditions, the expected strain due to thermal expansion was 0.0041 and the elastic recovery due to the load drop is 0.001. Once the discharge stops after 2 milliseconds, the specimen cools down, and as seen in Figure 3.1, the load recovers completely over a time scale of about 10 s.

The axial strain obtained from the DIC measurement is shown in Figure 3.2. Note that time is plotted on a logarithmic scale in order to show both the short-time and long-time response. It is noted that the strain increased rapidly (in less than 2 ms) due to thermal expansion associated with the Joule heating. This is the duration over which the load drops, but this is not resolved in the load bolt measurement due to electromagnetic interference. The time variation of the calculated from the load measured by the load bolt is shown in Figure 3.3. Note that the sharp drop in load during the first 2 ms is not captured because the interference from the large electromagnetic fields associated with the discharge disrupts the measurement, but because of thermal expansion, the stress in the specimen drops to ~40 MPa, then oscillates for about 30 ms and then increases during specimen cooling to the initial stress level of 172 MPa. Figures 3.2 and 3.3 are independent measurements of the stress and strain variation with time and correlate very well with each other. Due to the memory limitation of the high speed camera, only the first 1.4 seconds of the strain history were recorded; to complement this set of images, one final image was obtained at about 10 s after the current pulse. This image, when correlated with the initial image, provides the total strain a long time after the pulse discharge; the strain calculated at 10 seconds after discharge is shown in Figure 3.5 as a filled circular symbol.

The rapid unloading associated with this thermal expansion is similar to an impulse loading on the specimen and hence, this causes an oscillatory dynamic oscillatory response of the entire system at its natural frequency for the next 30 ms; this oscillation is seen clearly in both the stain and stress measurements. This is followed by a slow cooling of the specimen, and an associated shrinking of the specimen. Since the specimen remained below the plastic threshold during the entire test, complete recovery of the thermal strain was observed; this test result was used to calibrate the temperature from Rogovski coil measurement of the current. A similar thermoelastic response was observed in the Cu-102 specimens.

To test the effect of higher currents the specimen was pulsed with larger energies but no plastic accumulation was found. One specimen was tested with a current with $j_{\max}^{\infty}$ of 10^{10} A/m^2; the thermal expansion was large enough to cause the specimen to buckle out of plane. Due to this limitation no further testing was performed for higher current densities. With this elastic test, we have established the reliability of the test methodology to provide reliable measurements of the response of materials to combined mechanical and electrical inputs. It is important to note that there is a 2 ms heating time, with associated thermal strain, a 20 – 300 ms period during which high temperatures persist, with dynamic oscillations during the initial part of this period, and finally, a slow cool-down period of about 10 s. The characterization of the viscoplastic response of these materials is considered next by increasing the applied stress above the yield point and subjecting the materials to different levels of current pulses.

3.1.2. PLASTIC LOADING

Next, the same test was repeated, but with a higher initial loading; this time, in fact, the Al 6061-T6 specimen was loaded past yielding, to a stress level of 300 MPa. The procedure followed was the same of the previous test: first the specimen was loaded in the plastic range and then the system was allowed to settle down. Finally a current pulse was discharged through the specimen; as a result, the specimen temperature increased to 500 K. The variation of the stress and the strain measured with DIC are shown in Figures 3.4 and 3.5. The strain history measured with DIC is shown in Figure 3.5; the noise in this signal was eliminated by processing the data through a low pass filter. The filtered signal is also shown in Figure 3.5; from now on only the filtered strain measurement will be shown for clarity. The residual strain is indicated by the filled circle symbol in Figure 3.5.

Comparing the plot of the stress and strain variation with time with the fully elastic case shown in Figure 3.2, no major differences are evident except that upon cooling, the strain does not recover, leaving a permanent plastic strain of about 0.001. The results of a second test, performed with a larger temperature increase to 580 K are shown in Figures 3.6 and 3.7; in this case, the plastic strain accumulation was 0.004. Comparing the load variation in Figures 3.4 and 3.6, it is clear that there is a significant load drop in the latter, while a load drop is not observed in the former. We attribute this to differences in the compliance of the load train; the two beveled washers placed in line of the load train are thought to be responsible for such unpredictable differences. We will not rely on the load measurements in the sequel and instead focus attention on the accumulation of plastic strain.

Two tests were performed on a Cu-102 specimen with similar results. Temperatures of 420 K and 600 K were reached in these tests. The time variation of the stress and the strain are shown in Figures 3.8 and 3.9, and Figures 3.10 and 3.11, respectively for the two tests. The response is similar to that seen for the Al 6061-T6; note once again that there is a permanent strain of about 0.0005 and 0.0025 respectively for the two different temperatures.

The accumulation of plastic strain in the gage section during the pulse heating and cooling cycle implies that some permanent deformation must have occurred at some time between the pulse discharge and the cooling phase. The permanent strain accumulation during the short current pulse discharge is modeled in Section 4 with a viscoplastic constitutive model.

3.2. Multiple Current Pulses with Fixed Grip Loading

In order to investigate the strain accumulation behavior further and to determine the limiting behavior of the material under repeated pulses, a series of consecutive pulses of the same current density were discharged through the same specimen, maintaining the cross-head position unchanged between discharges. The specimen was allowed to cool down to room temperature between each discharge. First, the results for the copper specimen are discussed; this is followed by the response of the aluminum specimens that appear to be a bit more complex.

The first set of experiments consisted of pulsing two Cu-102 specimens four times each at the same current levels, with $j_{\max}^{\infty}$ of 6×10^9 and 8.7×10^9 kA/m^2 (T = 420 K and T = 600 K) and initial load of 270 MPa in both cases. The time variation of the load and strain for all the discharges are shown in Figures 3.12 and 3.14 and Figures 3.13 and 3.15 respectively; the residual strain accumulated at the end of each load cycle is shown by the symbols at 10 s. From these strain histories, it is apparent that the specimen accumulated a permanent strain of 0.006 during the first discharge, but the subsequent discharges did not provide any increment in the permanent strain, with the specimen returning to its initial state upon cooling. In contrast, the variation of the load with time, shown in Figures 3.12 and 3.14, exhibits a drop with each subsequent pulse of the current; as discussed earlier, we attribute this to compliance effects in the loading system and will return to this issue when we examine dead-load experiments in Section 3.3. It is important to note that the direct measurements of strain are absolutely essential in identifying the source of the load drop; in the absence of such local measurements, the global load drop would have been attributed to the specimen and would distort possible theoretical modeling efforts.

Similar experiments were performed on the Al 6061-T6 specimens, with temperatures reaching 500 K and 580 K and an initial load of 300 MPa. The time variation of the load and strain for all the discharges are shown in Figures 3.16 and 3.18 and Figures 3.17 and 3.19 respectively; the residual strain accumulated at the end of each load cycle is shown by the symbols at 10 s. The strain variation displays the same general behavior as seen so far consisting in a rapid expansion followed by decaying oscillations and a partial strain recovery. However, there appears a crucial difference from the behavior of Cu-102: plastic deformation continues to accumulate in subsequent cycles, without saturation. We will explore this further through the viscoplastic model and additional experimental investigations.

3.3. Single Current Pulse at Constant Load

As discussed in the previous section, under repeated pulse currents, the accumulation of plastic deformation was easily and appropriately identified by local measurements using DIC, but the associated load/stress drop was clouded by effects associated with the compliance of the loading system. In order to verify the validity of the model under different loading conditions and to remove any uncertainties related to compliance, a second series of tests was performed, this time under constant load. The constant load condition was obtained by hanging a calibrated weight from the bottom end of the loading fixture described in Section 2.2. In this way, a constant load level was assured throughout the discharge, except for possible dynamic effects of the system which generates an oscillation of the load experienced by the specimen.

The stress applied to the Al and Cu specimens was set to 138, 172, 206 and 242 MPa, and current pulse discharges with the charge voltage in the range of 3 to 6 kV in steps of 0.5 kV that cause maximum temperatures of 330 K to 670 K in steps of ~50K were applied to the specimen; the highest charge level resulted in failure of the specimen. The experimental procedure in described in Section 2.4 was repeated to evaluate the behavior of the specimen, with the exception being that the loading was by a weight hanging from the bottom grip fixture. In the case of multiple pulse tests, the duration of cooling between tests was long enough to allow the specimen to cool down to ambient temperature completely.

For the first test, a copper specimen was loaded to 172 MPa and a current discharge of $j_{\max}^{\infty} = 5.5\times10^{9}\,\mathrm{A/m^2}$ was applied to the specimen corresponding to a temperature of 390 K. The strain in the specimen was measured with DIC and the results are shown in Figure 3.20. Nearly all of the features observed in the fixed displacement tests are seen in this case as well. There is a rapid increase in strain due to thermal expansion in the first 2 ms to a strain level of 0.0019; this is followed by an oscillation caused by the response of the system at its natural frequency. Finally, the specimen cools down, with the corresponding thermal contraction; at this point, the specimen recovers completely to its initial strain level, indicating a fully thermoelastic loading cycle during such a low temperature excursion. A similar experiment was performed on the Al 6061-T6; the time variation of the strain is shown in Figure 3.21. The strain increases to about 0.00295 in the first 2 ms, corresponding to thermal expansion and exhibits a similar thermoelastic response as the copper specimen, with complete recovery.

In order to trigger plastic deformation, a second pulse discharge was sent through the same specimen, maintained at the same load level; the temperature in this discharge increased to 490 K. The corresponding time variation of the strain for the Cu-102 and Al 6061-T6 specimens are shown in Figures 3.22 and 3.23, respectively. The thermal expansion occurs within the first 2 ms to a strain level of ~0.003 for the Cu-102 and about ~0.005 for the Al 6061-T6; these higher temperature tests show a systematic increase in the magnitude of strain with time. Upon cooling, the specimen does not recover completely, but accumulates a permanent strain of 0.0021 for the Cu-102 and 0.0085 for the Al 6061-T6.

This accumulation of plastic strain occurs during the time period from 2 ms to about 20 ms. In order to explore the plastic strain accumulation further, subsequent pulses were discharged through the same Cu-102 specimen at charge voltages of 3.0, 3.5, 4.0 4.5 5.0, 5.25, 5.5 and 5.75 kV respectively and at stress levels of 138, 172, 206 and 242 MPa; the corresponding time variation of the strain is shown in Figures 3.24 and 3.25 for a stress level of 172 MPa. The remaining plots are shown in the Appendix. Note that the total strain increment over the dead-load strain is plotted in the figure; therefore, the accumulation of plastic strain with each pulse cycle can be seen clearly. The peak temperatures reached in each test are 330 K, 390 K, 430 K, 490 K, 530 K, 580 K, 640 K and 670 K, respectively. The response is clearly quite similar to that of the second pulse, with the only difference being the amount of plastic strain accumulation; plastic strain accumulates in the time interval of 10 to ~50 ms, with the duration and magnitude depending on the peak temperature. The dynamic oscillations that were observed at lower temperature tests are not easily identified in the higher temperature tests because the plastic strain levels are significantly larger than the dynamic oscillation amplitudes and further because of damping in the material at higher temperatures. Finally, the specimen fails completely at some location outside the gage section at a strain level of about 0.08.

A similar set of experiments was performed on Al 6061-T6 specimens. The peak temperatures were kept at 350 K, 400 K, 490 K, 540 K, and 640 K; the dead-weight loading resulted in stress levels of 138, 172, 206 and 242 MPa. The time variation of the strain in for each of the temperatures corresponding to the stress level of 172 MPa is shown in Figures 3.26 and 3.27; the remaining cases are shown in Appendix III. As with the copper specimens, thermal expansion is observed in the first 2 ms heating duration. Following this, there is accumulation of plastic strain as soon as the temperature increases above 0.35 T_M. Finally, failure occurs when the strain within the gage section reaches about 0.07.

This collection of experiments on Cu 102 and Al 6061-T6 has been performed over a range of temperatures and stress levels. This set of results can be categorized in the following way: each test is identified by plotting the stress, normalized by the yield stress at room temperature, against the temperature, normalized by the melting temperature as indicated in Figure 3.28. Each test is indicated by a point on this plane, with the filled black symbols indicating conditions under which thermoelastic deformation occurs with complete recovery, and the open red symbols indicating conditions under which plastic deformation occurs in the specimen. The filled red symbols indicate conditions at which the specimen failed completely. The boundary separating elastic response and plastic strain accumulation can be identified easily; it is clear that with increasing temperature, the stress required to trigger plastic deformation decreases. This boundary is an indication of the temperature variation of the yield stress; this idea is confirmed in Figure 3.28, where the measured isothermal yield stress variation with temperature reported earlier in Figure 2.2 is shown by the blue line. This is a simple reinforcement of the idea that plastic accumulation in the short duration heating pulse requires that at the peak temperature, the corresponding isothermal yield stress must be exceeded.

The dead-load experiments provide a clear indication of development of large plastic strains during the time of 10 to 50 ms. From the thermoelastic experiments, it is clear that the temperature is nearly constant in this duration. Therefore, the strain accumulation at constant load and temperature is clearly evidence of viscoplastic response of the material. There are now two sets of experiments, one at fixed-grip conditions and the other at dead-load conditions, indicating plastic strain accumulation at different time scales; these will be examined through a common viscoplastic constitutive model in the next chapter.

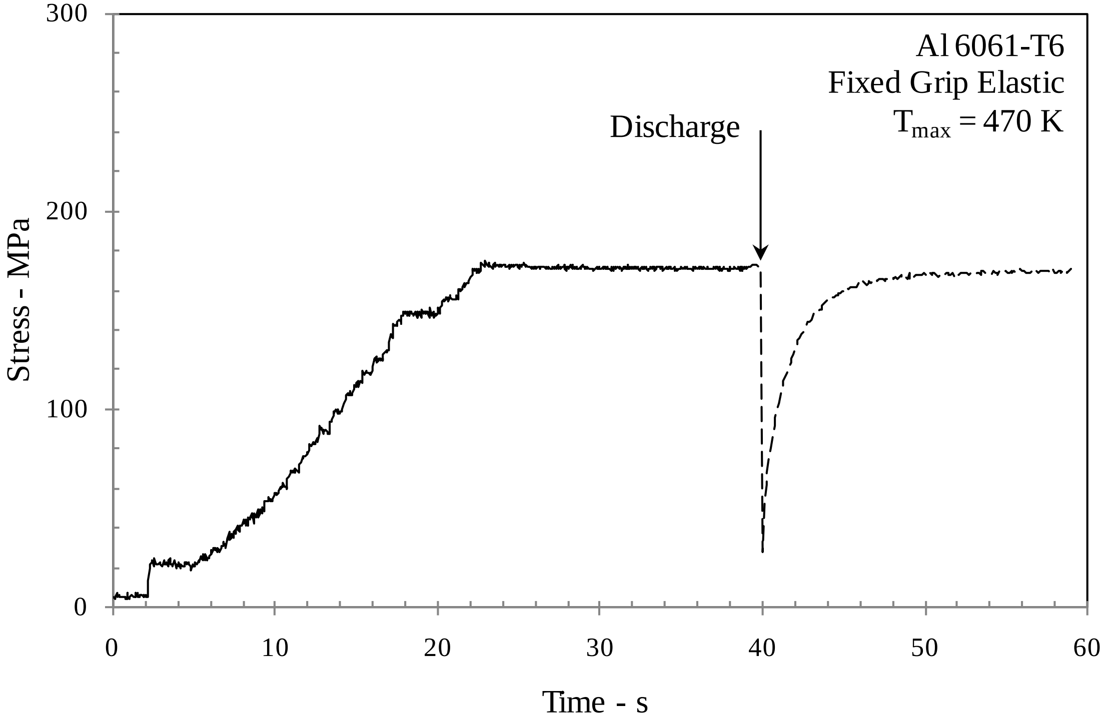

Figure 3.1. Time variation of stress in the specimen; initial stress $\sigma_i = 200$ MPa $< \sigma_Y$.

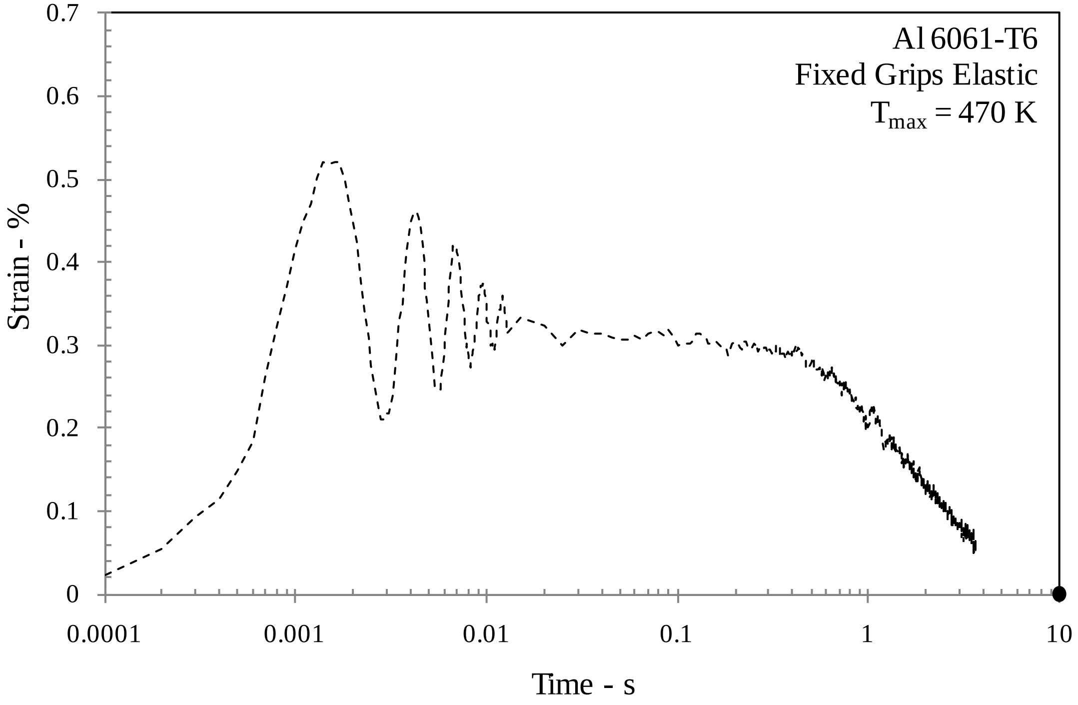

Figure 3.2. Strain variation as a function of time as calculated from DIC; initial stress $\sigma_i = 200$ MPa $< \sigma_Y$.

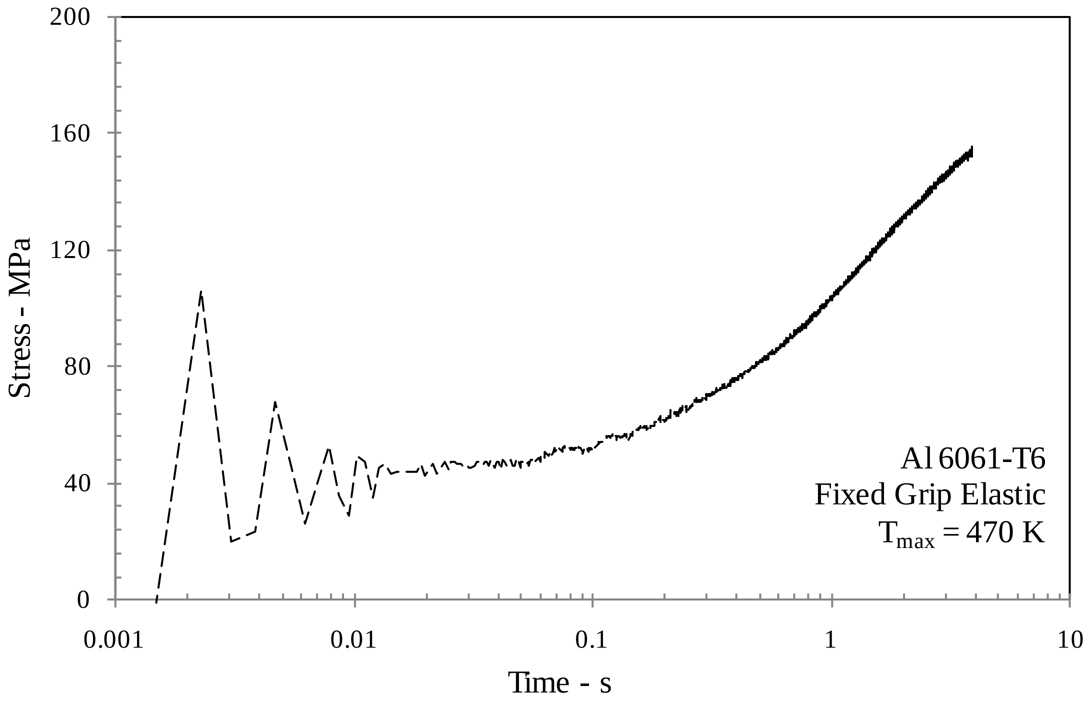

Figure 3.3. Load bolt readings from 2 ms to 4 seconds. The stress drops from 200 MPa to about 40 MPa and remains almost constant for 50 ms. The recovery is logarithmic as shown by the nearly linear behavior in the logarithmic scale.

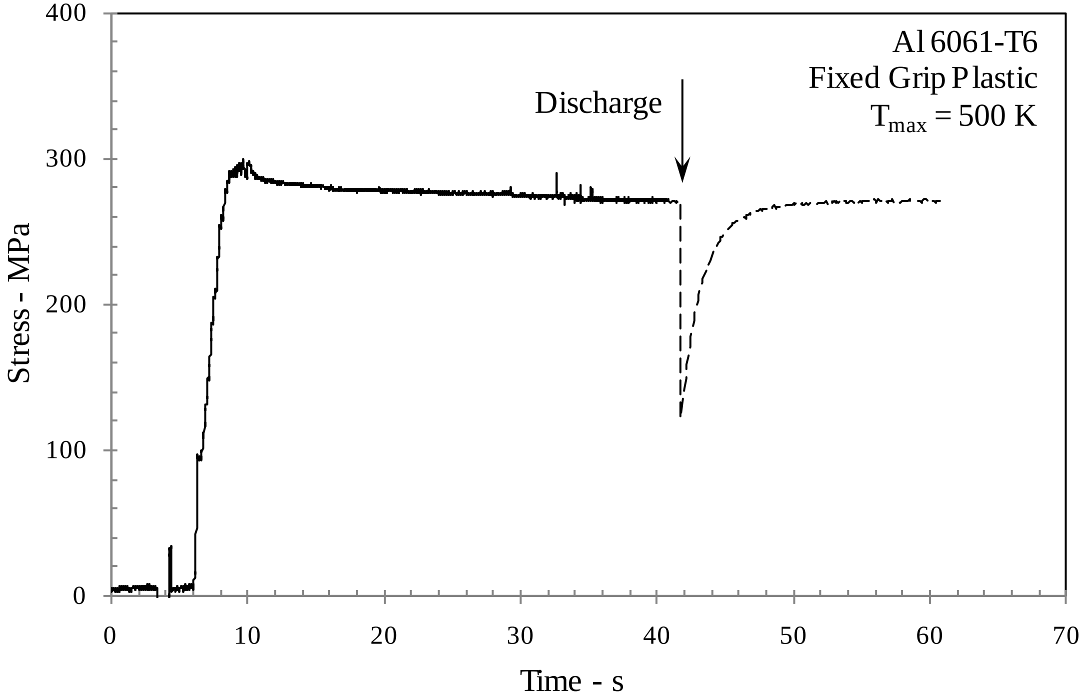

Figure 3.4. Time variation of stress in the specimen; initial stress $\sigma_i = 300$ MPa $> \sigma_Y$.

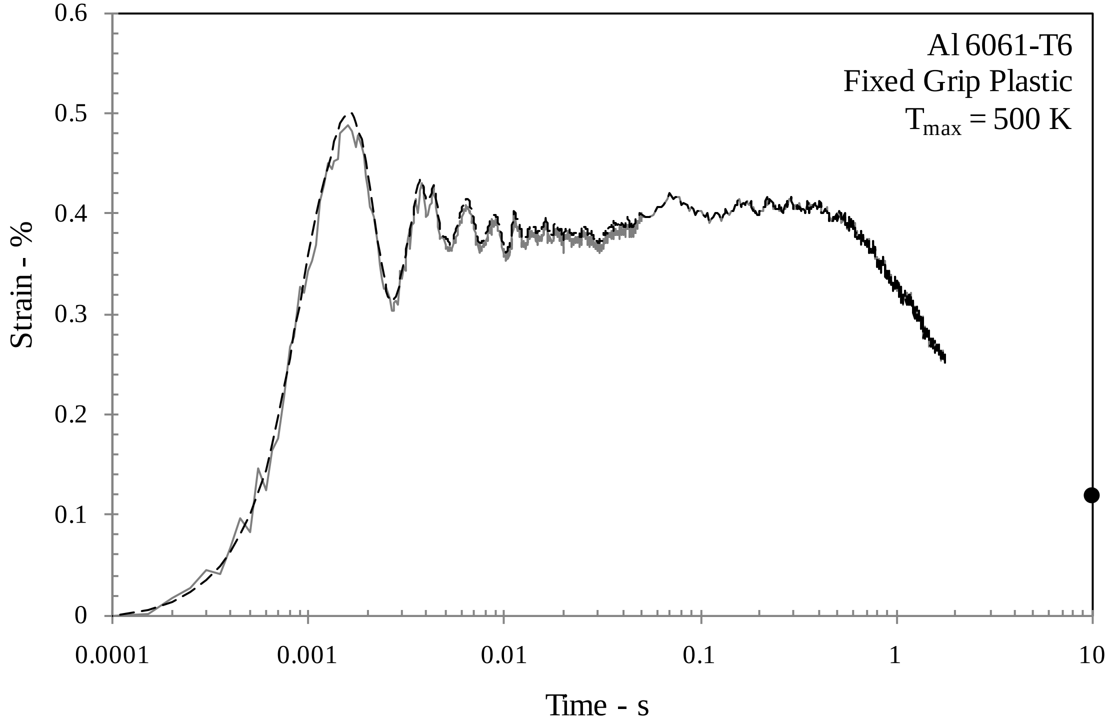

Figure 3.5. Strain variation as a function of time as calculated from DIC. The measured strain signal shown in gray line appears noisy; this noise has been filtered as shown in the dashed black line; initial stress $\sigma_i = 300$ MPa $> \sigma_Y$. .

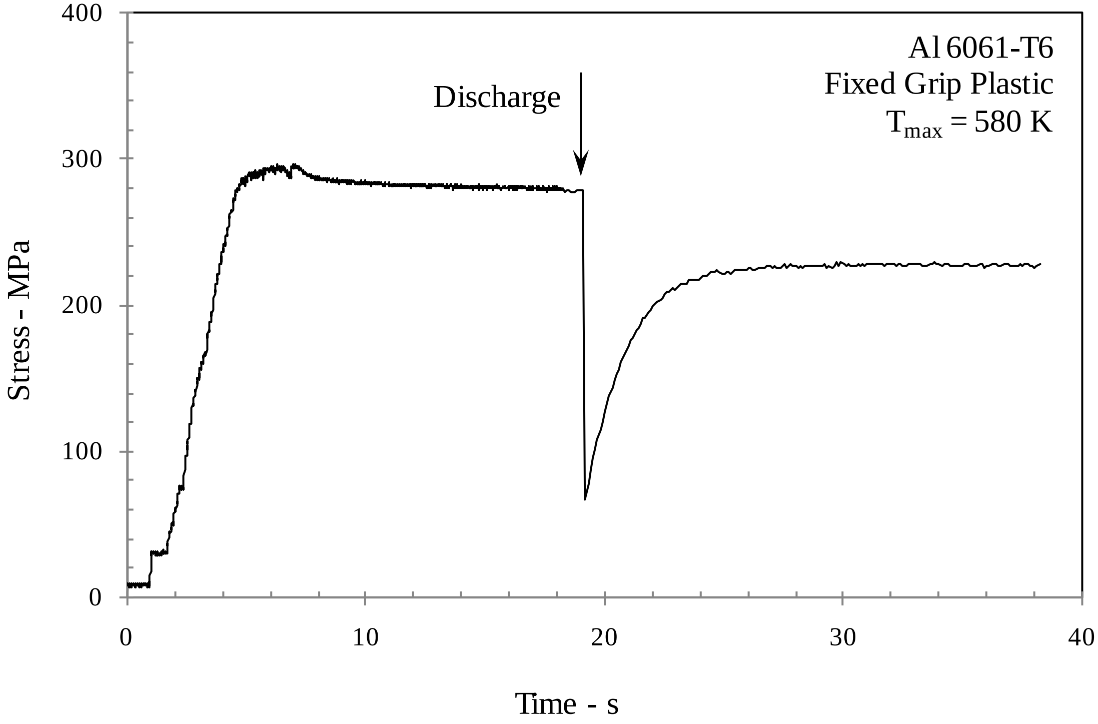

Figure 3.6. Time variation of stress in the specimen; initial stress $\sigma_i = 300$ MPa $> \sigma_Y$.

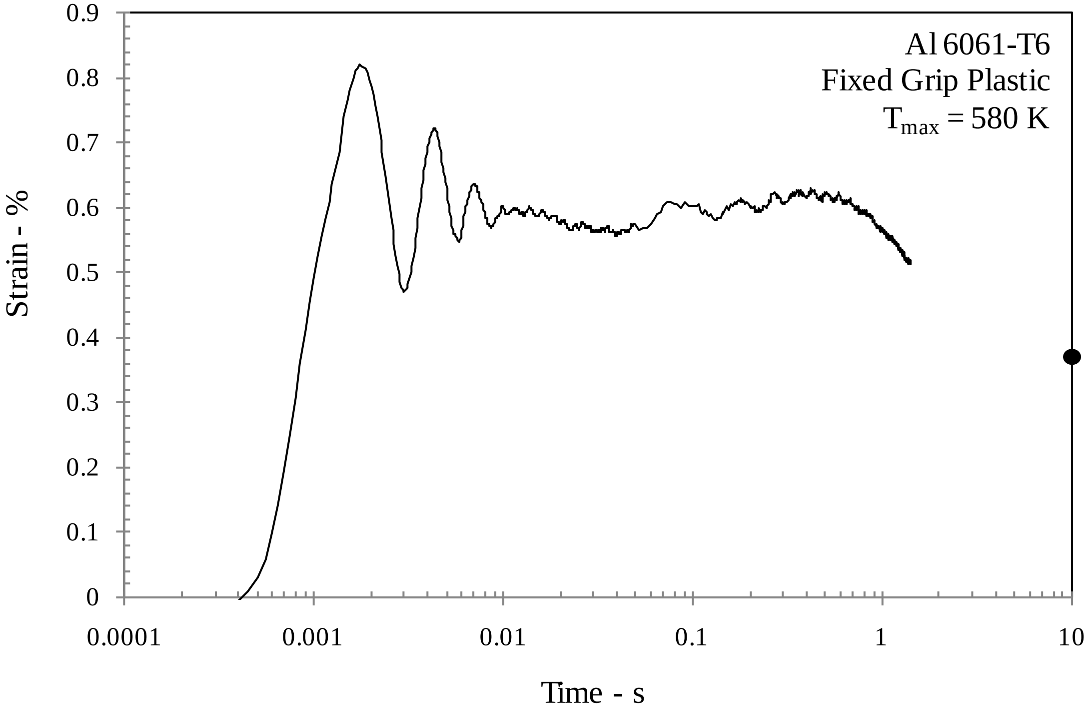

Figure 3.7. Strain variation as a function of time as calculated from DIC; initial stress $\sigma_i = 300 \text{ MPa} > \sigma_Y$.

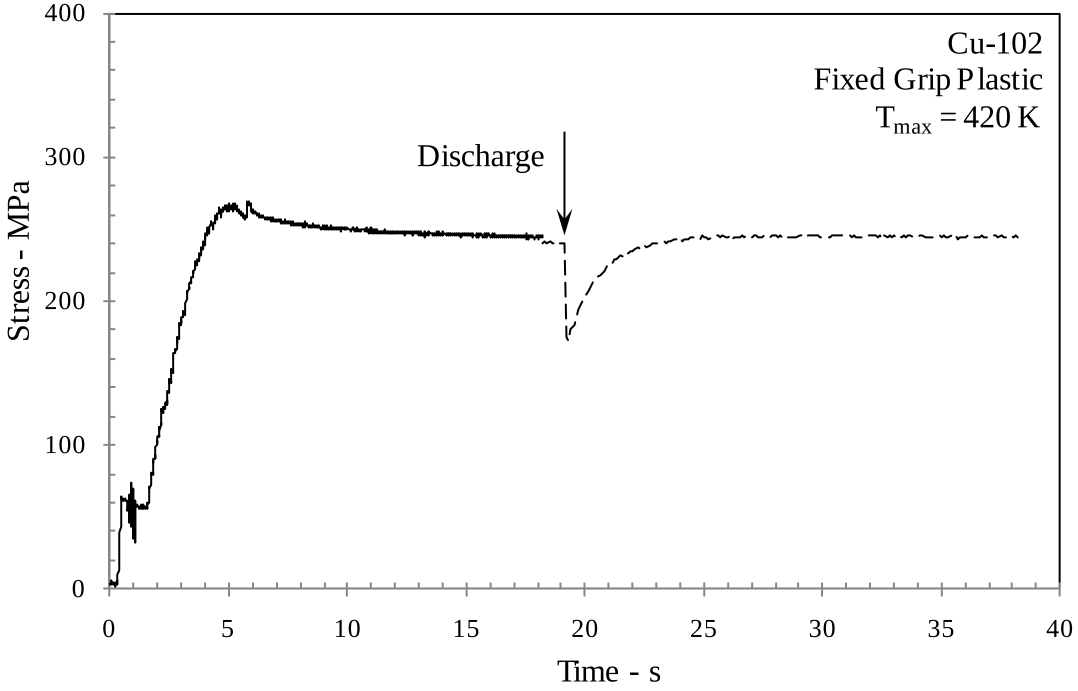

Figure 3.8. Time variation of stress in the specimen; initial stress $\sigma_i = 270$ MPa $> \sigma_Y$.

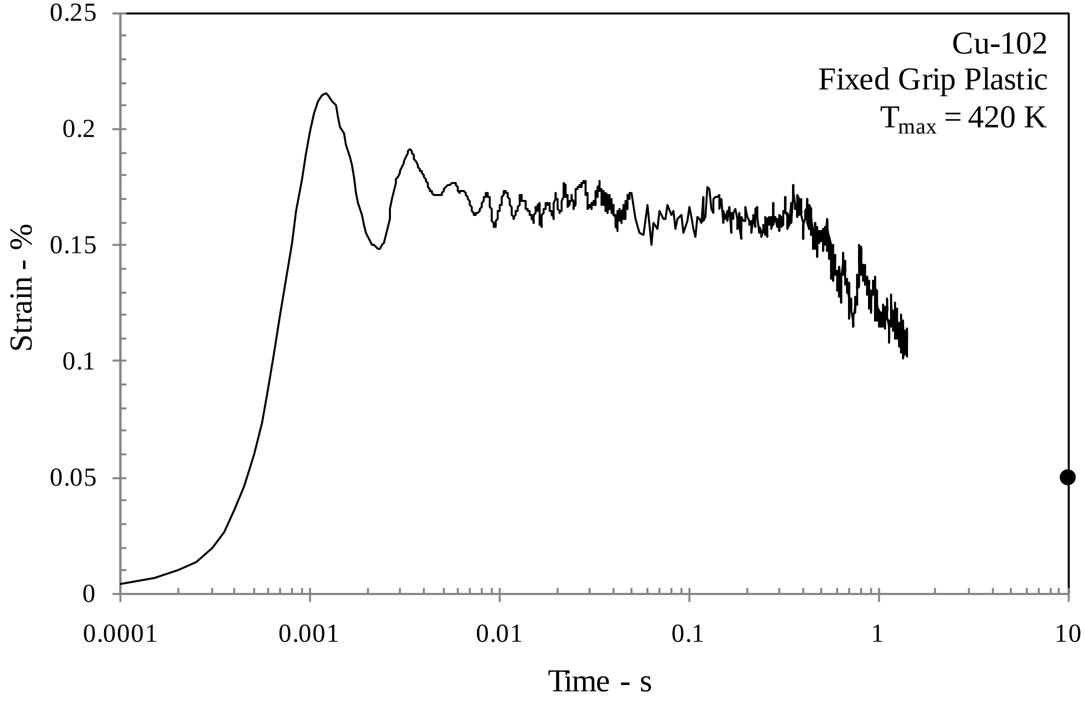

Figure 3.9. Strain variation as a function of time as calculated from DIC; initial stress $\sigma_i = 270$ MPa $> \sigma_Y$.

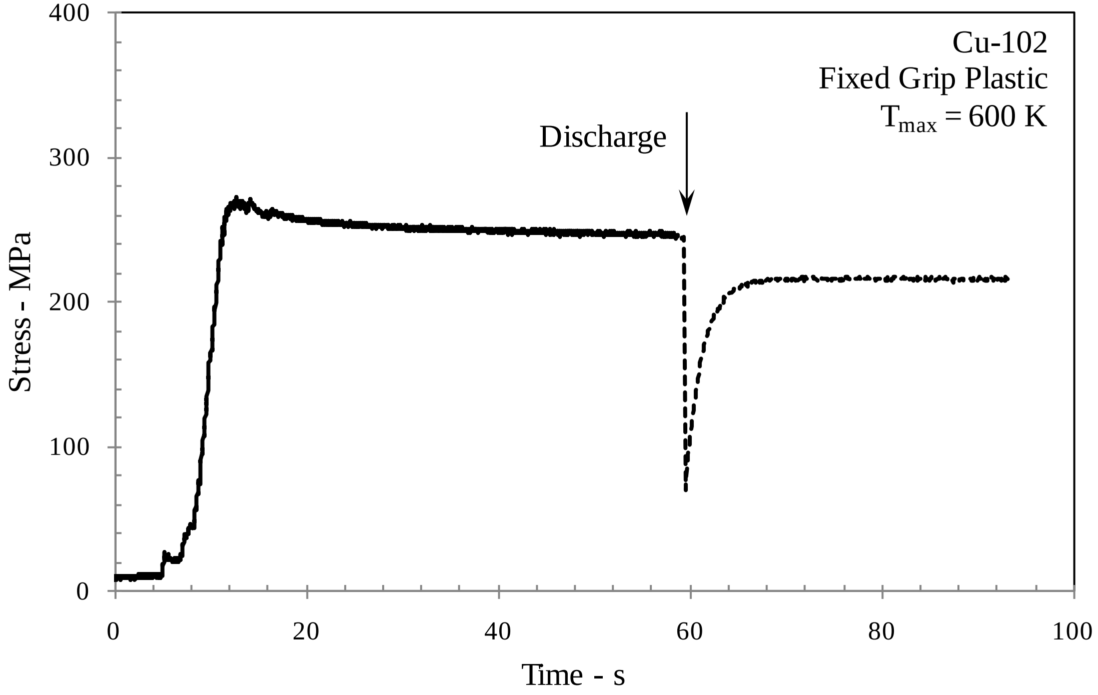

Figure 3.10. Time variation of stress in the specimen; initial stress $\sigma_i = 270$ MPa $> \sigma_Y$.

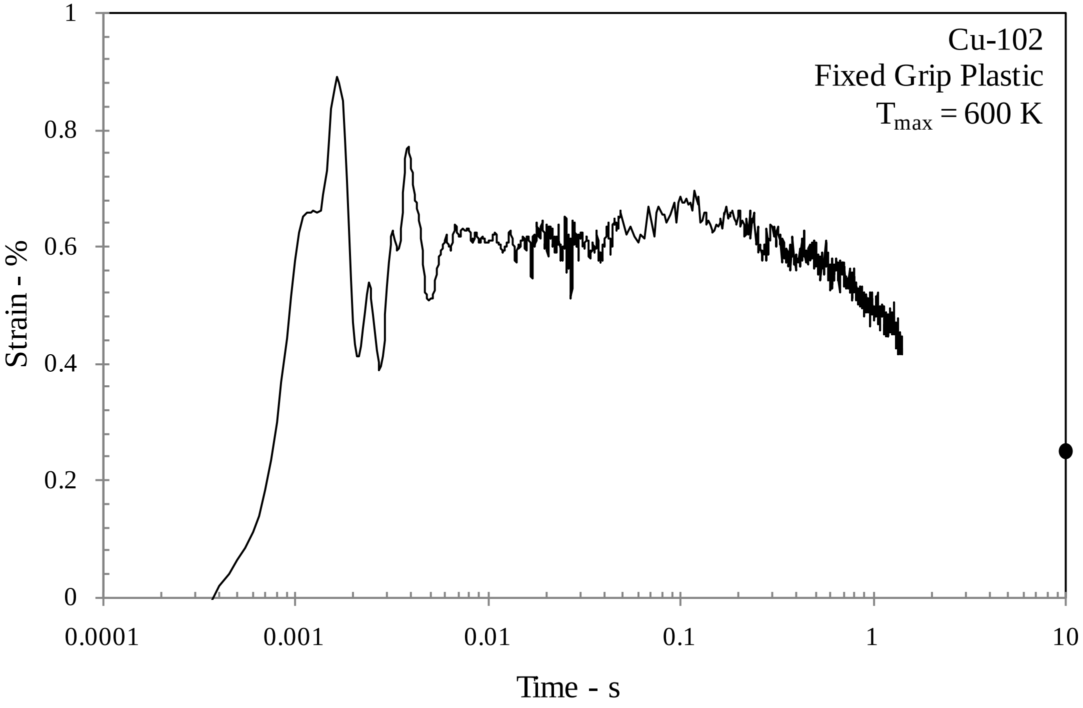

Figure 3.11. Strain variation as a function of time as calculated from DIC; initial stress $\sigma_i = 270$ MPa $> \sigma_Y$.

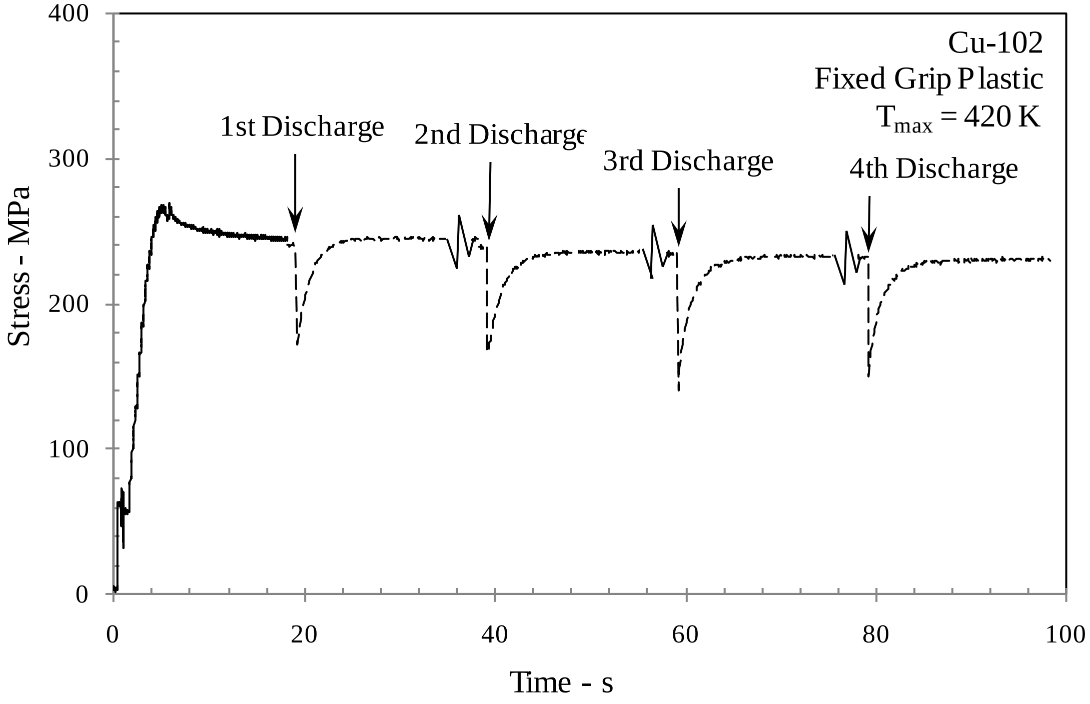

Figure 3.12. Time variation of stress in the specimen; initial stress $\sigma_i = 270$ MPa $> \sigma_Y$.

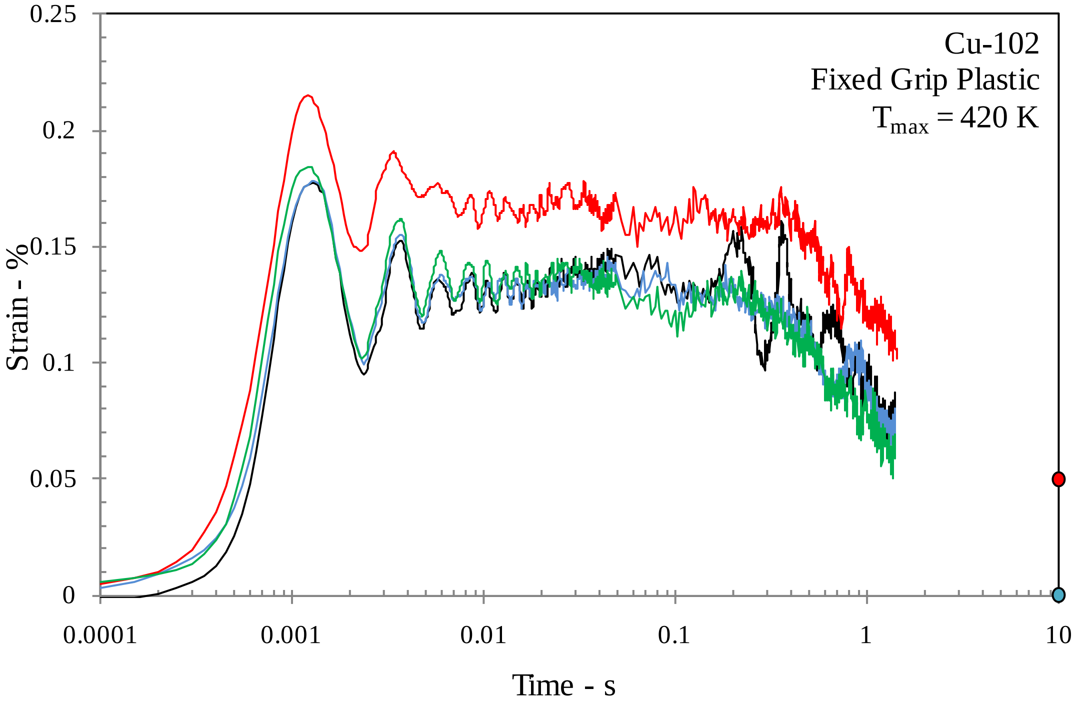

Figure 3.13. Strain variation as a function of time as calculated from DIC; initial stress $\sigma_i = 270$ MPa $> \sigma_Y$.

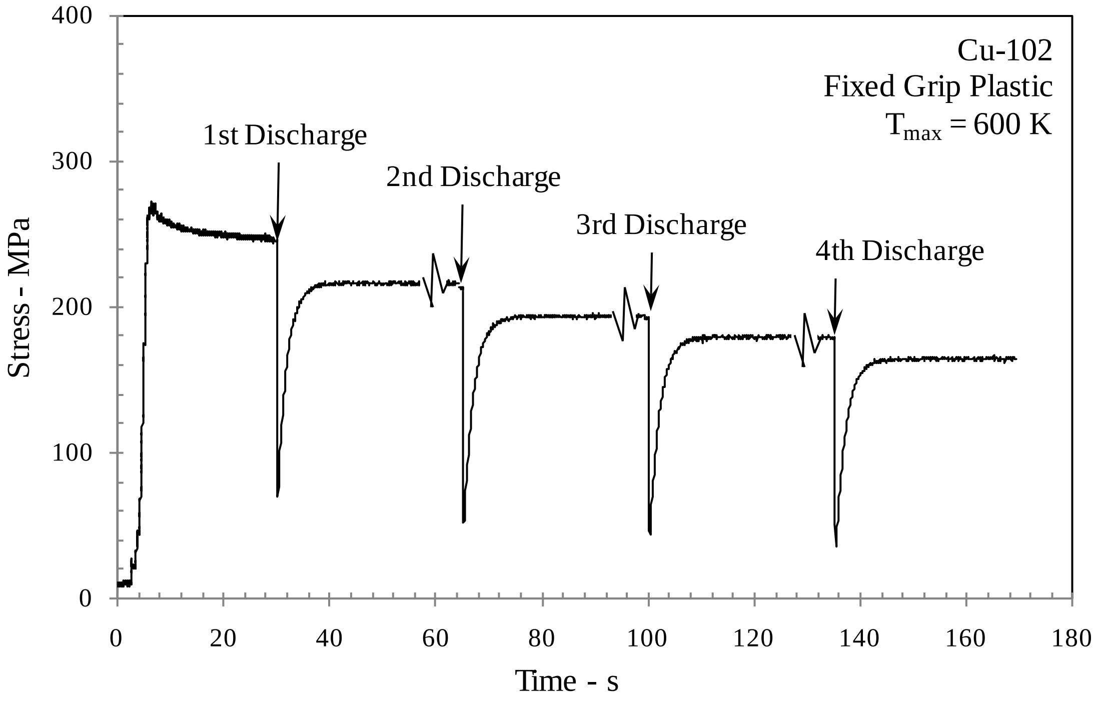

Figure 3.14. Time variation of stress in the specimen; initial stress $\sigma_i = 270$ MPa $> \sigma_Y$.

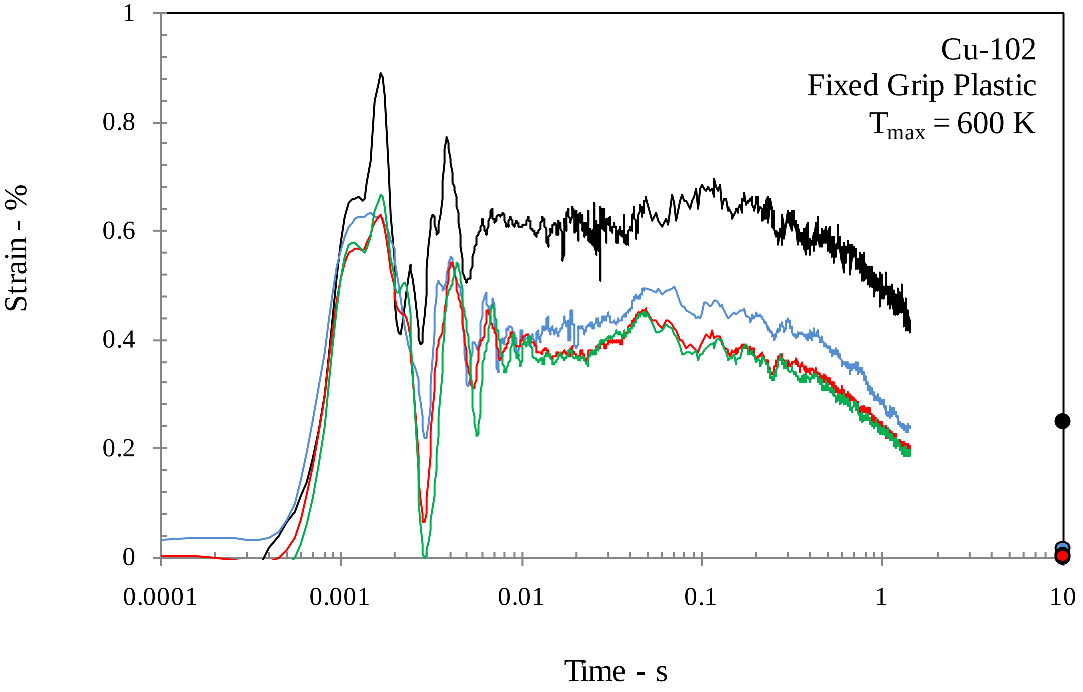

Figure 3.15. Strain variation as a function of time as calculated from DIC; initial stress $\sigma_i = 270$ MPa $> \sigma_Y$.

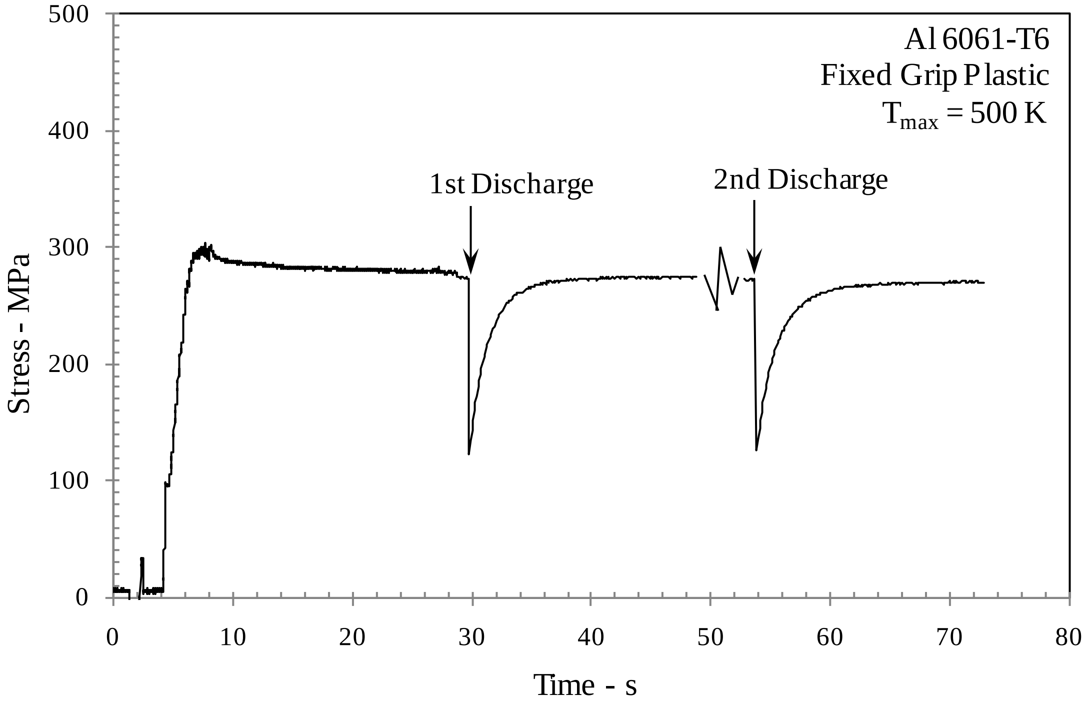

Figure 3.16. Time variation of stress in the specimen; initial stress $\sigma_i = 300$ MPa $> \sigma_Y$.

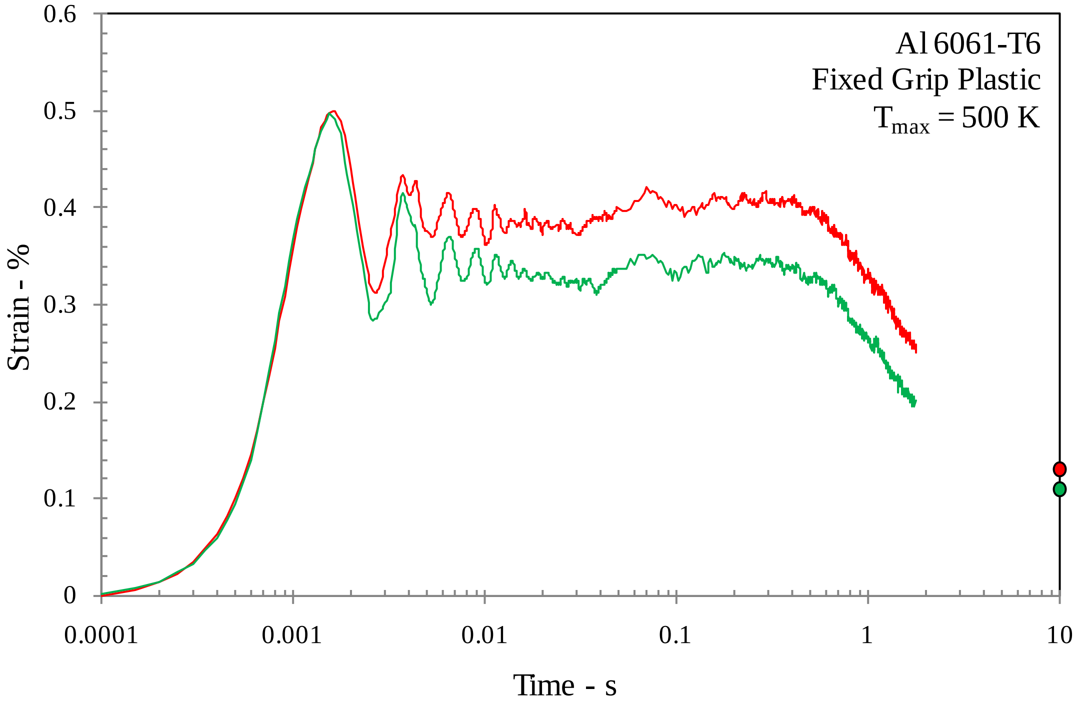

Figure 3.17. Strain variation as a function of time as calculated from DIC; initial stress $\sigma_i = 300$ MPa $> \sigma_Y$.

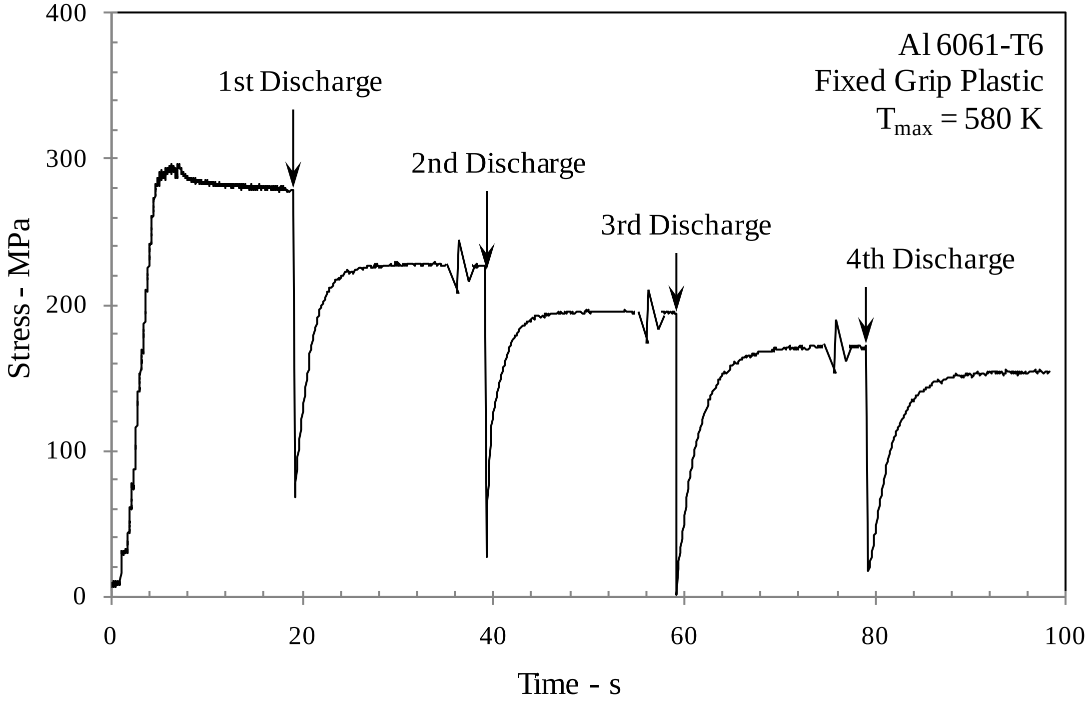

Figure 3.18. Time variation of stress in the specimen; initial stress $\sigma_i = 300$ MPa $> \sigma_Y$.

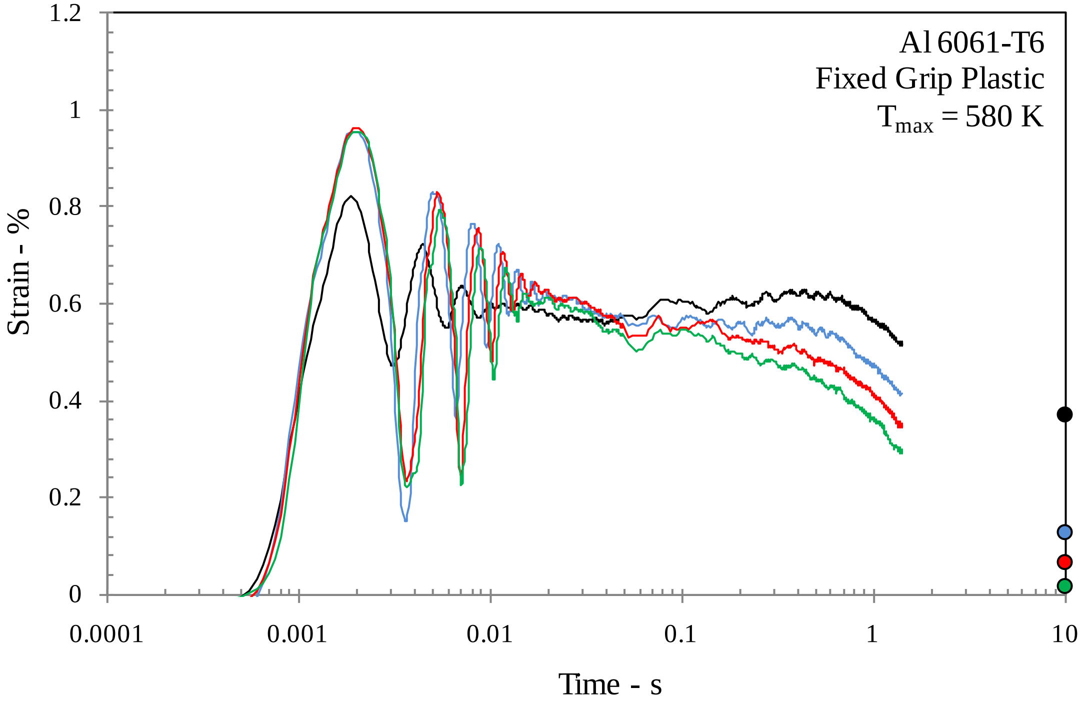

Figure 3.19. Strain variation as a function of time as calculated from DIC; initial stress $\sigma_i = 300$ MPa $> \sigma_Y$.

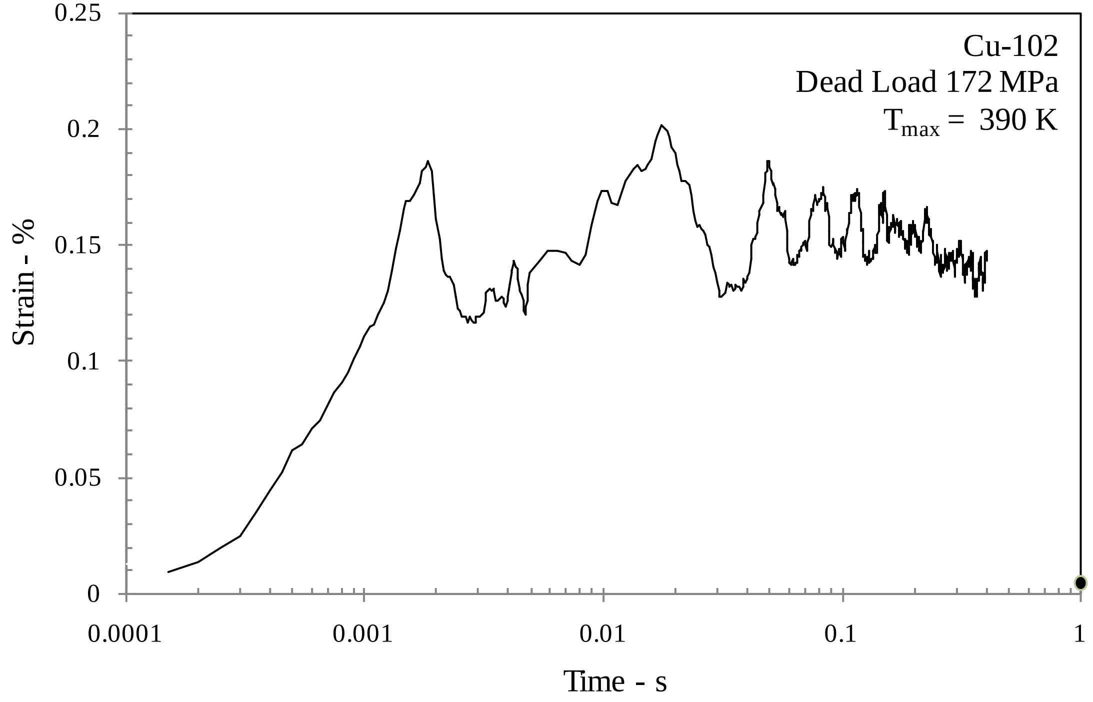

Figure 3.20. Strain variation as a function of time as calculated from DIC; initial stress $\sigma_i = 172$ MPa $< \sigma_Y$.

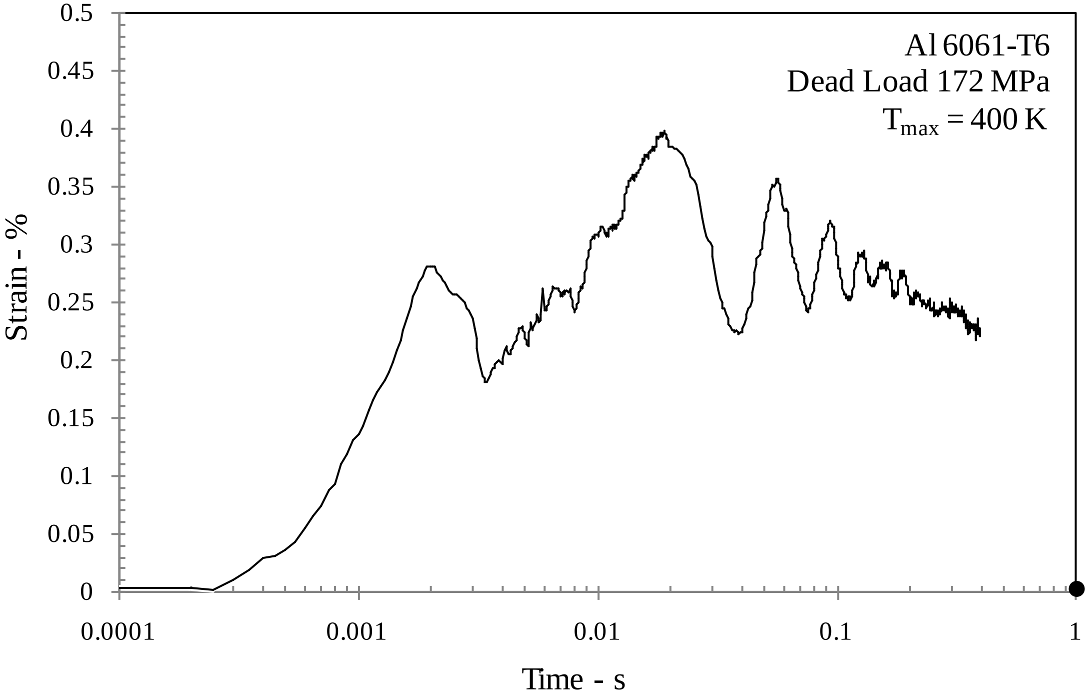

Figure 3.21. Strain variation as a function of time as calculated from DIC; initial stress $\sigma_i = 172$ MPa $< \sigma_Y$.

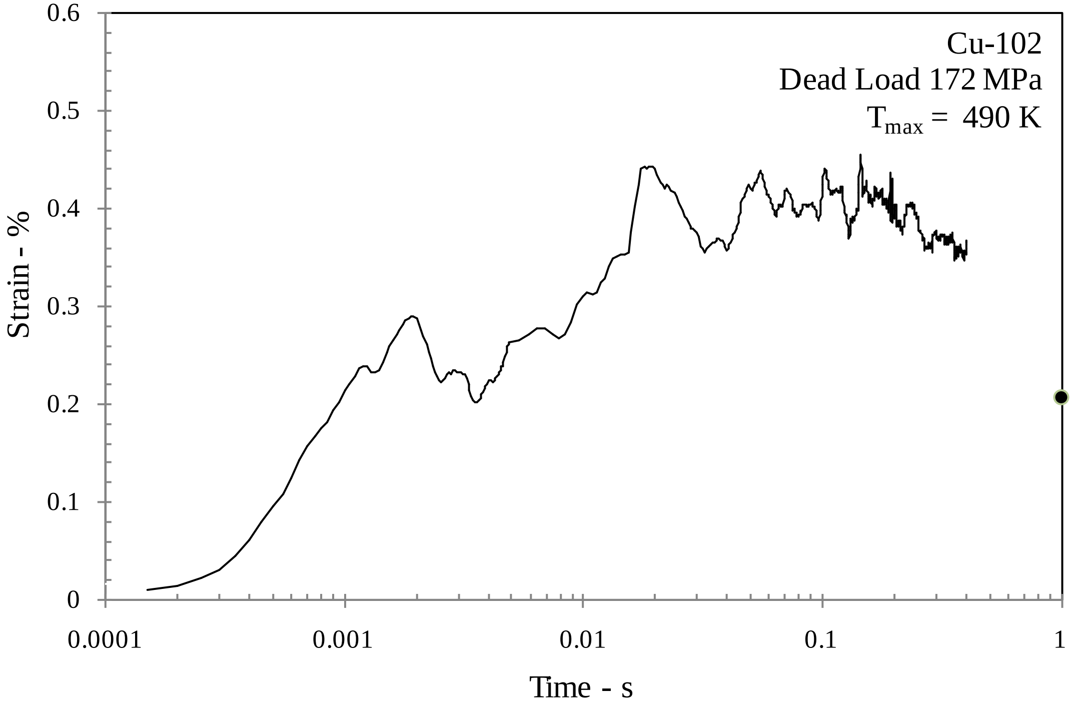

Figure 3.22. Strain variation as a function of time as calculated from DIC; initial stress $\sigma_i = 172$ MPa $< \sigma_Y$.

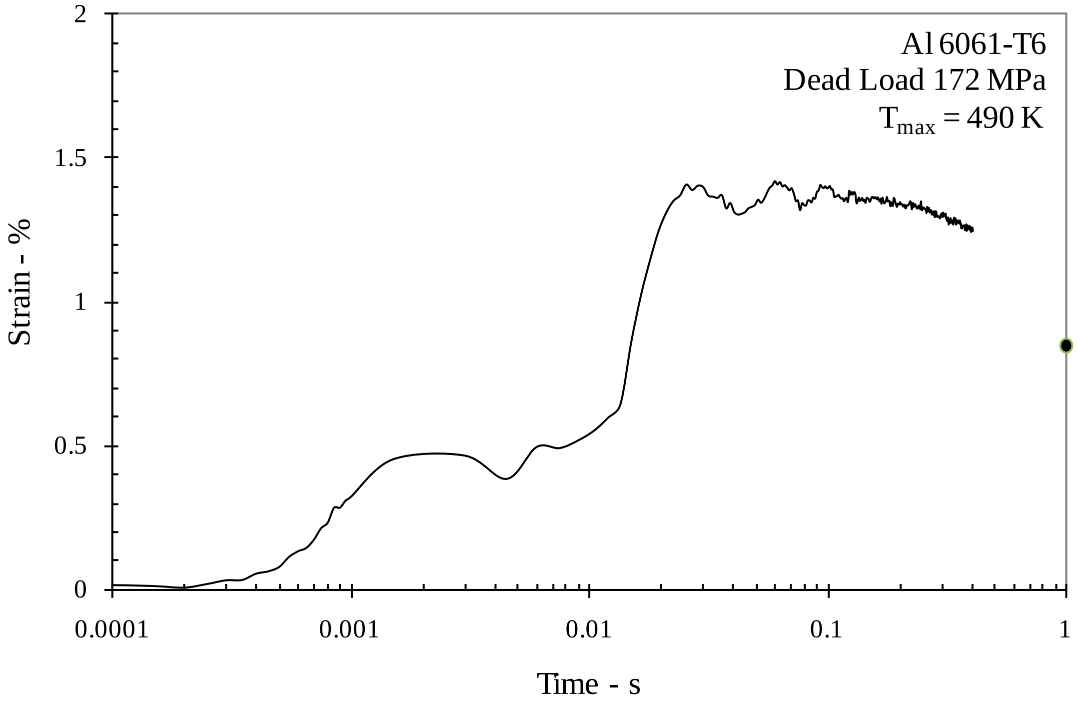

Figure 3.23. Strain variation as a function of time as calculated from DIC; initial stress $\sigma_i = 172$ MPa $< \sigma_Y$.

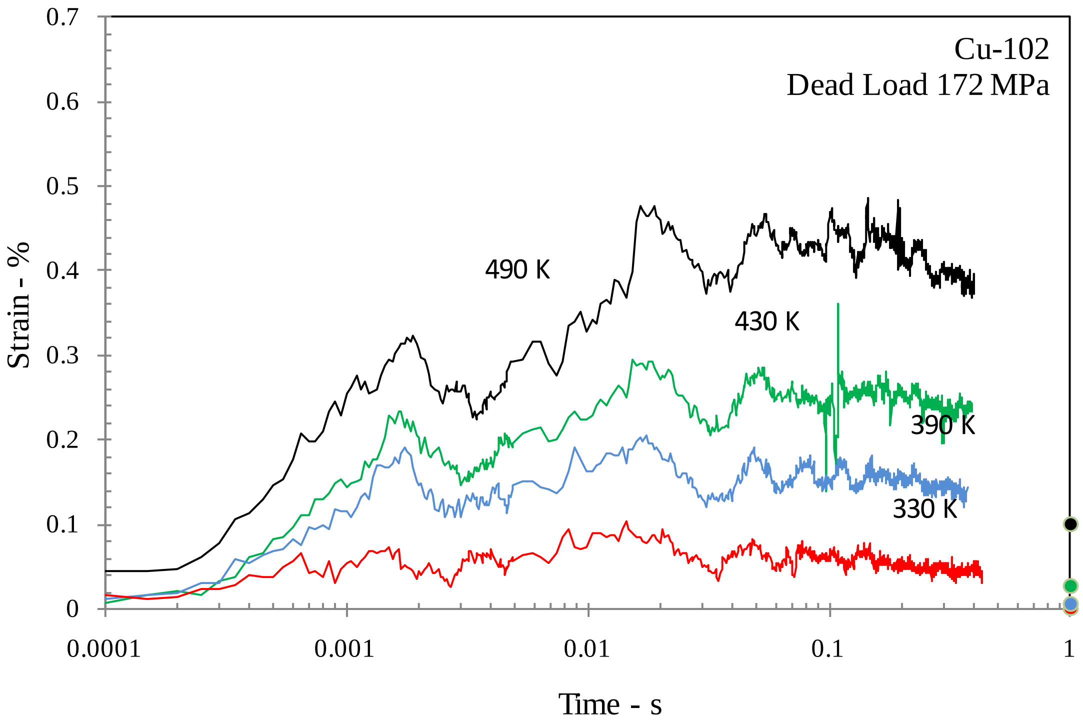

Figure 3.24. Strain variation as a function of time as calculated from DIC; initial stress $\sigma_i = 172$ MPa $< \sigma_Y$.

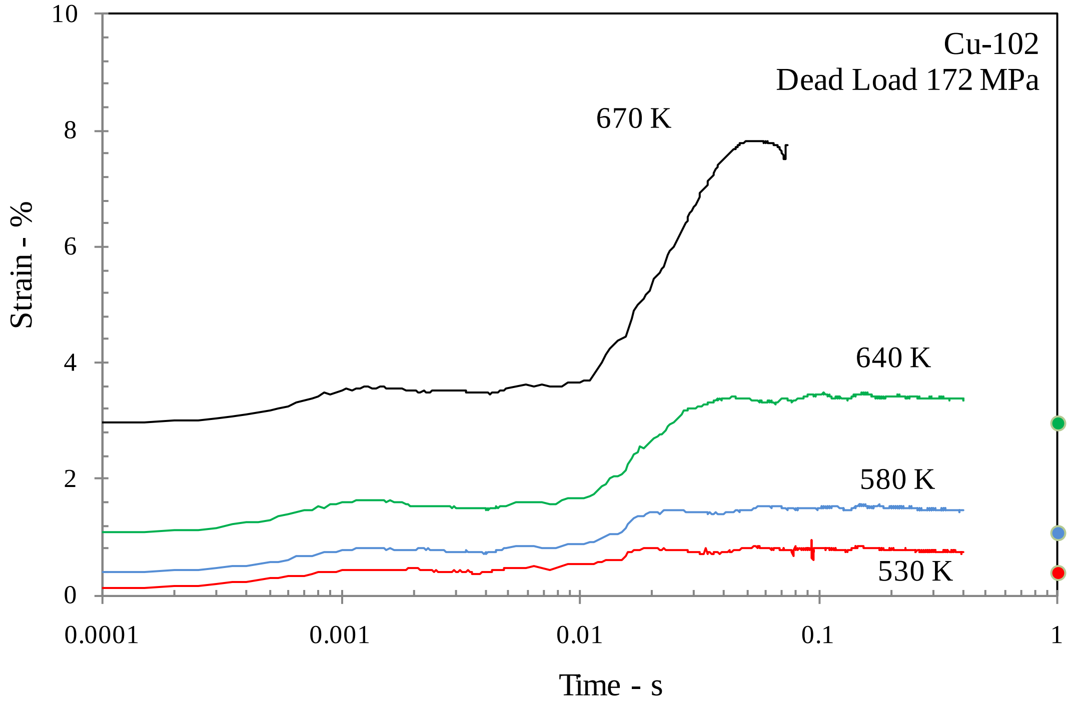

Figure 3.25. Strain variation as a function of time as calculated from DIC; initial stress $\sigma_i = 172$ MPa $< \sigma_Y$.

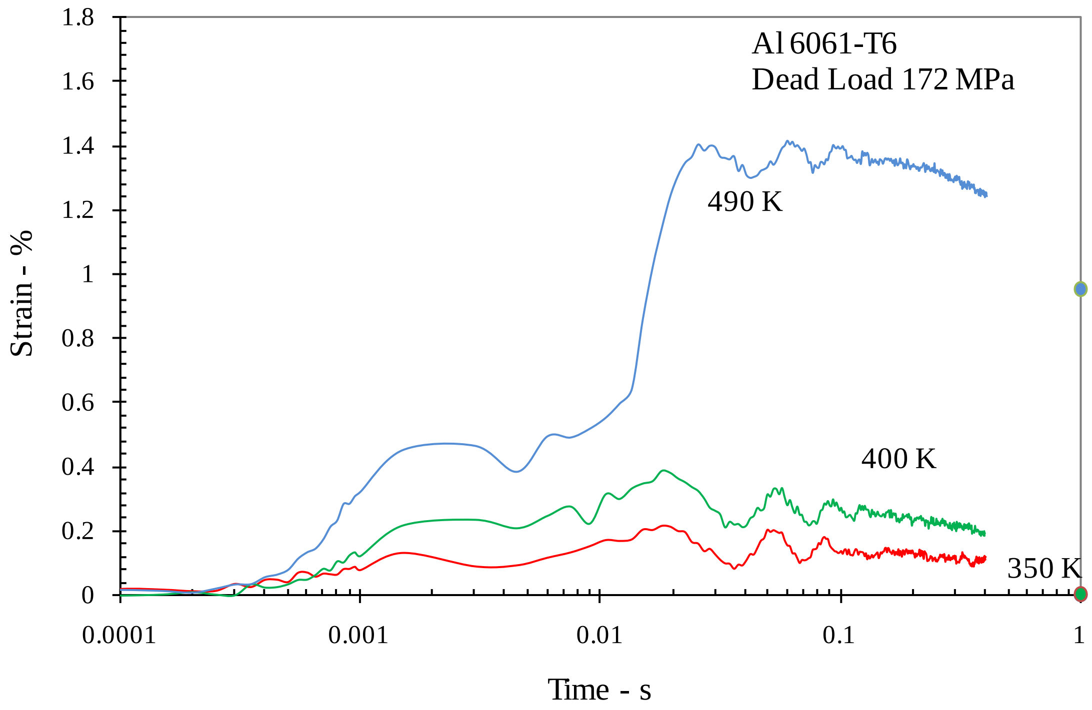

Figure 3.26. Strain variation as a function of time as calculated from DIC; initial stress $\sigma_i = 172$ MPa $< \sigma_Y$.

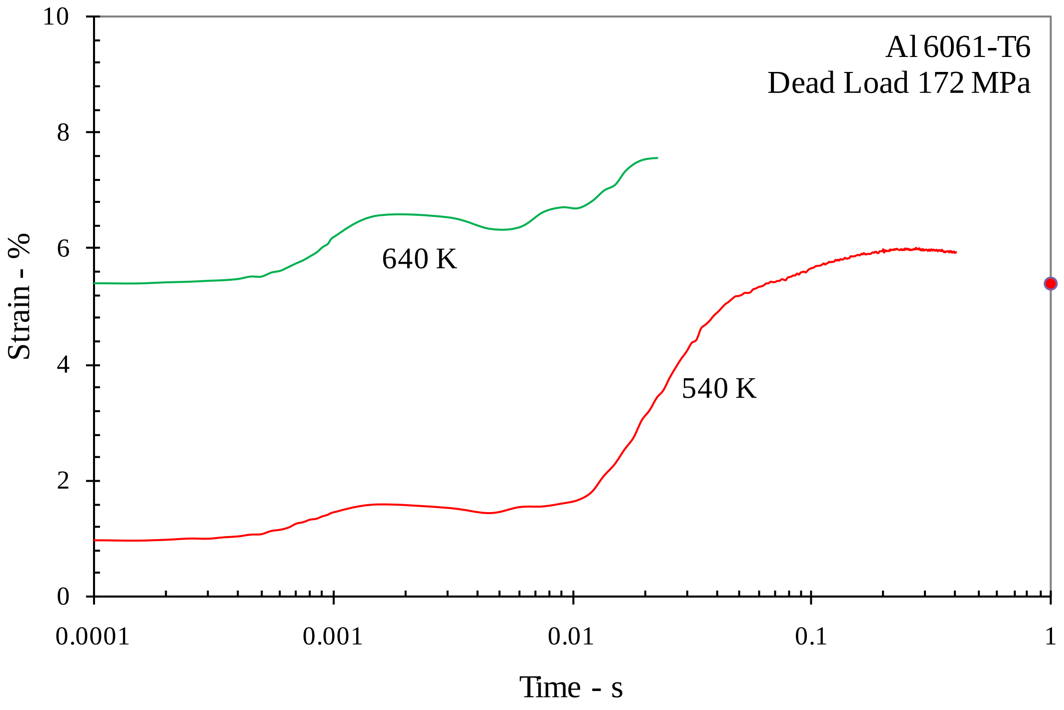

Figure 3.27. Strain variation as a function of time as calculated from DIC; initial stress $\sigma_i = 172$ MPa $< \sigma_Y$.

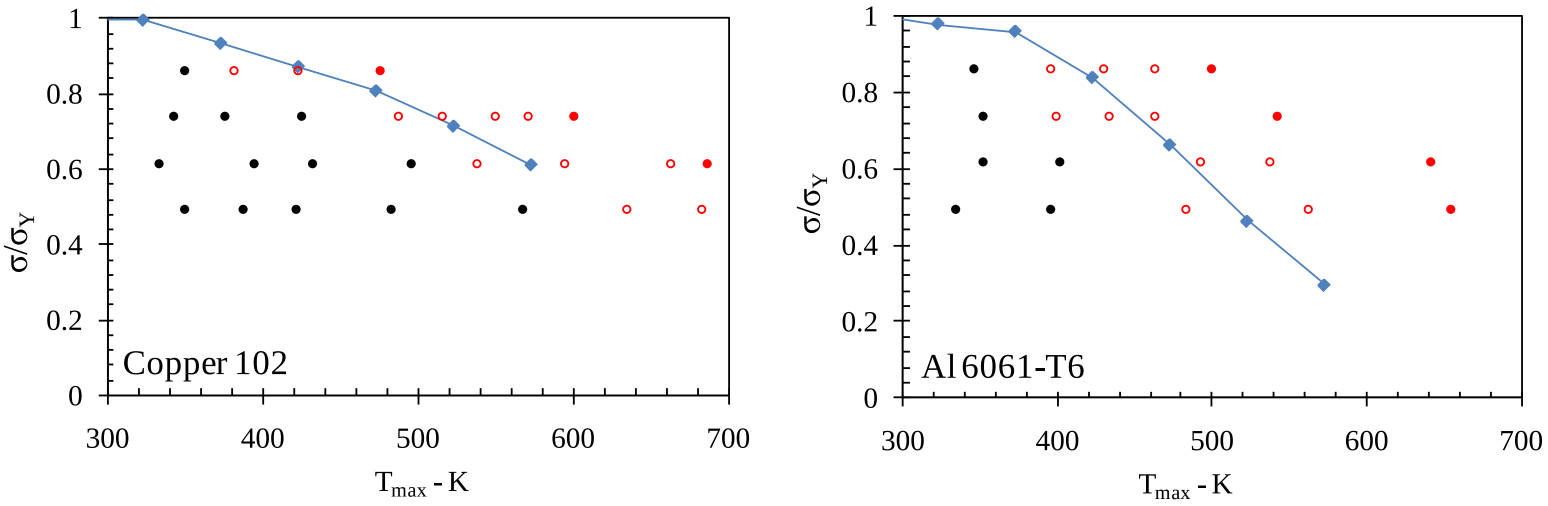

Figure 3.28. Plastic strain accumulation scheme. (a) Al 6061 T6 and (b) Cu 102. Black dots represent regions of elastic behavior; hollow dots are points of plastic strain accumulation and the full red dot are limit for specimen failure.

4. VISCOPLASTIC MODEL OF THE EXPERIMENT

The experiments described above provide significant insight into the effect of short duration pulsed current on plastic deformation. These measurements are interpreted in this chapter using a viscoplastic constitutive model of the material behavior. The observed response for both loading conditions – fixed grip and dead load – can be decomposed into 3 stages, but the fixed-grip case is considered first.

4.1. Physical Interpretation of the Stages of Deformation

The specimen, initially at the temperature T_0, is loaded to a stress level σ_i; if this value is greater than the yield stress $\sigma_Y(T_0)$ some plastic strain is accumulated; subsequently due to grip relaxation the specimen undergoes a small elastic unloading, and ends in a steady state at the end of stage 1; this will be called state 1. During stage 2, with the grips fixed at this level, the specimen is then subjected to a current pulse that raises the temperature by ΔT within 2 ms; the resulting thermal expansion of the specimen decreases the load experienced by the specimen under the fixed grip conditions, even though some compliance and dynamic effects may be present. In response to this, the stress drops to $\sigma_{\min}$; this is state 2. Note that due to electromagnetic interference, the actual load history of the load during this phase is not known. If the load drop is due only to thermal expansion of the specimen, then this unloading is an elastic process and as the specimen cools down during stage 3 to ambient temperature through conduction and radiation, in a matter of about 10 s, the stress level in the specimen must increase back to state 1 (σ_i). Those stages are summarized graphically in Figure 4.1. As noted in Section 3.1.1, for specimens subjected to elastic loading and a small amplitude current pulse, this is precisely what was observed. However, the experimental observations on initially plastically loaded specimens, indicate that the stress level increases only to $\sigma_f < \sigma_i$ (this is called state 3), and that the specimen accumulated some plastic strain.

For dead load boundary conditions the same three stages arise, but with a few exceptions. First, the specimen had to be loaded elastically; if the yield stress is exceeded the specimen fails due to instability caused by the low hardening exponent. Second, when the current is discharged, the material still experiences thermal expansion but this time the load does not drop because the weight was attached to the bottom grip; instead the load oscillates due to the dynamics associated with the system. These oscillations maintain the original dead load value on average. Finally, during the cooling phase, the load remains constant while the thermal strain is recovered.

Despite the differences in the conditions of the fixed grip and fixed load experiments, the same analysis can be used to interpret both types of experiments. At state 1, the measured displacement Δ_T^1 between two fixed gage points at a distance L apart on the specimen can be decomposed into two parts: the elastic displacement, $\varepsilon_e L$ and plastic displacement, $\varepsilon_p L$, the latter, if present. Therefore,

$$\frac{\Delta_T^1}{L} = \varepsilon_e + \varepsilon_p = \frac{\sigma_i}{E} + \frac{\left(\sigma_i - \sigma_Y(T_0)\right)}{E_*} \tag{4.1}$$

where $E_* = EE_T / (E - E_T)$, where E_T is the tangent modulus corresponding to a bilinear approximation; in both tests the total gage displacement experienced by the specimen varies during the current pulses due to the compliance of the fixtures and dynamic effects but since the displacement is monitored at fixed gage points on the specimen, the compliance effects do not influence the analysis. In state 2, (when the thermal strain is at its maximum level), Eq. (4.1) must be modified to account for thermal expansion:

$$\frac{\Delta_T^2}{L} = \varepsilon_e + \varepsilon_p + \varepsilon_{th} = \frac{\sigma_{\min}}{E} + \frac{\left(\sigma_i - \sigma_Y(T_0)\right)}{E_*} + \alpha\Delta T + \Delta\varepsilon_{p1} \tag{4.2}$$

In the above equation the possibility that additional plastic deformation, $\Delta\varepsilon_{p1}$, could be accumulated as the specimen goes from stage 1 to stage 2 is also incorporated. This is based on a conjecture that viscoplastic effects may be dominant when the strain rates are high and will be explored in the following. Finally in stage 3, the cooling of the specimen to room temperature eliminates thermal expansion and hence:

$$\frac{\Delta_T^3}{L} = \varepsilon_e + \varepsilon_p = \frac{\sigma_f}{E} + \frac{\left(\sigma_i - \sigma_Y(T_0)\right)}{E_*} + \Delta\varepsilon_{p1} + \Delta\varepsilon_{p2} \tag{4.3}$$

The possibility of further accumulation of plastic strain during the cooling period is introduced in Eq. (4.3) through the term $\Delta\varepsilon_{p2}$; this is because the temperature remains high for one second.

In the experiments reported in Section 3.6 – 3.8 the gage strain $\frac{\Delta_T}{L}$ was measured. The thermal strain $\alpha \Delta T$ can be determined from the temperature estimated from the current measurements, and the elastic strain $\frac{\sigma_i}{E}$ can be obtained from the load measurements; this last reading was not obtained for the dead load experiments. All these measurements are resolved in time except for the elastic strain during the first 2 ms corresponding to the current discharge duration and the thermal strain for times larger than 2 ms. Comparing Eqs. (4.1) and (4.3) it is clear that the observed difference in stress between stages 3 and 1 is possible *if and only if* additional plastic strains are generated during heating or cooling of the specimen. Such additional plastic strains are possible only if the yield stress drops (from thermal effects) below the stress that the specimen experiences and triggers viscoplastic flow. Hence, for non-isothermal conditions, Eq.(4.2) is then rewritten as:

$$\frac{\Delta_T(t)}{L} = \frac{\sigma(t)}{E} + \frac{\left(\sigma_i - \sigma_Y(T_0)\right)}{E_*} + \alpha \Delta T(t) + \varepsilon_p(t) \tag{4.4}$$

This partition of the strain can be used in interpreting the experimental observations described in Chapter 3.

4.2. Viscoplastic Analysis of Response to Short Duration Current Pulses

In the experiments discussed in Chapter 3, the gauge strain is measured with DIC and the thermal expansion is obtained through an indirect reading of the temperature as discussed in Chapter 2.3. While a direct reading of the load was attempted, the disturbances created by the electromagnetic field during the pulse discharge made it impossible to obtain a usable load signal for the first 2 ms. Nevertheless, the independent measurements of the temperature and local strain eliminates the need to evaluate the compliance of the loading apparatus and can be used to obtain an accurate estimate of the plastic strain accumulation resulting from the discharge. However, a viscoplastic model is necessary in order to track the plastic strain evolution during the heating and cooling periods. If a differential viscoplastic constitutive equation relating the stress to the strain rate is introduced, Eq.(4.4) can be written in the following compact form:

$$\dot{\varepsilon}_T = \dot{\varepsilon}_E + \dot{\varepsilon}_{th} + \dot{\varepsilon}_p = \dot{\sigma}/E + \alpha\dot{\Delta}T + \dot{\varepsilon}_p\left(\sigma,\overline{\varepsilon},T\right) \tag{4.5}$$

where the superdots indicate the time derivative of the corresponding quantities and $\dot{\varepsilon}_p\left(\sigma,\overline{\varepsilon},T\right)$ is a suitable viscoplastic model that describes the plastic strain evolution in terms of the stress, accumulated plastic strain ($\overline{\varepsilon} = \int_0^t \dot{\overline{\varepsilon}}dt$) and temperature. Bilyk et al (2003) have recently incorporated such a viscoplastic model to analyze the results of Okazaki et al (1978) for the constant strain rate experiments. Here, this model will be further investigated with the present experimental results and some modifications will be proposed to describe the physical phenomena better. This model was chosen for the following reasons: first, the range of temperatures experienced by the specimens – 0.2 – 0.5 T_M – is such that viscoplasticity is expected to dominate the behavior of the material. Secondly, since the maximum strain rates observed are in the order of 10 per second, the addition of a high strain rate response was considered useful. Lastly, since the temperature rise is significant, the model must include temperature effects on plastic response. The model selected here provides sufficient flexibility to incorporate temperature and strain rate effects.

4.2.1. VISCOPLASTIC CONSTITUTIVE MODEL

The viscoplastic constitutive equation is taken to be as follows (Zhou and Clifton 1997) for the uniaxial loading:

$$\dot{\varepsilon}_p = \frac{\dot{\varepsilon}_1 \dot{\varepsilon}_2}{\dot{\varepsilon}_1 + \dot{\varepsilon}_2}, \ \dot{\varepsilon}_1 = \dot{\varepsilon}_0 \left[\frac{\bar{\sigma}}{g(\bar{\varepsilon}, T)} \right]^m, \ \dot{\varepsilon}_2 = \dot{\varepsilon}_m \exp\left[-\frac{a g(\bar{\varepsilon}, T)}{\bar{\sigma}} \right] \tag{4.6}$$

$$g(\bar{\varepsilon}, \sigma) = \sigma_0\left(\bar{\varepsilon}\right) \left[1 - \beta \left\{ \left(\frac{T}{T_0} \right)^{\kappa} - 1 \right\} \right] \tag{4.7}$$

where the function $g(\bar{\varepsilon}, T)$ is the quasi-static stress strain relation at a (small) reference strain rate $\dot{\varepsilon}_0$, β and κ are thermal softening parameters, T is the temperature and T_0 is a reference temperature. m and a are rate-sensitivity parameters corresponding to strain rates below 10^3 s^{-1} and above 5×10^4 s^{-1}. Note that Eq. (4.6) is valid only when $\bar{\sigma} > g$; otherwise $\dot{\varepsilon}_p = 0$. Substituting the constitutive law in Eq.(4.4) results in a nonlinear differential equation of the stress at fixed grip for a given temperature history. This can be solved numerically using a finite difference scheme.

Zhou and Clifton, (1997) provided a calibration of the parameters of this viscoplastic model; however, the model was calibrated using quasi-static tests for the materials considered in this work. The isothermal yield function was obtained from the stress strain curves measured at room temperature for each material by Watkins et al. (2005). The temperature dependence was calibrated by first determining the yield stress variation with temperature from isothermal stress strain curves (see Figures AII:1 and AII:2 for the isothermal σ-ε curves for the Al 6061-T6 and Cu 102 examined in this work) and then determining the two parameters β and κ by fitting Eq.(4.7) to the data for both materials; the temperature variation of the yield stress as well as the best fit model are shown in Figure 4.2. The green line represents the parameters suggested by Bilyk et al. (2005). The difference between the curves obtained with the two sets of parameters is significant only after the temperature exceeds 0.4 T_M; the two materials are nominally similar in composition and microstructure and hence one expects similar temperature dependence. In some of our experiments the temperature reached by the specimen was outside the range of the isothermal test data; using the exponential decay given before for temperatures higher than 0.6 T_M results in physically unrealistic values for the yield stress. Therefire, an arctangent function with appropriate scaling which still mimics well the yield stress drop at 0.5 T_M but levels off for temperatures higher than 0.6 T_M was used. Note that the rate-sensitivity parameters m and a have not yet been determined; the short duration current pulse tests discussed in Chapter 3 will be used to extract these parameters. The parameters for the model for both Al 6061-T6 and Cu 102 obtained with such calibration are listed in Table 4.1.

Table 4.1. Parameters for the viscoplastic model in Eq. (4.5)

Al 6061-T6		
	Bilyk et al.	Best fit to Expt
β	0.23	0.12
κ	1.9	3.0
m	22	20
a	20	20
E - GPa	72	72

Cu-102		
	Bilyk et al.	Best fit to Expt
β	0.25	0.065
κ	1.3	3.0
m	25	26
a	21	20
E - GPa	104	104

4.2.2. SOLUTION PROCEDURE

The nonlinear model in Eq.(4.5) is solved using a finite difference approach that requires certain simple modifications to account for lack of force data for the first 2 ms and temperature data beyond 2 ms. The total strain across the fixed gage length, ε_{DIC}^{i+1}, is known at every time step. So, for the first 2 ms, the unknown elastic strain increment is written in terms of the known thermal, and viscoplastic strains as follows:

$$\varepsilon_E^{i+1} = \varepsilon_{DIC}^{i+1} - \varepsilon_T^{i+1} - \varepsilon_p^{i} - \dot{\varepsilon}_p^{i} \cdot dt \tag{4.8}$$

where a simple forward integration in time is used for the viscoplastic strain evolution. Between 2 and 20 ms the thermal strains are not measured, but the temperature may be assumed to be constant. This is easily justified by examining the variation of thermal strains in the purely elastic tests. Therefore in this time interval, the unknown plastic strain increment can be estimated directly from measurements without any model

$$\varepsilon_p^{i+1} = \varepsilon_{DIC}^{i+1} - \varepsilon_T^{i+1} - \varepsilon_E^{i+1} \tag{4.9}$$

Note that this must also be consistent with the predictions of the viscoplastic model. Beyond 20 ms, the load and strain readings are used to calculate the thermal strain recovery accurately while any further plastic accumulation is still captured through the viscoplastic model. This can be written as:

$$\varepsilon_T^{i+1} = \varepsilon_{DIC}^{i+1} - \varepsilon_E^{i+1} - \varepsilon_p^{i} - \dot{\varepsilon}_p^{i} \cdot dt \tag{4.10}$$

Therefore, from the measurements of the total strain, as well as the temperature and load, a well calibrated viscoplastic model may be used in Eqs. (4.5), (4.8) and/or (4.10) to determine the plastic strain variation with time.

4.3. Viscoplastic Analysis of Response of Cu-102

The viscoplastic model discussed above is now used to examine the experimental results presented in Section 3.6 – 3.8. Only experiments where some plastic strain accumulation was observed will be analyzed since the thermoelastic response seen in Section 3.6.1 is quite straightforward to interpret. Cu-102 is considered in this section; the Al 6061-T6 displays additional thermal effects and is discussed in Section 4.4.

4.3.1. FIXED-GRIP LOADING

The first test to be analyzed is the one performed on Cu-102 at fixed grips conditions. In this test the specimen was loaded to the plastic range ($\sigma = 270$ MPa) and pulsed with a current to increase the temperature to 600 K. This corresponds to the result shown in Figure 3.11, where the total strain across the gage length, as measured by DIC is shown. In Figure 4.3, this result is repeated (by the blue line); in addition, the elastic strain drop caused by the drop in load (calculated from the load measurement beyond 2 ms) and the strain due to thermal expansion (calculated from the Rogovski coil measurement and extended to larger times through Eq.(2.4)) are also shown by the green and red lines, respectively.

The viscoplastic model can be used to determine the time evolution of the plastic strain using the following the procedure: For $t < 0.002$ s, the total and thermal strains are measured; therefore, Eq.(4.8) is used to calculate the partition between the elastic and plastic strains. For $0.002 < t < 1$ s, the total and elastic strain components are measured; therefore, Eq.(4.10) is used to calculate the partition between the thermal and plastic strains. The resulting calculation of the plastic strain with time is shown in Figure 4.3 by the black line. Note that for $0.002 < t < 1$ s, the thermal strain can also be estimated by using Eq.(2.4); in this case, the plastic strain accumulation can be calculated directly from the experiments without the need for a viscoplastic model; the result of this calculation is shown in Figure 4.3 by the gray line and is seen to agree well with the predictions of the viscoplastic model.

Finally, the viscoplastic model indicates that a residual plastic strain of 0.00248 is accumulated in the specimen; this compares well with the 0.00252 plastic strain that was measured in the specimen after an elapsed time of 10 s. The simulation was repeated for the second and third current pulse experiments indicated in Figure 3.13. The comparison of the predicted and measured plastic strain evolution is shown in Figures 4.4 and 4.5.

Once again, the model prediction is quite good; in particular the model confirms the absence of plastic strain accumulation in the second and third cycles.

There are two observations that can be made from these results: first, plastic strain accumulation occurs simultaneously with the temperature increase, with all changes in the time interval $0.002 < t < 1$ s being thermoelastic; very simply, the time rate of change of all quantities is very small outside this time window and there is no accumulation of plastic strain. Second, the heating duration appears to be sufficient to reach isothermal conditions in the specimen; this is probably why subsequent cycles do not show any strain accumulation. Higher temperatures and shorter heating cycles are needed to explore these aspects more completely, but are outside the range of the capacity of the experimental apparatus.

4.3.1. DEAD-WEIGHT LOADING

Analyzing the data from the fixed grips boundary conditions, it became clear that, due to the specific boundary conditions, the magnitude of plastic strain accumulation is limited by the imposed displacement and the compliance of the loading system to less than one percent strain in most cases. This limitation, however, is avoided in the tests performed at dead weight loading conditions. In this case, in fact, the material is allowed to accumulate plastic strain for as long as the yield stress – for the particular temperature it was heated at – lies below the stress corresponding to the particular dead load. Sufficient strain accumulation to result in failure of the specimen is seen in Figure 3.25. The viscoplastic model is now used to track the strain evolution in these dead-weight loading experiments.

Before proceeding with the analysis, a physical interpretation of strain accumulation under fixed load is provided in Figure 4.6. The specimen, initially at room temperature and at a stress level σ_0 (green dot) is heated by the electric pulse to a temperature $T_1 = 423K$. Due to the rise in temperature, the entire stress strain curve shifts to a lower level as indicated in the figure. At this point, the material experiences an overstress (red arrow) which drives the plastic strain accumulation to the equilibrium point marked by the blue dot. The dynamic oscillations observed in the experiments may influence this overstress and this aspect will be examined later. Whether the specimen reaches this equilibrium point or not depends on how long the temperature is maintained at the elevated level. This evolution can be determined quantitatively using the viscoplastic model.

The time variation of the total strain across the gage length as measured by DIC is shown in Figures 3.24 and 3.25. In Figures 4.7 – 4.10, these results are repeated by the blue lines; in addition, the elastic strain oscillations caused by the drop of the load (calculated from the load measurement beyond 2 ms) and the strain due to thermal expansion (calculated from the Rogovski coil measurement and extended to larger times) are also shown by the green and red lines, respectively. First of all compatibility in Eq. (4.4) can be applied to find the plastic strain after 2 ms (due to the noise in the load signal during the discharge) until about 200 ms; this result is shown by the gray line. After 300 ms the assumption of constant temperature is not valid but due to the saturation of plastic accumulation within 100 ms, this region is not relevant to this study. The viscoplastic model can be used to determine the time evolution of the plastic strain using the same procedure described above for the fixed-grip tests in Section 4.3.1; the only variation to the previous procedure is that compatibility will be used to calculate the load trace at all times. The resulting calculation of the plastic strain with time is shown in Figures 4.7 – 4.10 by the black lines. For the test at 370K, a complete recovery is observed, while for the tests at higher temperatures, increasing plastic deformation is observed. Finally, the viscoplastic model indicates that a residual plastic strain of increasing amount accumulates in the specimen at the end of each test at increasing temperatures; this accumulation compares well with the plastic strain accumulation history calculated with compatibility as well as with the strain that was measured in the specimen after an elapsed time of 10 s, shown in these figures as a black filled symbol. Note that in this procedure the load is computed with compatibility at each time step while the plastic strain rate is found with the viscoplastic model. This approach was necessary to stabilize the simulation; in fact if the plastic strain accumulation is driven by the load readings it will cause the plastic strain to accumulate much faster than expected. This response is due to the nature of the model which incorporates an exponential dependence of the plastic strain rate on the overload; this means that small errors in the load reading cause a large perturbation in the plastic strain rate giving erroneous estimates. However it is important to observe that the computed stress level compares well with the values found experimentally.

The specimen heated to 650K failed after a total accumulated plastic strain of about 0.08. Similar tests at other fixed load levels shown in the Appendix were also simulated; the predictions of the viscoplastic model provided a good estimate of strain accumulation with heating pulses.

The large plastic strain accumulation that is seen in the constant load tests appears at timescales that are quite different from that observed in the fixed-grip tests. This is easily interpreted in terms of the viscoplastic model. For the fixed grip tests, plastic strain accumulates only when there is an imbalance between the rates of thermal expansion (which depends on the temperature history) and the rate of elastic unloading (which depends on the grip compliance). This occurs in the 2 ms duration of the current pulse; beyond this time, the load drops significantly below the yield point and hence plastic strain accumulation occurs only during the 2 ms pulse time. In contrast, for the constant load tests, there is little accumulation of plastic strain in this time scale; rather, plastic strain accumulates during the time interval of 10 to 30 ms, when the temperature is near the peak and the load is nearly constant, above the flow stress appropriate to this temperature, as indicated in Figure 4.6.

4.4. Viscoplastic Analysis of Response of Al 6061-T6

The experimental results on Al 6061-T6 alloys were also interpreted using the viscoplastic analysis discussed in Section 4.2; since a higher fraction of the melting temperature was attained in this material, additional considerations concerning annealing need to be introduced in order to capture the response correctly.

4.4.1. FIXED-GRIP LOADING

The experiments on Al 6061-T6 reported in Figures 3.16 - 3.17 and Figures 3.18 - 3.19 are considered next. The time variation of the total, thermal, elastic and plastic strain components are shown in Figures 4.11 - 4.14 for the first and second pulse cycles at each temperature. The predictions of the viscoplastic model agree very well with the experimental measurements for T = 500 K; in particular the accumulation is predicted correctly. However, accumulation of plastic strain is observed in both the first and second cycles and is captured well by the viscoplastic model. Therefore, it may be concluded that the viscoplastic model is appropriate for this material at this temperature. The fact that viscoplastic accumulation does not saturate as observed in the case of Cu-102 is puzzling and requires further examination. For the test at T = 580 K, with $T = 0.6T_M$, the measured strain variation could not be captured by the viscoplastic model without altering the rate-sensitivity parameter m. These results suggest that the viscoplastic model is appropriate when the maximum temperatures are below about 500K, but additional effects – such as flash annealing - may be important at higher temperatures.

4.4.2. DEAD-WEIGHT LOADING

The strain variation for the dead-weight loading tests on Al 6061-T6 are shown in Figures 4.15 – 4.18. The viscoplastic model is used to obtain the partition between the elastic, thermal and plastic strains for each test. At a maximum temperature of 380K, the response is thermoelastic, with complete recovery of the strains; the plastic strain estimated from the viscoplastic model is negligible. At a maximum temperature of 500 K, significant plastic strain accumulation occurs in the time scale of 10 to 30 ms and saturates at about 0.0072; the viscoplastic model indicates an accumulated plastic strain of 0.00705. The saturation of plastic strain at about 30 ms is due to the drop in the overstress as illustrated in Figure 4.6. Note that the viscoplastic model is forced to accumulate strain by imposing the measured total displacement. With further increase in temperature to 580K, the specimen fails with a total plastic strain increment of 0.08. The viscoplastic model provides a good estimate of the residual strain at the end of each pulse if the measured total strain is used along with Eq.(4.8) to calculate dynamic load fluctuations; this is similar to the fixed grip experiments discussed in the previous section. It is suggested that this variation in the response of the fixed grip experiment above 500K may be due to flash annealing of the aluminum alloy. This aspect is considered next, but only from a qualitative perspective; no models of this behavior are generated.

4.4.3. FLASH ANNEALING OF AL 6061-T6

The Al 6061-T6 specimens were subjected to temperatures as high as $0.6T_M$; this amounts to heat-treating the alloy over extremely short durations. In a typical test, the temperature is increased to T_M and held for about 300 ms. Is it possible to cause microstructural changes and “flash anneal” or “flash age” the alloy? This is explored through a series of experiments.

Annealing is the process in which a material is heated to a high temperature, well below T_M, but sufficiently high to increase atomic mobility and drive microstructural changes, and held for an extended amount of time and then slowly cooled back to room temperature. The effect of this treatment is to soften the material; this is achieved in three stages: recovery, recrystallization and grain growth. To completely anneal an alloy, such as aluminum Al 6061-T6, it is typically exposed to a temperature of about 773 K for about 2 hours and slow cooled to 673 over one hour; this has the effect of reducing the yield stress from about 300 MPa to less than 100 MPa. From examination of the solidus for the Al 6061, it is clear that such annealing could occur if the peak temperature is greater than 550 K, but the hold time may have to be longer because of the reduced mobility. Typically, time scales associated with recovery could be short, but recrystallization and grain growth are diffusion controlled and are very slow.

Aging treatments for Aluminum alloys imply heating to temperatures above 373 K and holding for a few minutes to hours in order to allow precipitates to form and grow. Typically the Al 6061-T6 is peak aged by holding the temperature for an optimal time. Aging for longer times will decrease the yield stress. In the present experiment the temperature is increased to ~400 – 640 K, but for duration for less than one second. Could this treatment contribute to over aging the Al 6061-T6?

In the previously discussed experiment, the temperatures reached were close to that required for annealing/aging, but the time the specimen spent at this state is on the order of a second. To estimate the amount of macroscopic yield stress reduction, if any, different specimens were pulsed with a T_M = 580 K, with an increasing number of discharges, from a single pulse up to 30 pulses, allowing sufficient time for the specimen to cool down to room temperature between pulses. Those pulses were supplied without the addition of any mechanical load. Each specimen was then carefully removed and tested to failure to extract the stress strain response. Results of this procedure are plotted in Figures 4.19.

From these experiments it became evident that when pulsed with lower current levels that cause a rising temperature no greater than 500 K, even after 30 pulses, the material maintained its yield and flow properties. If, however, the current level is increased, bringing the maximum temperature to about 580 K, the yield stress drops significantly during the first five pulses, leveling to a steady value of 260 MPa thereafter. If we consider that each pulse cycle keeps the specimen at 580 K for about 300 ms, it suggests that flash-annealing or flash-aging can occur even within the duration of this order. This behavior must clearly influence the large strain accumulation observed in the Al 6061-T6 for tests with T_M in the range of 540K and above. Unfortunately, no quantitative models are available of this flash annealing/ flash aging process and hence this effect is not incorporated into the viscoplastic model described above.

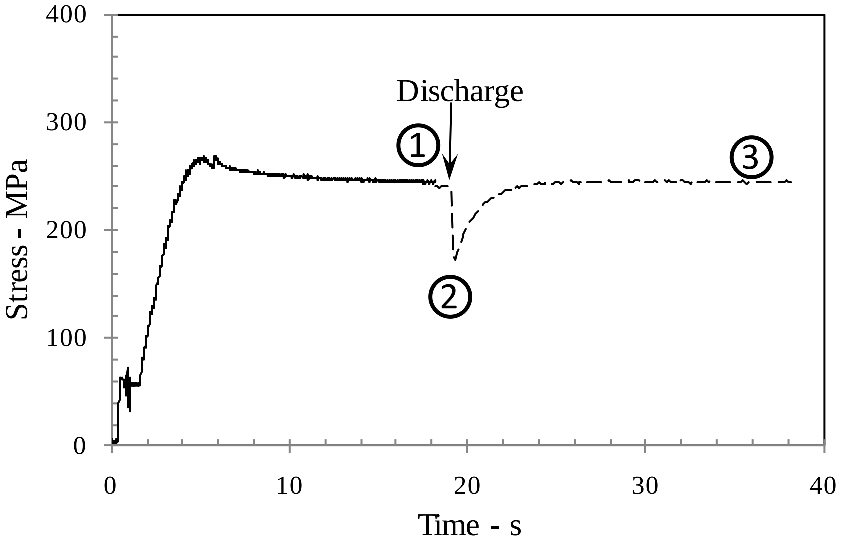

Figure 4.1. Schematic representation of the experiment. The numbers represent the stages of the test while the time the pulse was applied is pointed by the arrow.

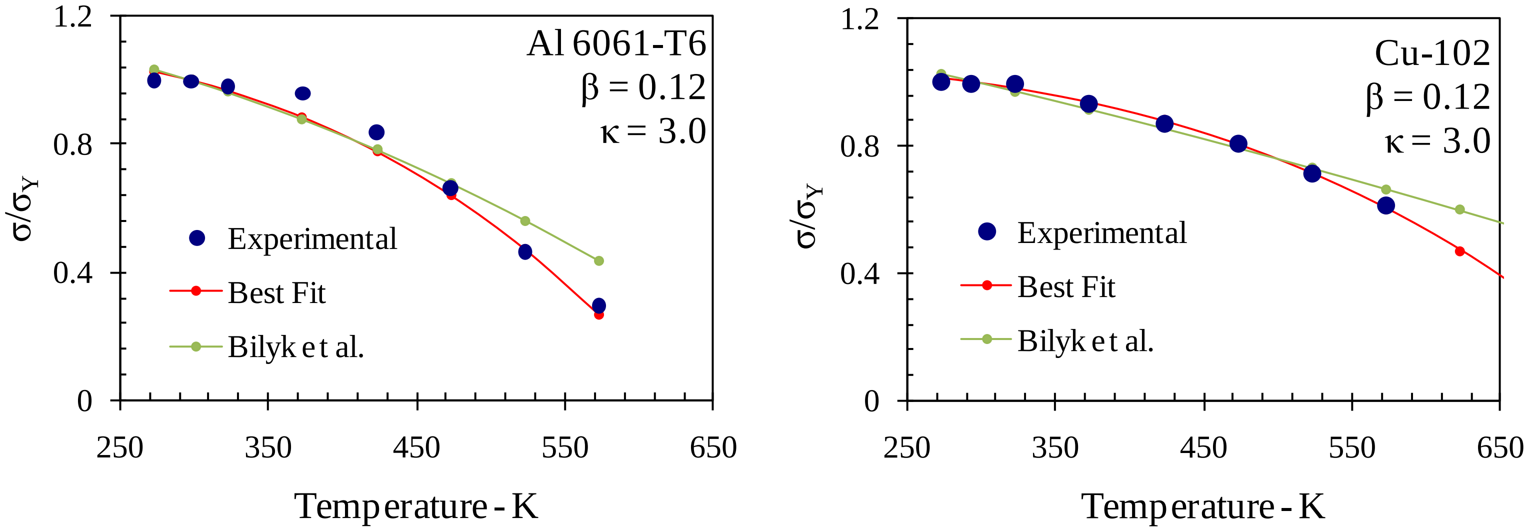

Figure 4.2. Yield stress as a function of temperature normalized by its value at room temperature. The blue line is the experimental measurement and the red line is the fir using the parameters listed. The green line is the fit used by Bilik et al.

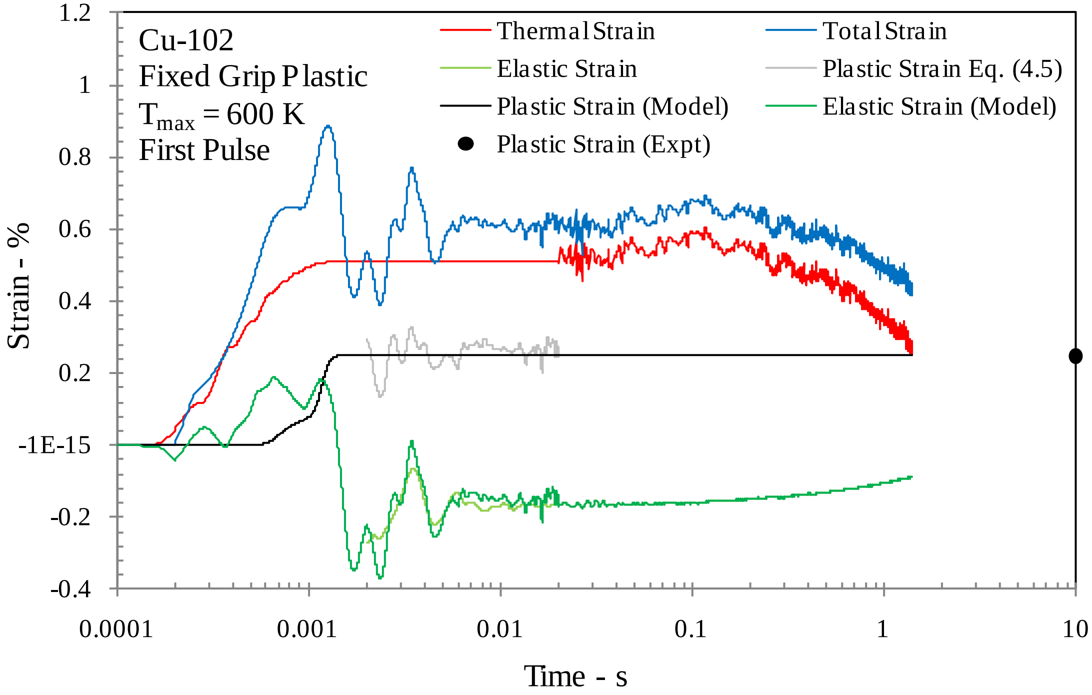

Figure 4.3. Comparison of the response predicted by the viscoplastic model. All the quantities are expressed as strains to allow visualization on the same scale.

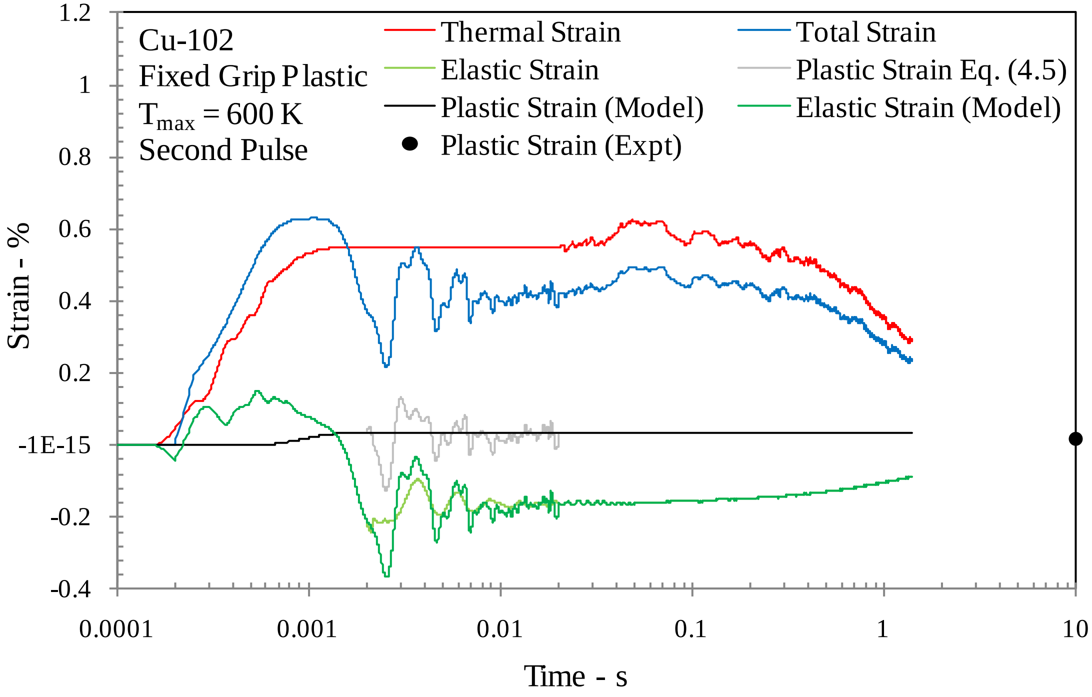

Figure 4.4. Comparison of the response predicted by the viscoplastic model. All the quantities are expressed as strains to allow visualization on the same scale.

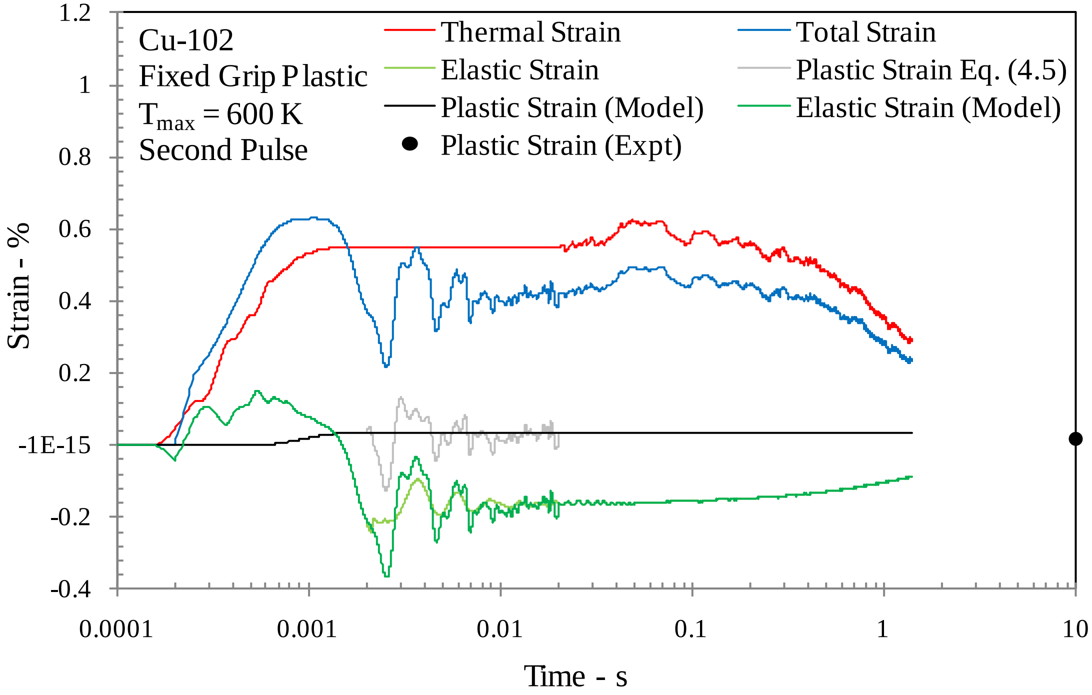

Figure 4.5. Comparison of the response predicted by the viscoplastic model. All the quantities are expressed as strains to allow visualization on the same scale.

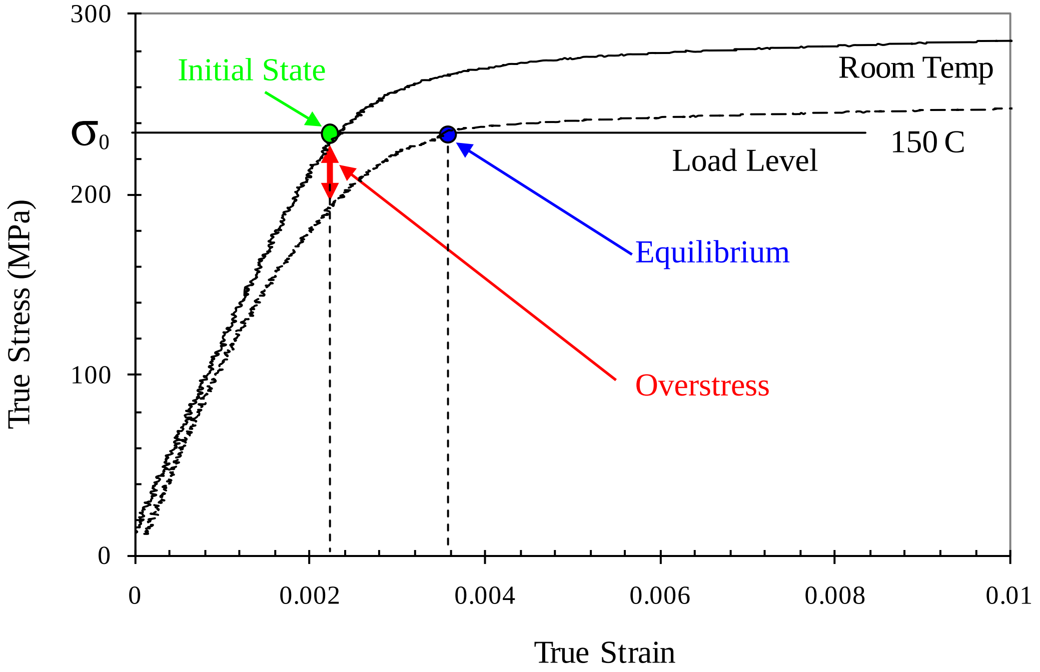

Figure 4.6. Plastic strain accumulation mechanism.The two curves are isothermal stress strain at room temperature and at 150°C and the horizontal line is the constant load level throughout the experiment. Initial state is the strain and load at room temperature and the equilibrium point is the strain level corresponding to the load at the maximum temperature reached during the discharge.

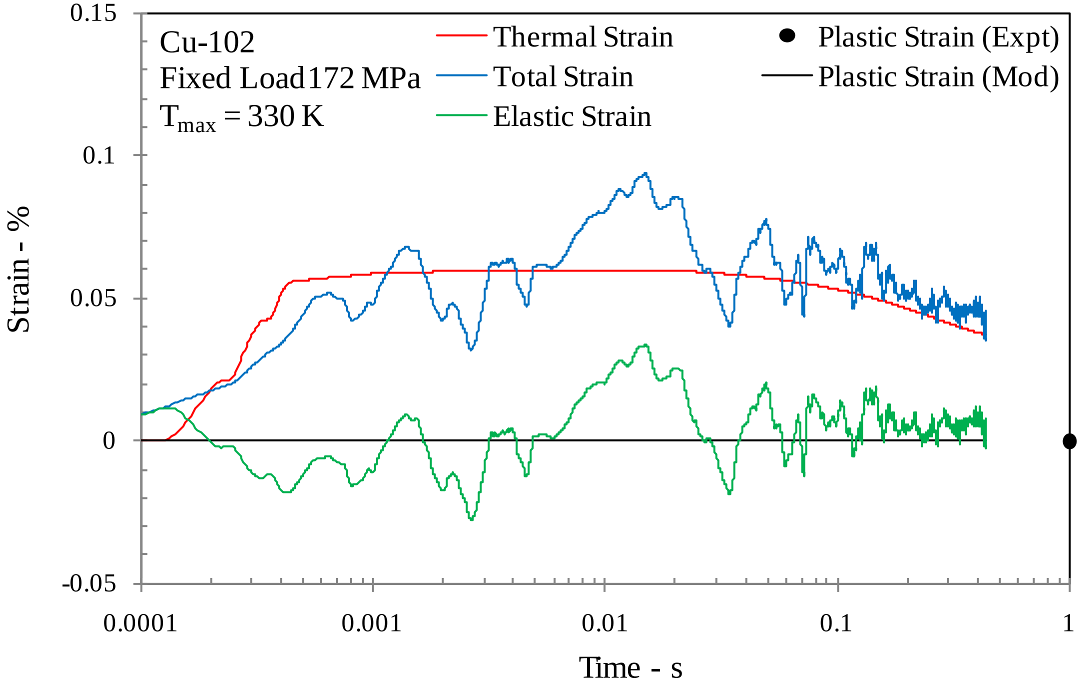

Figure 4.7. Comparison of the response predicted by the viscoplastic model.

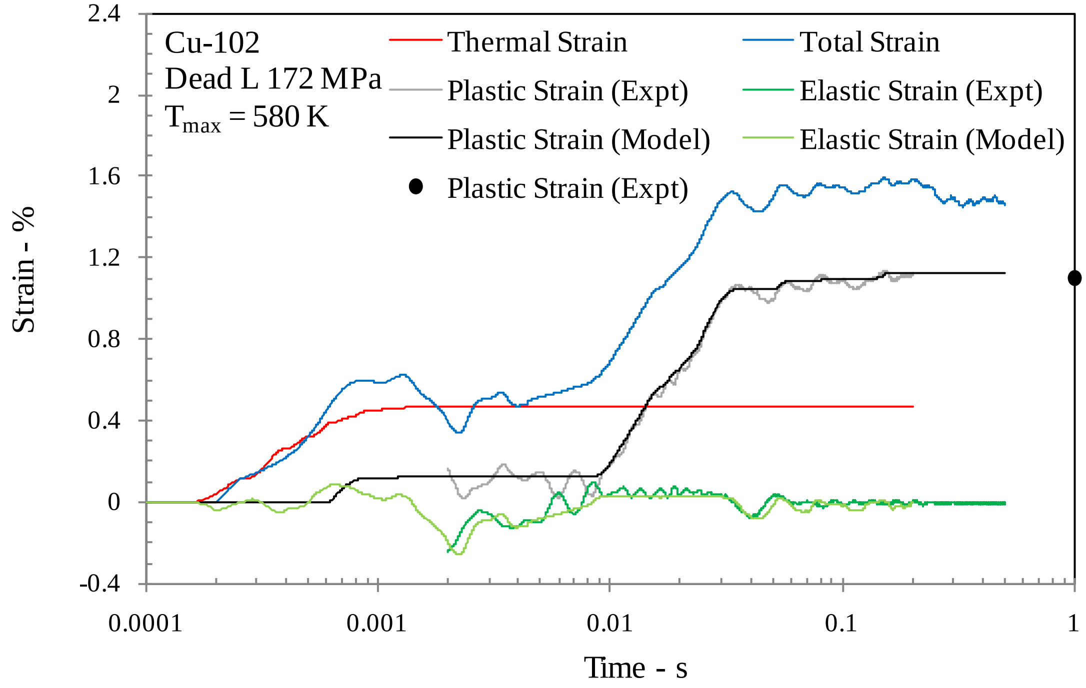

Figure 4.8. Comparison of the response predicted by the viscoplastic model.

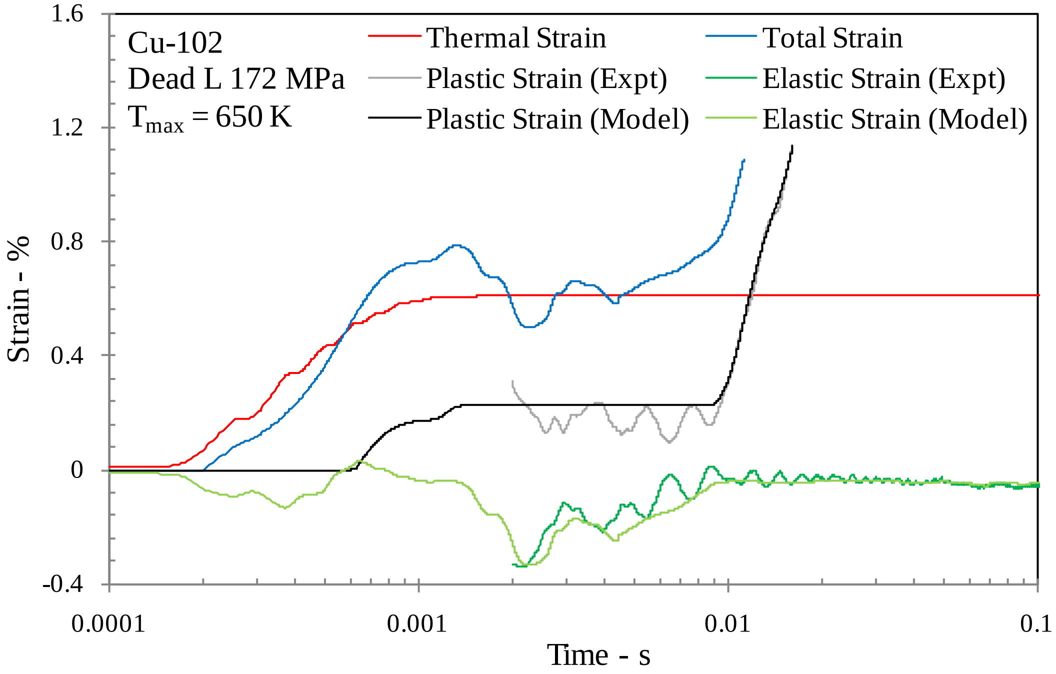

Figure 4.9. Comparison of the response predicted by the viscoplastic model.

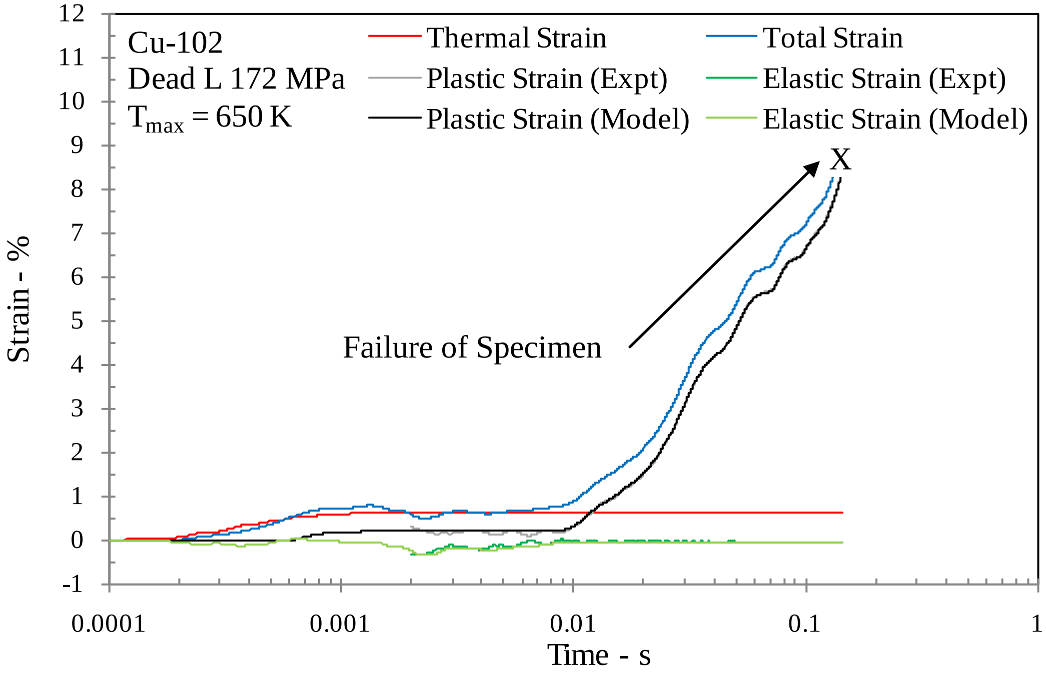

Figure 4.10. Comparison of the response predicted by the viscoplastic model.

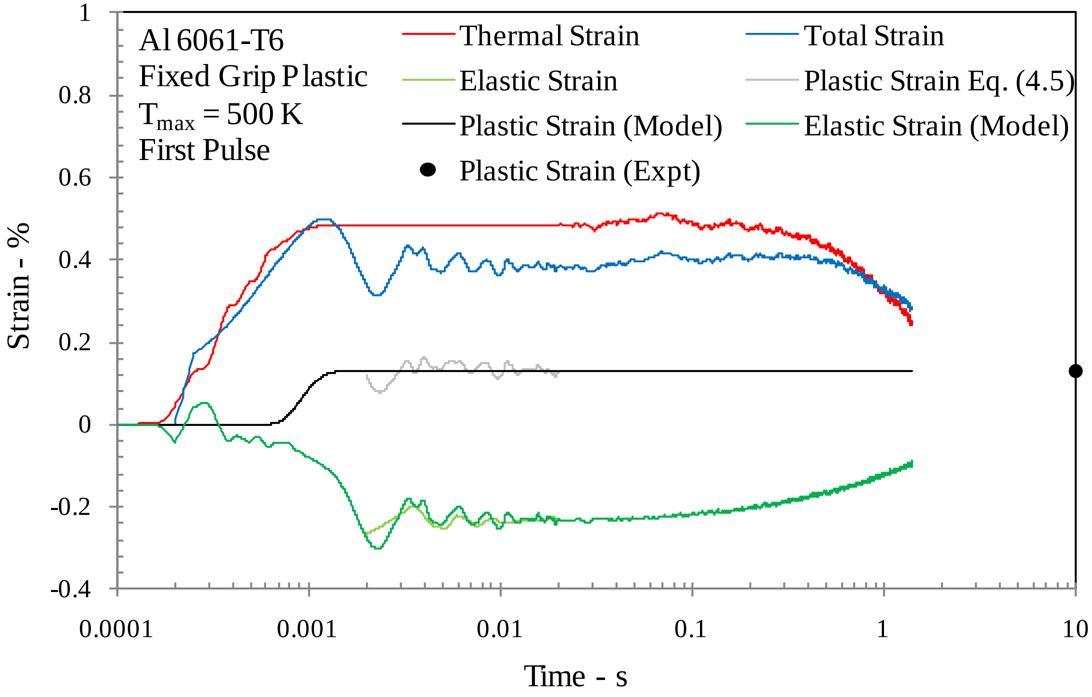

Figure 4.11. Comparison of the response predicted by the viscoplastic model.

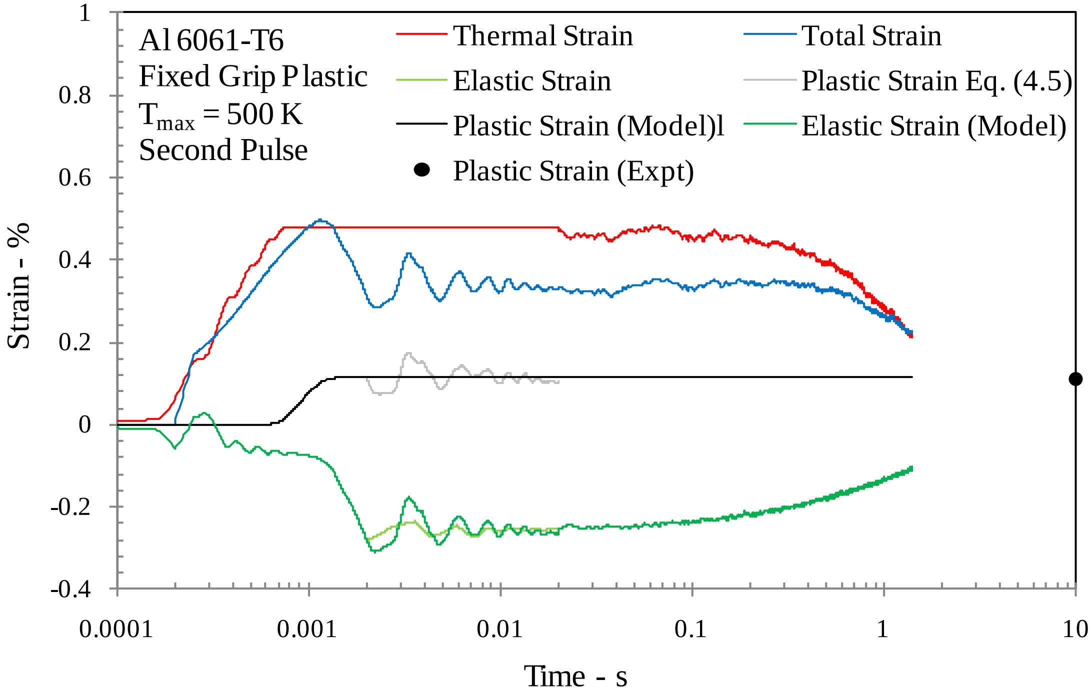

Figure 4.12. Comparison of the response predicted by the viscoplastic model.

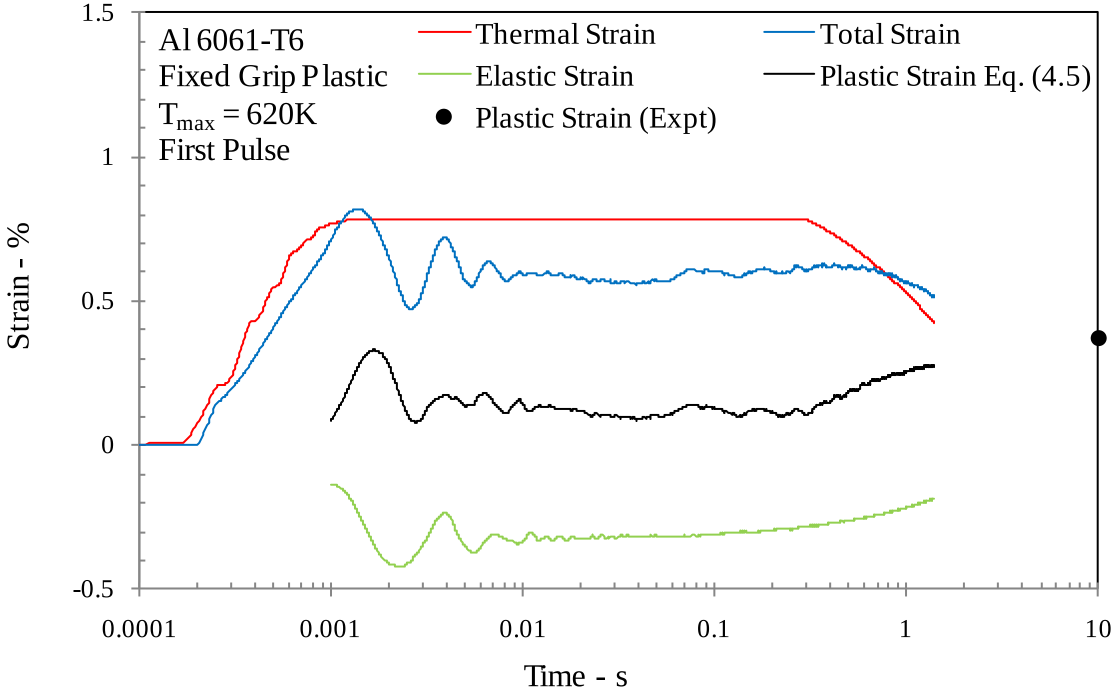

Figure 4.13. Comparison of the response predicted by the viscoplastic model.

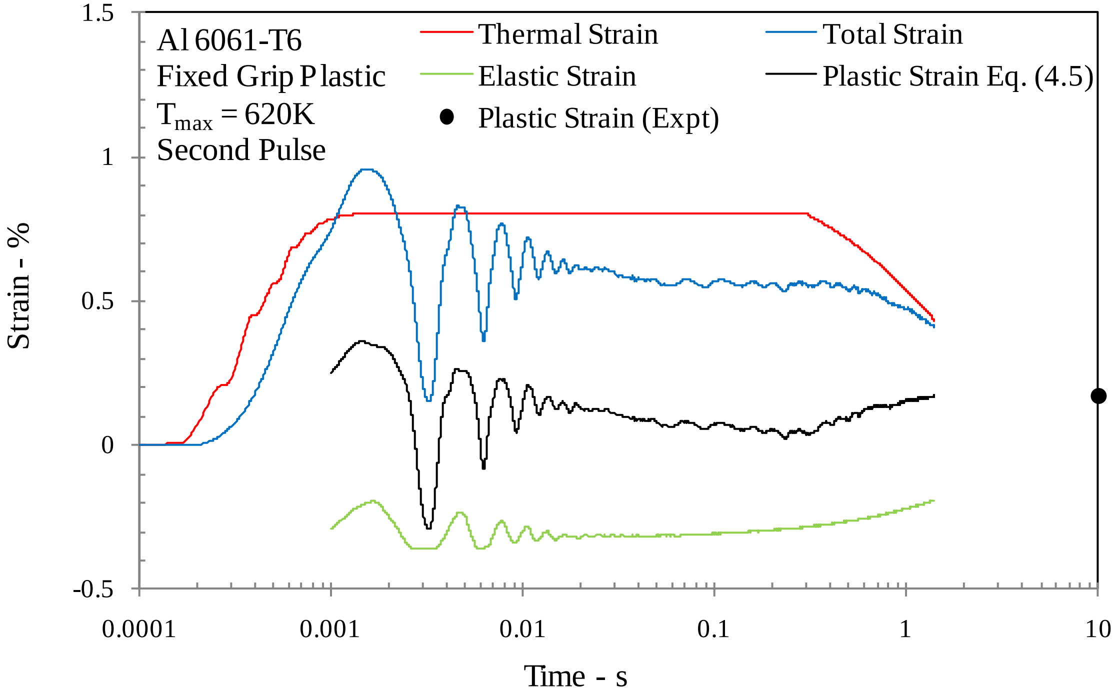

Figure 4.14. Comparison of the response predicted by the viscoplastic model.

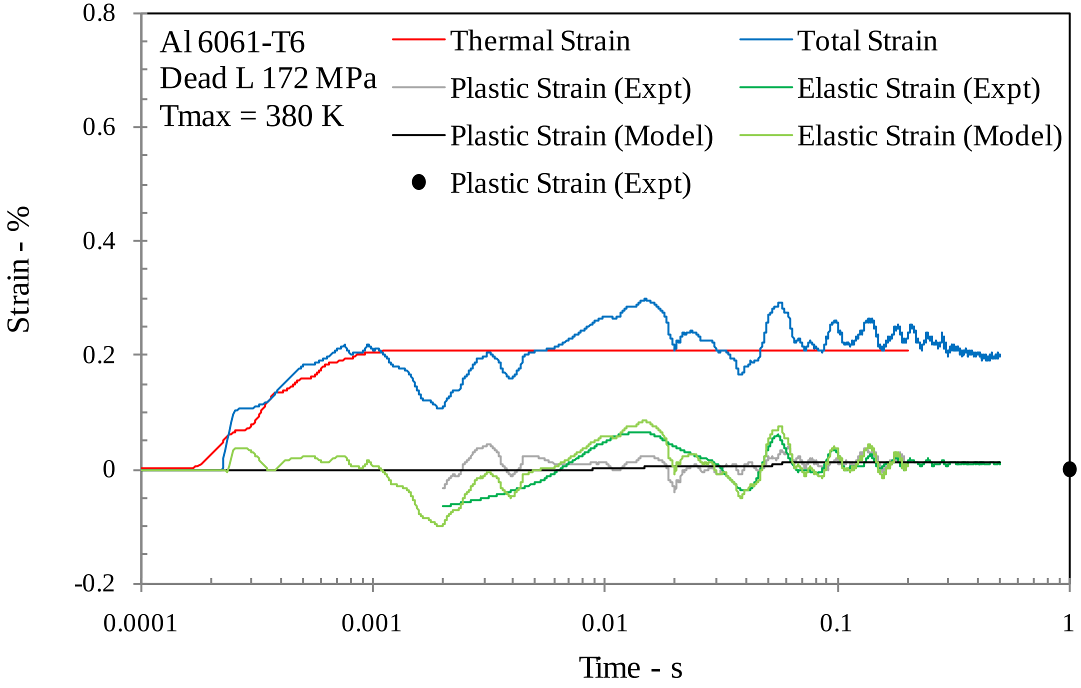

Figure 4.15. Comparison of the response predicted by the viscoplastic model.

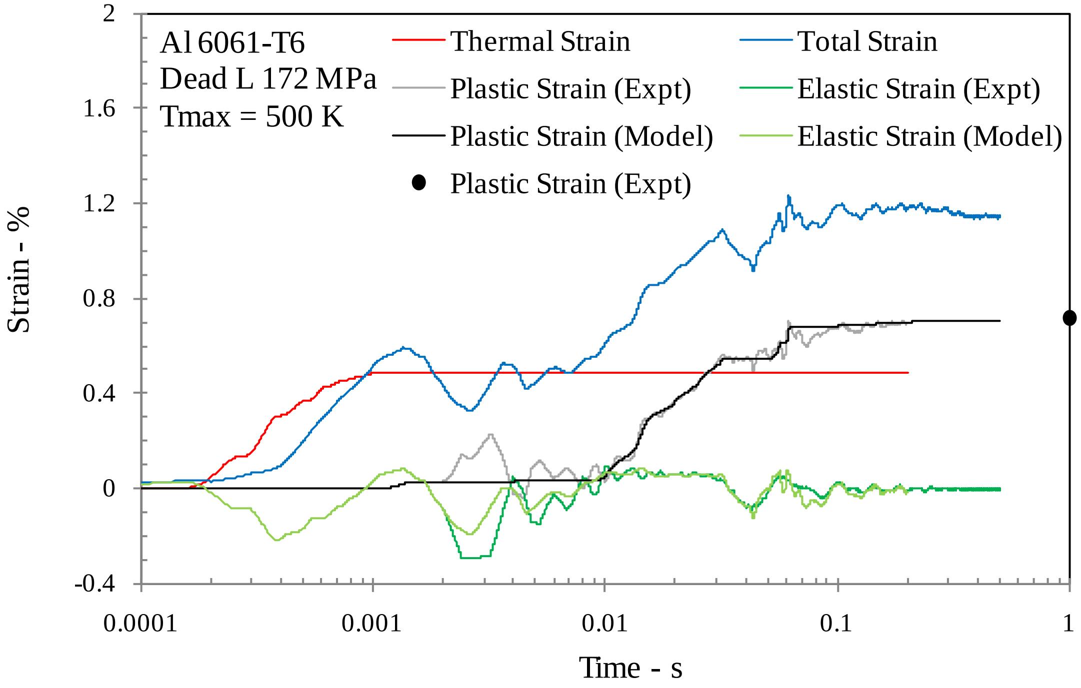

Figure 4.16. Comparison of the response predicted by the viscoplastic model.

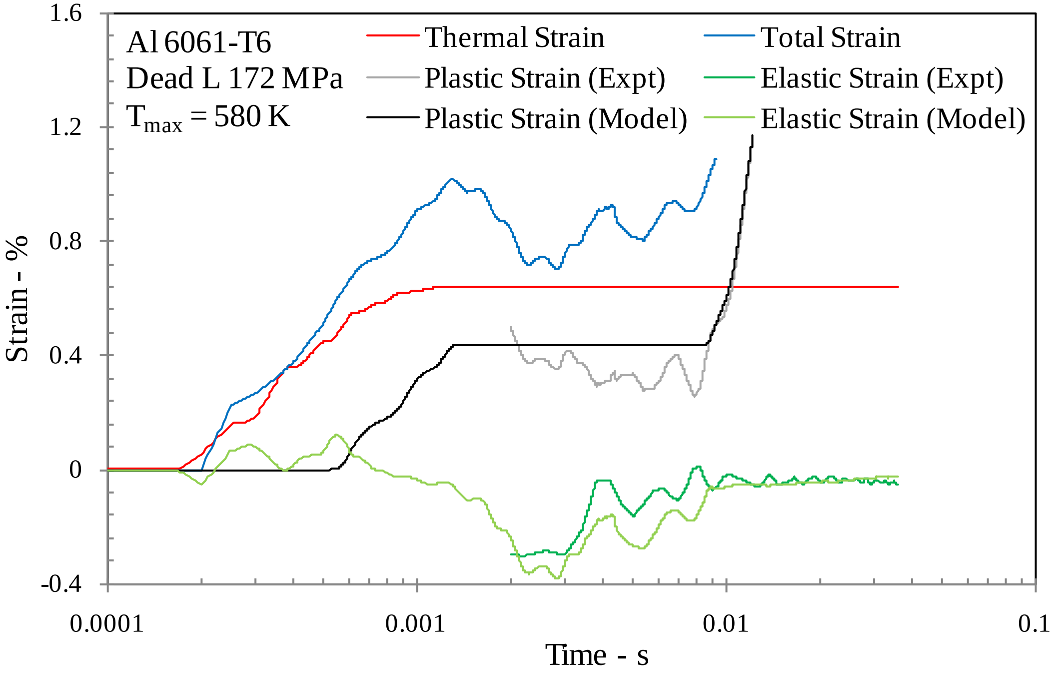

Figure 4.17. Comparison of the response predicted by the viscoplastic model.

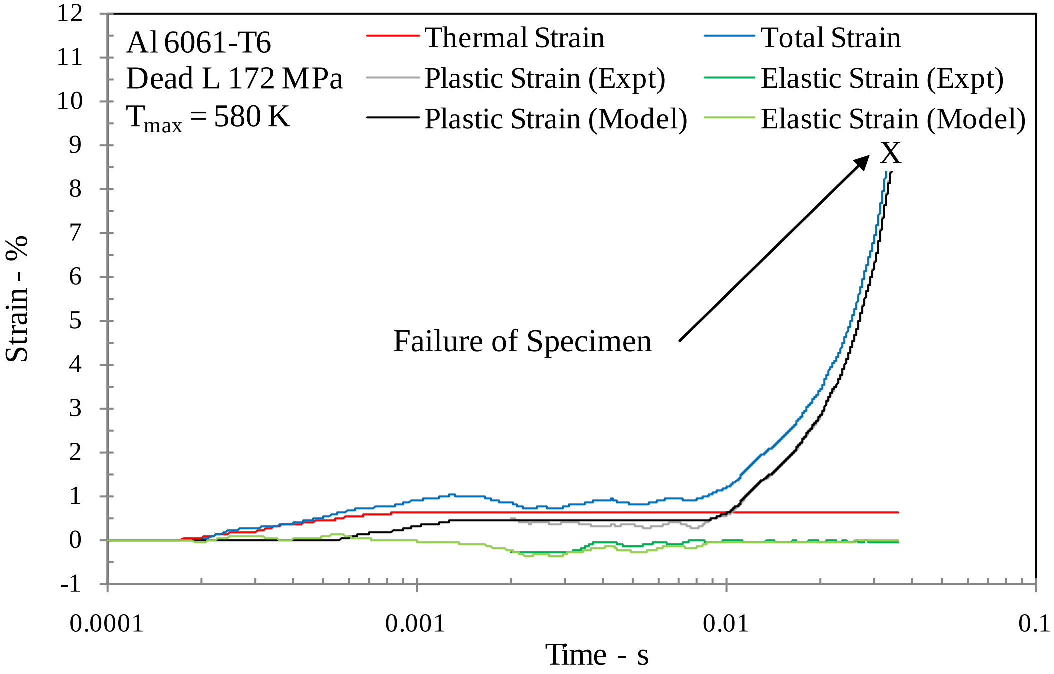

Figure 4.18. Comparison of the response predicted by the viscoplastic model.

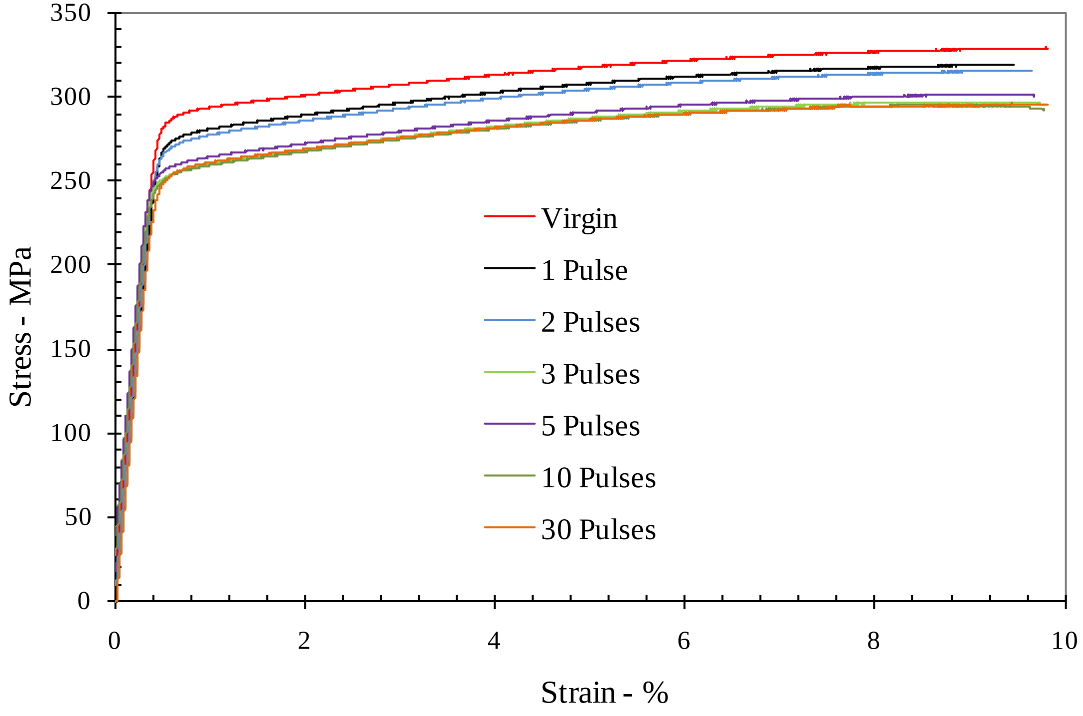

Figure 4.19. Stress strain curves for specimens exposed to different number of current pulses.

5. EFFECT OF PULSED CURRENT THROUGH A DAMAGED CONDUCTOR

The main aim of this section is to examine the behavior of a conductor with damage or defect in the form of a crack under loading conditions similar to that used in Chapter 3. The motivation behind this study is that, as discussed in the Introduction, the presence of a defect, such as notches, cracks or voids, localized material damage occurred once the conductor was pulsed with high current discharges. This damage consisted in metal melting and ejection from the vicinity of such defects.

The fundamental experiment performed in this work consists of loading an electrically conductive specimen to a predetermined remote load and subsequently discharging a short-duration, high-intensity current pulse through it. The response of the specimen is monitored though multiple diagnostics – electrical, thermal and mechanical. For this purpose specimens were designed as described in Section 2.1 to provide connections for mechanical and electrical inputs simultaneously. Each specimen was cut by electric discharge machining (EDM) to be 10 mm wide and approximately 30 mm long starting from a 0.8 mm thick sheet; a 1 mm long single edge notch (SEN) was introduced in the middle of the specimen; the width of the EDM notch was 0.4 mm resulting in a crack tip radius of about 0.2 mm. A natural fatigue crack, approximately 1 mm long was created by cyclic loading. In some of the specimens tested, the EDM notch was set to be 4 mm long without a fatigue crack.

The crack tip region was monitored with a Phantom v7.3 high speed video camera in order to observe the macroscopic effects of the current discharges and to evaluate the onset of damage. The camera was equipped with a macro lens arrangement to magnify the image eight times. This camera is capable of recording 50 thousand pictures per second with a 125 x 512 pixel window size for a duration of about half a second. The overall field of view of the camera was about 1 mm high and 2.8 mm wide. A grating with a one mm pitch was marked on the specimen in order to identify the position of the crack tip.

A typical experiment aimed at identifying the crack tip damage under combined electromechanical loading is described below. First, the specimen is mounted in the special grips and subjected to mechanical load. A constant crosshead displacement rate of 1.27 mm per minute – corresponding to a strain rate of 10^{-3} s^{-1} – is used to reach the desired load level, selected to be some fraction of the failure load. The variation of load with time is acquired by the data acquisition system every 0.1 seconds. Next, the crosshead is stopped at the desired load level and the system is allowed to settle down to a steady state; the load is continuously monitored during this stage. Finally, the capacitor bank is charged to the desired voltage level and discharged by triggering the ignitron. The high speed camera and the oscilloscope that records the Rogovski coil output are triggered synchronously. If crack extension/melting does not occur under this current pulse, the charge voltage in the capacitor bank is increased in steps of 500 V and discharged through the specimen at the same mechanical load until crack extension/melting is observed. This sequence of events is repeated corresponding to different load levels in order to identify the damage threshold conditions at different load levels. After the test, the region in the vicinity of the crack was inspected with a high magnification microscope; the appearance of the crack tip at the failure threshold is shown in Figure 5.1. A small crack/hole is observed near the crack tip; it is possible to observe in the video images that a part of the crack tip region melts and this molten material gets ejected in a radial direction away from the crack tip[2]. It appears that this is due to the Lorentz force developed during the discharge. It was also observed that the molten metal from the interior of the specimen gets pushed out along the crack front and then out radially; there could be some three-dimensional aspects to the ejection of the molten metal as we show in Section 5.3. The failure criterion for the combined mechanical and electrical problem can now be analyzed by considering the mechanical and electrical fields and examining the energy flow to the crack tip region.

The data from the above experiment were interpreted to indicate whether or not the values of the load and current level – expressed as $\left(\sigma^{\infty}, j_{\max}^{\infty}\right)$ – produced any visible melting and/or ejection of material from the crack tip; the failure threshold values are denoted as $\left(\sigma^{c}, j_{\max}^{\infty,c}\right)$. It should be noted that $\left(\sigma_{cr}, 0\right)$ corresponds to failure under pure mechanical loading. On the other hand, when subjected to a current pulse without mechanical loading, melting/ejection occurs at a critical value of the current: $\left(0, j_{cr}^{\infty}\right)$ corresponding to pure electrical failure. For combined mechanical and electrical input, the results indicate the interaction between the two critical quantities. This interaction

---

[2] Videos of two experiments are available in the attachments of this dissertation.

between the electrical and mechanical damage can be explored further through an analysis of the stress and current fields in a normalized sense, considering the effect of the crack tip as described in the next section.

5.1. Physical Description

This experiment involves the coupling of multiple physical fields: mechanical, electrical, magnetic and thermal. These fields interact with each other in complex ways and cause failure; analysis of this interaction and its role in the onset of failure is the main problem of interest. The general behavior of each of these fields will be described briefly in an attempt to draw connections between them and motivate the interpretation of failure.

The simplest field to analyze is the mechanical field near the crack tip due to a load applied across the crack. The mechanical loading on a cracked specimen creates a stress singularity that may be handled within the theory of linear elastic fracture mechanics. The specimen geometry and mechanical loading are indicated in Figure 5.2; this corresponds to a single-edge-notched (SEN) tension specimen. The stress intensity factor due to a uniform far field stress σ^{∞} in this specimen is given by the following expression (Tada et al., 1973):

$$K_I = \sigma^{\infty}\sqrt{\pi a}\, f\left(\frac{a}{W}\right) \tag{5.1}$$

$$f\left(\frac{a}{W}\right) = \sqrt{\frac{2W}{\pi a}\tan\left(\frac{\pi a}{2W}\right)}\,\frac{0.752 + 0.202\dfrac{a}{w} + 0.37\left(1 - \sin\left(\dfrac{\pi a}{2W}\right)\right)}{\cos\left(\dfrac{\pi a}{2W}\right)} \tag{5.2}$$

where σ^{∞} is the stress in the uniform region and W and a are the specimen width and crack length, respectively. Under purely mechanical loading, the cracked specimen will fail when the value of the applied K_I equals the fracture toughness K_c of the material; fracture toughness values for the Al6061-T6 and Cu102 used in the present work are given in Table 2.1. Note that for the 1 mm thick specimens used in this study, a large plastic zone develops near the crack tip; therefore, the values of toughness obtained here are not the “plane-strain fracture toughness” values of the material. Nevertheless, the stress intensity factor is used as the main interpretation of the mechanical loading in order to bring together the effect of both the loading and crack length in a simple way. In all the tests performed to explore the coupling of mechanical and electrical fields, K_I never exceeded $0.8K_c$.

For the conductors considered in the present work, the electric field is governed by the time independent Maxwell’s equations. This is justified by the fact that for the frequencies of interest (about 4.4 kHZ), the skin depth is on the order of the specimen thickness. In particular the electric field is given by $\mathbf{E} = \nabla\phi$, where $\mathbf{E}$ is the electric field and ϕ is the electric potential. The electric field is related to the current density vector $\mathbf{j}$ by Ohm’s law: $\mathbf{E} = \Omega\mathbf{j}$ where Ω is the electrical resistivity. Then the equation governing the electric potential is

$$\nabla^2\phi = 0 \tag{5.3}$$

The boundary conditions are set as follows: on the top and bottom boundaries, $\nabla\phi\cdot\mathbf{n}=\pm\Omega j^{\infty}\left(t\right)\mathbf{e}_2$, where $\mathbf{n}$ is the unit normal to the boundary, $\mathbf{e}_2$ is the unit vector in the x_2 direction, and $j^{\infty}\left(t\right)$ is the uniform current density distribution that is imposed at the upper and lower boundaries from the pulsed power supply. All the other boundaries, including the crack surfaces, have zero normal current imposed implying perfect insulation and hence we have $\nabla\phi\cdot\mathbf{n}=0$. This boundary value problem holds for steady state conditions and is utilized under the assumption that the electro-magnetic time constant is small in comparison to the rate of change of the boundary conditions. To solve for the electric field near the crack tip, an analogy with a mode III crack problem can be used; the analogy is evident by considering that for the latter problem the out-of-plane displacement u_3 is also governed by Laplace's equation with Neumann boundary conditions. From this analogy the two components of the current density vector j_1 and j_2 can be compared to the anti-plane shear stress components σ_{13} and σ_{23}, and the electric potential can be seen to be equivalent to the out-of-plane displacement u_3. The solution for the mode III crack problem can be found in Tada et al. (1973). From this analogy, the electric current field near the crack tip can be written as:

$$\left.\begin{aligned} j_1\left(r,\theta\right)&=-\frac{C_i}{\sqrt{2\pi r}}\sin\frac{\theta}{2} \\ j_2\left(r,\theta\right)&=\frac{C_i}{\sqrt{2\pi r}}\cos\frac{\theta}{2}\end{aligned}\right.\quad \text{as } r\to 0 \tag{5.4}$$

where (r,θ) represent the crack tip centered polar coordinates. The factor C_i will be called the *current intensity factor* (CIF) and plays a role that is somewhat analogous to the stress intensity factor in the mechanical problem. A similar definition was introduced by Mukherjee et al (1982). Note that Eq. (5.4) describes the electric current in the vicinity of the crack tip; the value of the CIF must be obtained from the complete solution to the boundary value problem described above; the complete solution to the mode III mechanical problem yields:

$$C_i = j^{\infty}\sqrt{\pi a}\, f_{III}\left(\frac{a}{W}\right), \text{ with } f_{III}\left(\frac{a}{W}\right) = \sqrt{\frac{2W}{\pi a}\tan\left(\frac{\pi a}{2W}\right)} \tag{5.5}$$

It is seen from the Eq.(5.5) that the current density field exhibits an inverse square root singularity just like the mechanical problem. In practice, such singular current density is not permissible; while the yield stress provides the physical limit to the stress in the mechanical problem, melting resulting from Joule heating provides the limit to the current near the crack tip. Just as the singular stress field is used in the mechanical problem under the assumption of "small scale yielding" where the yield zone is small in comparison to other length scales, the singular current field can be used in the electrical problem provided the size of the melt zone is small in comparison to other length scales. This will be discussed in Section 5.2 through numerical simulations.

The fracture criterion is examined assuming the validity of the singular electric field. There exists a large literature related to the crack propagation in piezoelectric materials; here the crack tip singularity is identified either in terms of electric displacement intensity factor, K_D (see for example, Landis 2004) or the electric field intensity factor K_E (see for example, Zhang et al 2003). Furthermore, the fracture criterion is posed in terms of the critical energy release rate. However, unlike the case of piezoelectric materials where the current is zero, in the conductors considered here, the current field causes two major differences. First, the electrical influence on the energy release is negligible in comparison to the elastic and fracture energies. Second, unlike the case of piezoelectric materials, the nonzero current causes continuous Joule heating and failure is primarily due to melting. Therefore, the energy accumulated over time in the crack tip region has to be considered. Note that in this formulation Lorentz forces that arise from the interaction of the electric and magnetic field are ignored; this may be very important to the material points near the crack tip, particularly if melting occurs.

Therefore, instead of examining the energy release rate as is typical in quasi-static fracture problems, the thermal effects that arise from the current concentration are considered. First, a real crack is not a sharp crack that generates a singular stress state but presents a certain length scale at which the "sharp crack" assumption does not hold. Even for a natural fatigue crack this dimension could be on the order of a few hundred nanometers; EDM cut cracks are significantly larger. This limits the current densities to finite values so as to make the field in Eq.(5.4) physically admissible away from the crack tip. Second, a coupling between the electrical field and the thermal boundary value problem has to be introduced because the current in the specimen generates an increase in the temperature; this phenomenon – Joule heating – and the associated heat conduction in the solid are governed by the heat equation:

$$\rho C_p \frac{\partial T}{\partial t} - k\nabla^2 T = Q = j^2\Omega \tag{5.6}$$

where ρ is the density, C_p is the specific heat, k is the thermal conductivity, and Q is the heat source intensity; the latter is equated to the heat production from Joule heating. The time dependence of the temperature field presents an interesting feature; Eq.(5.6) implies that, in a thermally insulated specimen, even if $\mathbf{j}^\infty$ is held constant, the temperature in the specimen will increase with time and eventually result in melting. Note that this heating will also alter the local deformation and current fields by affecting the yield strength, the electrical resistivity, the heat capacity and thermal conductivity. This requires a coupled analysis that will be examined in Section 5.2. Here the conditions under which the contribution of heat diffusion can be neglected are established. Equation (5.6) is expressed in normalized form as follows:

$$\frac{\partial \hat{T}}{\partial \hat{t}} - \nabla^2 \hat{T} = \hat{Q} \tag{5.7}$$

where $\hat{T} = T/T_M$, $\hat{t} = t/\tau$, $\hat{r} = r/r_{th}$, $\hat{Q} = j^2\Omega\tau/\left(\rho C_p T_M\right)$, $r_{th} = \sqrt{\kappa\tau}$ and $\kappa = k/\left(\rho C_p\right)$. In these expressions, T_M is the melting temperature, κ is the diffusion coefficient, τ is the duration of the current pulse and r_{th} is the diffusion length. For $r >> r_{th}$, diffusion may be neglected. With this in mind, the size of the <u>instantaneous melt zone</u> near the crack tip is estimated. Notice that the rate of temperature change is proportional to $\hat{Q}$. Substituting for j from Eq.(5.7) the temperature field near the crack tip can be written as:

$$T\left(r,\theta,t\right)=\frac{\Omega}{2\pi\rho C_p r}\int_0^t C_i^2 dt \qquad (5.8)$$

If the radius of the melt zone is indicated by r_M, then:

$$r_M(t)=\int_0^t\left(\frac{C_i}{C_{cr}}\right)^2 dt\text{, with } C_{cr}=\sqrt{\frac{2\pi\rho C_p T_M}{\Omega}} \qquad (5.9)$$

C_{cr} is related to the 'action' that is used in evaluating burst threshold for electrical conductors (Tucker and Toth, 1975). Note that equating the heat generated to the heat required at melting in a uniform conductor of cross-sectional area S, results in the following: $\frac{1}{S^2}\int_0^{t_M} I^2 dt=\rho C_p T_M/\Omega$; the right hand side consists of materials properties and is termed action. The factor C_{cr} depends solely on material properties and its value is shown in Table 5.1 for the materials considered in the present work.

Table 5.1. Values of C_{cr} for Al 6061-T6 and Cu-102

Material	C_{cr} - $\frac{A\sqrt{s}}{m^2}$
Al 6061-T6	5.87×10^8
Cu-102	1.30×10^9

In cases where $r_{th} < r_M$, heat conduction in the solid can be ignored[3]. Ignoring heat conduction, a naïve estimate can be made of the melt zone for the case of transient current pulses used in the experiment with the single-edge-notch. From Eqs.(5.8) and (5.9), it is clear that the radius of the melt zone $r_M(t)$ can be written as:

$$\frac{r_M(t)}{a} = \frac{\Omega\left[f_{III}(a/W)\right]^2}{2\rho C_p T_M}\int_0^t \left(j^\infty\right)^2 dt \tag{5.10}$$

The failure criterion is now simply that the crack tip region will melt whenever $r_M(t) \geq r_c$. Note that this is based on the asymptotic analysis of a sharp crack and furthermore neglects changes in physical properties with temperature; in practice, the resistivity of the material increases with increasing temperature and therefore, will alter the current paths near the crack tip. Therefore, the failure criterion should be:

$$r_M(t) \geq \lambda r_c \tag{5.11}$$

with λ determined through a complete numerical analysis, including such resistance changes, or by calibration to experiments. The parameter λ was determined from the experimental measurements to be 0.33 for Al 6061-T6 and accounts for blunt crack and property variation effects. Given a time variation of the uniform current away from the crack – typically this involves using the current measured by the Rogovski coil (shown in Figure 2.7a for example) – Eq.(5.10) may be used to get the variation of the melt zone and to evaluate the critical condition in Eq.(5.11) for the crack. It should be noted that

---

[3] Experiments indicate that the molten metal is ejected by Lorentz forces and therefore may be removed from consideration.

this is an approximate calculation of the melt zone in exactly the same sense in which the elastic field is utilized in the yield condition to determine the plastic zone size.

The experimental measurements can now be interpreted using the local description of the fields near the crack. In particular, the failure thresholds under combined electrical and mechanical loads can be viewed not in terms of absolute quantities $\left(\sigma^c, j_{\max}^{\infty,c}\right)$, but in terms of local quantities that take into account the presence of a crack. Therefore, the critical values of $\left(\sigma^c, j_{\max}^{\infty,c}\right)$ can be used in Eqs.(5.1) and (5.5) to estimate the critical combination of stress and current intensity factors at the onset of melting in the tests; these are denoted as $\left(K_I^c, C_i^c\right)$. This failure envelope is shown in Figure 5.3a and 5.3b for Al 6061-T6 and Cu-102, respectively. In these figures, open symbols correspond to combinations of $\left(K_I, C_i\right)$ where no damage was observed near the crack tip and while filled symbols correspond to tests where crack tip melting was observed. A shaded line is drawn at the boundary between the two responses indicating the failure threshold. Conductors with cracks that fall within the failure envelope can be said to be safe from electrically induced melting or crack extension (for this current pulse profile). The failure threshold for Cu 102 suggests a coupling between the mechanical and electrical fields, while for the Al 6061-T6, the influence of mechanical loading appears to be weak. While the critical condition is given in terms of the current intensity factor in Figure 5.3, this diagram misses an important point: the accumulation of heat with time. The best way to understand the failure is to use Eq.(5.10) to estimate the radius of the melt zone as a function of time and determine when this exceeds the crack tip or notch radius, as indicated in Eq.(5.11).

5.2. Numerical Simulation

In order to analyze the interaction between the mechanical, thermal and electrical fields, a finite element model was constructed in the multi-physics simulation software, COMSOL. Due to the complexity of this analysis, the model is built in stages, incorporating additional physics at each stage. Therefore, in the present work the problem of melting is considered and the corresponding electrical and thermal problems are solved to find the melt zone radius as a function of time; here the effect of crack tip bluntness as well as the influence of heat conduction are incorporated. The mechanical loading is not considered in the present work. The main aim of the modeling effort is to make plausible the physical assumptions that have been used to interpret the observed melting and ejection. The material properties used in all the simulations can be found in Table 2.1 for the Al 6061-T6.

The domain to be modeled in the numerical simulation is shown in Figure 5.2; although symmetry boundary conditions could be introduced we discretized the entire domain. The analysis is restricted to two dimensional elements since we consider thin sheet specimens; however in thick specimens, as indicated in Section 5.3, melting initiates at the interior and spreads towards the free surfaces quickly. A refined triangular mesh is used in the vicinity of the crack; the crack itself is modeled either as a rounded tip with a radius of 200 μm or as a ‘sharp’ crack with a radius of 20 nm. Comparison of the two results will be used to establish the validity of the asymptotic analysis. The electrical field is governed by Eq.(5.3) together with the boundary conditions indicated in Figure 5.2. Specifically a uniform current flow was imposed at $x_2 = \pm h$. The time variation of the current is expressed as a simple sine wave given in Eq.(2.1). The thermal field is governed by Eq.(5.6), with the heat source given by Joule heating and appropriate insulating boundary conditions along the sides and crack faces. The coupled electrical-thermal problem is solved in a staggered manner. At each time step, the electric field is calculated first; at this time step the Joule heating from the calculated current is then introduced into the thermal problem where time integration is performed explicitly. The simulation marches in this way through the imposed current sinusoidal pulse.

First, the effect of crack tip bluntness is explored. Figures 5.4 and 5.5 show a comparison of the fields calculated using a blunt crack (with crack tip radius of 200 μm) and a sharp crack (with a crack tip radius of 20 nm). The color contours indicate the temperature field while the arrows indicate the current density vector. Figure 5.6 shows a comparison of $j_2(r,0)/j_{\max}^{\infty}$ evaluated at the peak of the current cycle calculated from the asymptotic result in Eq.(5.4) with the numerical simulations corresponding to the blunt and sharp cracks. It is clear that the calculated current variation corresponds very closely to the singular field. Second, the temperature contours are nearly circular in shape, confirming the usefulness of the asymptotic calculation in Eq. (5.10). A quantitative estimate of the radius of the melting zone (defined in the simulation as the position at which the temperature equals T_M) as a function of time for the sinusoidal current pulse is shown in Figure 5.7. In this figure, the simulation results for the sharp and blunt cracks are shown; in addition the asymptotic calculation using Eq.(5.10) is also shown.

It is clear that the asymptotic results do quite well in matching the calculations based on heat conduction and blunting. This has two implications; first, the sharp crack will become blunted as melting progresses and beyond this point the two become nearly indistinguishable and thus the effect of crack tip bluntness is appreciable only in the early stages of crack growth. Second, for the timescale considered, the effect of heat conduction is not significant since neither the current variation and nor the melt zone radius appear to be influenced significantly by heat conduction.

However, these simulations have the unrealistic feature that with continued current passage the radius of the melt zone grows, with the melt region remaining circular; this is contrary to the experimental observations and arises from the neglect of two essential features of the experiment. First, the resistivity of the material is a function of temperature; this results in the crack tip region becoming more resistive with time and hence diverting the current away from the tip; second, the molten material is unable to sustain loads and as a result is ejected from the crack tip region by the Lorentz forces. These effects are introduced in the simulation by adopting the following strategy. First, the resistivity is prescribed as a linear function of temperature: for Al 6061-T6, $\Omega = \Omega_0 \left[1 + \beta \left(T - T_0 \right) \right]$, with values of Ω_0 and β obtained by fitting to the resistivity values in Simmons and Baluffi, (1959). Second, in order to ensure that the molten region did not contribute further either to the electrical or to the heat conduction problem, the resistivity and the specific heat were increased to a large value as the temperature reached

T_M. Results of this simulation for Al 6061-T6 are illustrated in Figure 5.8; in this figure, the color contours indicate the temperature while the lines indicate the electric potential ϕ. Figures 5.8a to 5.8d indicate the results of the simulation at times corresponding to the first four peaks of a sinusoidal current pulse similar to the one shown inf Figure 2.7a, with $j_{\max}^{\infty} = 4.7 \times 10^9$ A/m^2. The development of the melt zone and the diversion of the current around the melt zone are observed in the simulation; also, the melt zone extends with each subsequent cycle along the line of the crack. The corresponding experimental observations are shown to the right in Figures 5.8e to 5.8h. The time variation of the melt-zone radius is shown in Figure 5.9; the solid lines indicate the results of the COMSOL simulation, while the symbols represent the experimental measurements. The correspondence between the two indicates excellent qualitative agreement and a reasonable quantitative agreement. Note that the removal of the molten material and the physical interaction that couples the electrical and mechanical effects have not been modeled completely; there are two possible contributions, one resulting from the thinning of the crack tip region and resulting three dimensionality, and the other from the Lorentz forces generated by the electromagnetic interactions

5.3. Three dimensional effects

All the experiments reported in the previous section were performed on thin specimens (0.8 mm); in these cases, nearly uniform mechanical and electrical fields through the thickness direction could be assumed. However, if the thickness becomes large, relative to intrinsic length scales, potentially three-dimensional effects on the problem have to be considered. The intrinsic length scale for determination of three-dimensionality is provided by the development of the plastic zone near the crack tip for the mechanical problem. For the electrical problem, the length scale is set by the depth of penetration of the electrical field (skin depth); this is dependent on the frequency of the electric field and was estimated in Section 3 to be on the order of one mm. So, it is of interest to determine how cracks respond when the specimen thickness is varied significantly in relation to these intrinsic lengths.

In order to examine the response of relatively thick specimens, single edge notch (SEN) specimens with nominal cross-sectional dimensions of 12.7 mm (1/2 in) by 6.36 mm (1/4 in) were used. Those rods were cut to be 381 mm (15 in) long and a sharp notch was cut with a wire-EDM. A schematic diagram of the region near the crack tip is shown in Figure 5.10. This specific design, with a large opening notch, was chosen to allow a clear view of the center portion of the notch; this was necessary to observe any three dimensional aspects of the response properly. Two orientations of the cross-section were considered in order to vary the thickness. The depth of the cut was varied for both geometries from 40% to 60% of the width; this choice of deep cracks was necessary due to the limitations of the power supply.

For the large cross-sections used in these specimens, the power supply has to provide a much larger current in order to maintain the current densities at levels comparable to that used for the thinner specimens. The pulsed power supply available at the Institute for Advanced Technology at The University of Texas was used for this purpose. This system has a much larger total energy storage in the capacitor bank and is capable of providing current densities of the order of ~1.5 GA/m^2. This power supply is a heavily overdamped system, and therefore, the current output does not display the ringing behavior observed in the tests reported in the previous chapter. A typical overdamped shape for the current pulse from this facility is shown in Figure 5.11a, The total amount of energy deposited into the specimen is about 0.8 J for aluminum and 0.4 J for copper and results in a temperature increase of 32 °C for the aluminum and 10 °C for the copper specimens in the region away from the crack. The power spectrum of this pulse is shown in Figure 5.11b; for the highest frequencies contained in this pulse (~900 Hz for the 16th Fourier mode), the skin depth is estimated to be 4.5 mm for the aluminum alloy and 3 mm for the copper. Therefore, one expects nearly uniform current distribution with some concentration around the crack tip and corners.

The current levels used in these large specimens are quite high; therefore, special connectors had to be designed for introducing the current into the specimen. Furthermore, the Lorentz forces are significantly larger than in our previous experiments. Therefore, a special supporting rig was designed for the large scale specimens; the geometry of this fixture is shown in Figure 5.12. The current is supplied to the specimen through a set of custom built clamps which hold the specimen in place. In an attempt to minimize the Lorentz forces, a symmetric design with two rods that run alongside the specimen is used in completing the circuit. The distance between the conductors was selected so as to leverage on the 1/r decay of the magnetic field from the conductor. In this arrangement, the Lorentz interactions between the two return paths cancel each other in the plane of the conductors. The only drawback of this arrangement lies in the stability with respect of the out-of-plane motion of the specimen; any out-of-plane misalignment would cause a bending moment on the specimen and continue to bend the specimen. The stability of the system will depend on the bending stiffness of the specimen itself, on the intensity of the field and on the distance between the rods. Due to the presence of the notch in the center of the specimen, its bending stiffness is significantly reduced; therefore, to avoid this bending instability, a backing support consisting of a G10 rod with the same cross-section as the specimen was clamped to the specimen and resulted in a stiffness increment sufficient to minimize out-of-plane bending. Multiple runs were made with increasing currents until melting was noticed near the crack tip.

The procedure followed in these tests is similar to that used in Section 3, with the exception that a mechanical load was not applied; this was due to the difficulty in insulating the loading system for high currents. This omission should not be a major impediment because, as observed in Section 5.2, melting and not mechanical failure was the most important factor in determining failure of the conductors. In order to view and capture the entire crack length along with the surface, the high-speed video camera was oriented at 45 degrees with respect of the front face of the specimen; this provides a three-dimensional perspective view of the crack front. Experiments were performed on Al 6061-T6 and Cu 102. To generate crack tip melting without exceeding the limit of the bank of capacitors, the notch length was increased from 40% to 50% for the thinner side of the aluminum bar and to 60% for the thicker one. For the copper the crack was extended to 70% of the width. The peak current was increased in each test from 1.2×10^9 A/m^2 to 2.8×10^9 A/m^2 in finite intervals until some visible damage appears.

First, Al 6061-T6 bars were tested with the notch on the ¼ in side; for pulses of peak current below 1.5×10^9 A/m^2 no visible damage occurred. A selected sequence of images from the high speed video of a test with a peak current of 1.9×10^9 A/m^2 is shown in Figure 5.13; a very small plume of smoke appeared on the surface of the specimen near the tip of the crack (Figure 5.13b) and a small molten region could be observed near the center of the specimen (Figure 5.13c). The specimen was then removed from the fixture and examined at high magnification in an optical microscope; the near tip region is shown in Figure 5.14 and displays some damage; it is not clear whether this can be characterized as melting. The experiment was then repeated at a peak current of 2.1×10^9 A/m^2; this time, the appearance of molten material at the center of the crack was observed in the high speed video images shown in Figure 5.15. At about 500 μs, the bright spots seen in the figure both near the center of the crack and on the surface of the specimen indicate molten material; beyond this point, the material melts and is ejected out. A video of this melting phenomenon is attached to this dissertation.

Melting and ejection stop as soon as the current decays to zero after about 6 ms. Optical micrographs of the front and back sides of this specimen are shown in Figure 5.16. The appearance of a circular hole near the crack tip is evident; this is quite similar to the observation of the melt cavity in the small scale specimens reported in Figure 5.1. In order to identify the melting threshold, the first appearance of the visible damage anywhere along the crack front was used as the critical condition. As discussed in Section 5.1, melting starts when the radius of the melt zone is larger than some fraction of the crack tip radius: $r_M(t) \geq \lambda r_c$. Therefore the values of λ were extracted from the measurements of melting threshold in these large samples. The resulting values for r_M are reported in Table 5.2; these values are consistent with the threshold found previously in Section 5.1 for the thin specimens, validating the criterion for melting suggested in Eq.(5.11).

5.4. Crack Tip Melting in Aluminum Alloys

In order to determine the melting threshold in other aluminum alloys, tests described in Section 5.1 were performed on Al 1100-0, 1100-H14, 2024-T3 and 7075-T6. Each alloy was subjected to current pulses at various levels of load in order to find the failure envelope, and each threshold was evaluated using Eq.(5.5). Each specimen was pulsed

Table 5.2. Action calculation and comparison for different thicknesses

		1/32 in Width	¼ in Width	½ in Width	
Thickness	b	8.13E-04	6.35E-03	1.27E-02	m
Width	w	1.00E-02	1.27E-02	6.35E-03	m
Crack Tip Radius	r_c	2.16E-04	2.16E-04	2.16E-04	m
Crack Length	a	4.20E-03	6.57E-03	4.03E-03	m
Geometry Factor	f_{III}	1.08E+00	1.14E+00	1.24E+00	
	r_M /a	1.73E-02	1.13E-02	1.84E-02	
	r_M	7.25E-05	7.44E-05	7.42E-05	mm
	λ	0.336	0.345	0.344	

with increasing energy while no mechanical load was applied and the threshold of melting was identified; these results are shown in Figure 5.17 for all five aluminum alloys. As before, the open black circles indicate current levels at which no melting was observed, while the filled red circles signify pulse conditions for which some ejection was recorded. Looking at the graph, the first aspect to notice is that the failure threshold varies greatly between the different alloys; this was to be expected due to the large range of electrical and thermal properties of the material selected. At this stage, the failure threshold in Eq.(5.10) was introduced and the values of the molten radius were computed; the values found are shown in Table 5.3 along with the values for aluminum 6061-T6 and Cu-102.

As discussed in Section 5.1, melting starts when the radius of the melt zone is larger than some fraction of the crack tip radius: $r_M(t) \geq \lambda r_c$. Therefore the values of λ were extracted from the measurements of melting threshold; comparing this parameter for each alloy it became clear that it is somewhat consistent for the aluminum specimens but it varies drastically for copper. This result was expected due to the different physical properties of those alloys; in fact, recalling that the factor λ depended on the change of resistivity near the molten zone and on the heat conduction, its magnitude was scaled by the heat transfer coefficient for each material normalized by the same coefficient of the Al 6061-T6.

After comparing the threshold of each material at zero load, a series of tests were carried out at different mechanical load levels in order to inspect their behavior under combined electro-mechanical loading. The plot for the melting threshold of al 1100-O is

Table 5.3. Action calculation and comparison for different materials*

	Al 1100-O	Al 1100-H14	Al 6061-T6	Al 7075-T6	Al 2024-T3	Cu-102	
Ω	2.99E-08	3.00E-08	3.99E-08	5.15E-08	5.82E-08	1.70E-08	ohm-m
ρ	2.71E+03	2.71E+03	2.85E+03	2.81E+03	2.78E+03	8.90E+03	kg/m^3
C_p	904	904	899.56	960	875	385	J/(KgK)
k	222	220	167	130	121	385	W/m-K
T_m	916	916	855	750	775	1356	K
r_M /a	1.51E-02	1.60E-02	1.72E-02	2.58E-02	2.41E-02	8.39E-03	
r_M	6.35E-05	6.71E-05	7.21E-05	1.08E-04	1.01E-04	3.52E-05	mm
λ	3.40	3.22	2.99	1.99	2.14	6.13	
$\lambda(k_{Al}/k)$	0.29	0.31	0.33	0.5	0.47	0.16	mm

*Geometrical properties same as for to Table 2.1

shown in Figure 5.18, while the threshold for other aluminum alloys are shown Figures 5.19 – 5.21. From these tests it became clear that the threshold for melting does not depend strongly on the load applied. In fact even for the Al 1100-O – which displayed the largest influence of the load in the threshold – the current level required for melting at 60% mechanical load diminishes only of about 10%. Other alloys instead display very little interaction between the two quantities.

.

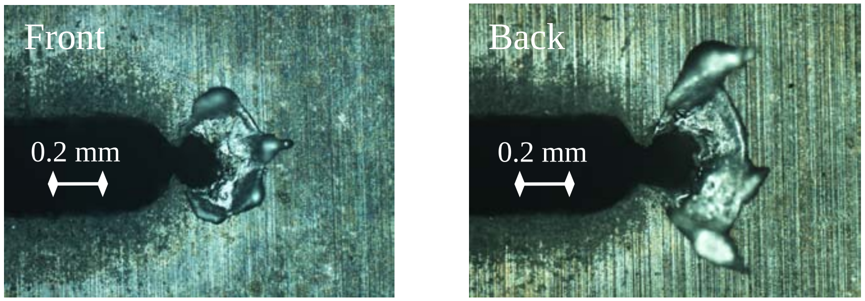

Figure 5.1. Close up view of the melting induced in the crack tip region. The initial crack has a blunt tip; the first current pulse melts a circular region near the crack and ejects this material out, creating the appearance of a hole. Front and back views of the specimen are shown. For this experiment $j_{\max}^{\infty} = 4.1\times10^{9}$ A/m^2; a = 4.2 mm, $\sigma^{\infty} = 0$

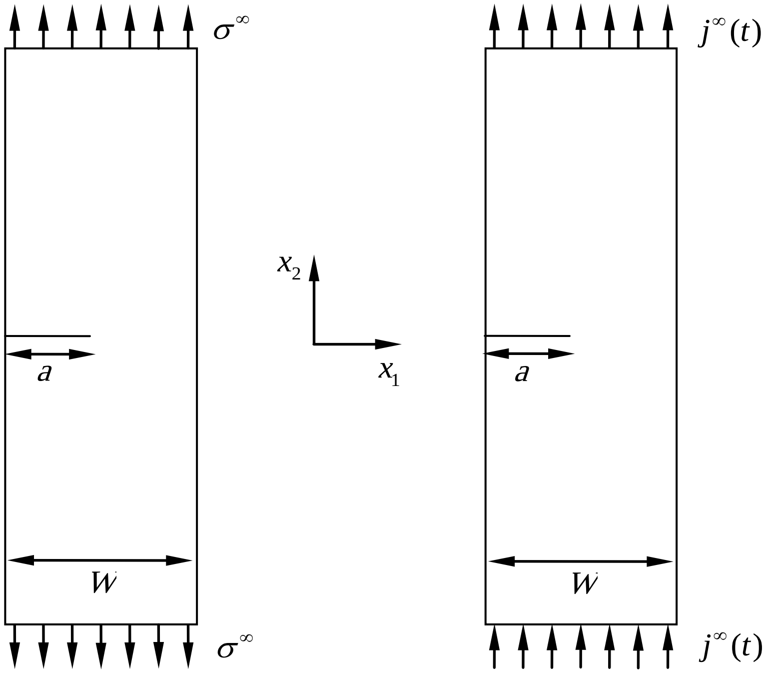

Figure 5.2. Schematic diagram of the single-edge-notched specimen. Diagram on the left illustrates the mechanical boundary value problem while the one on the right illustrates the electrical boundary value problem.

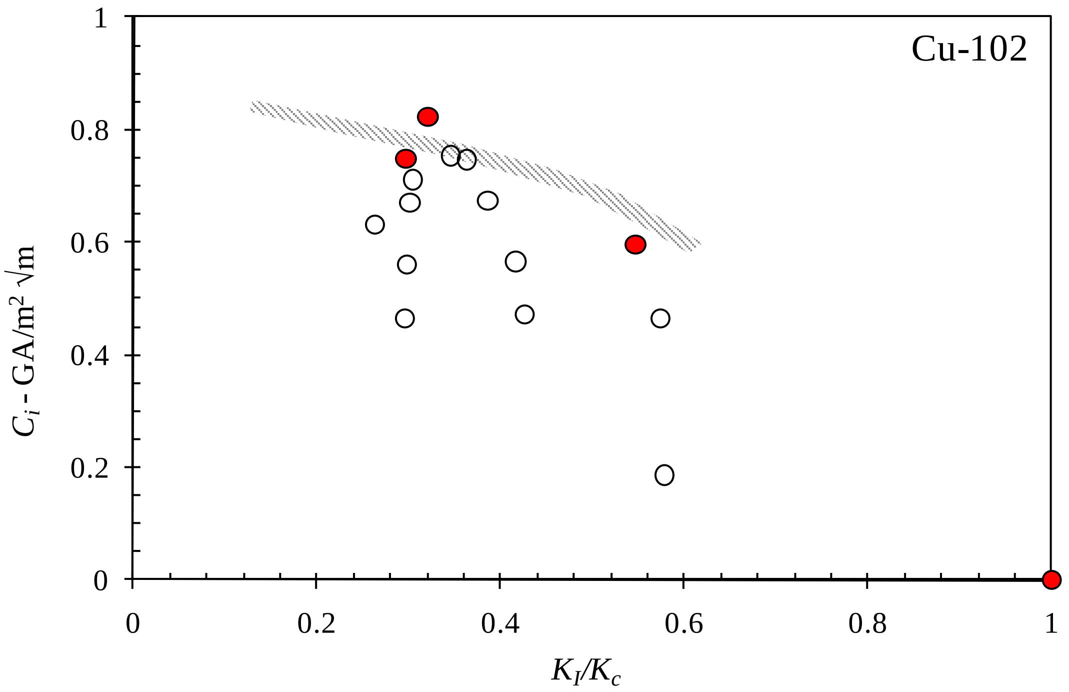

Figure 5.3a. Interaction diagram of the critical current intensity factor and the mechanical stress intensity factor at the threshold of melting.

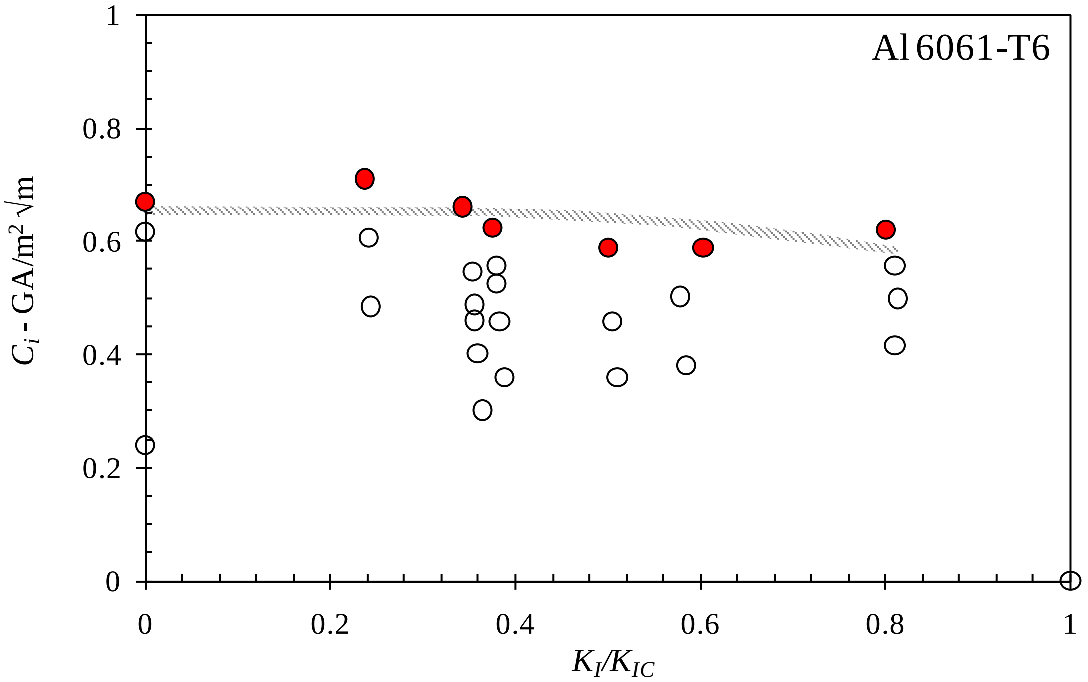

Figure 5.3b. Interaction diagram of the critical current intensity factor and the mechanical stress intensity factor at the threshold of melting.

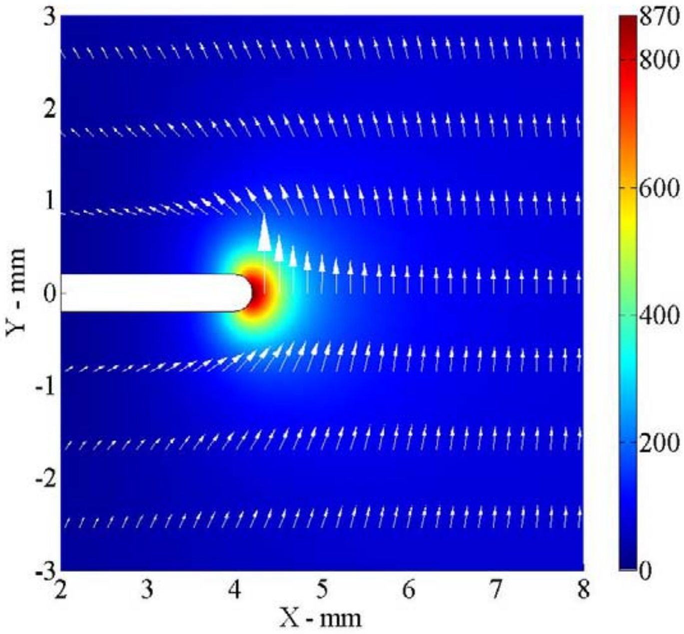

Figure 5.4. Results of the simulation with $j^{\infty} = 4.7 \times 10^{9}$ A/m^2 and crack tip radius of 200 μm. Arrows indicate current vector and contours indicate temperature in Celsius.

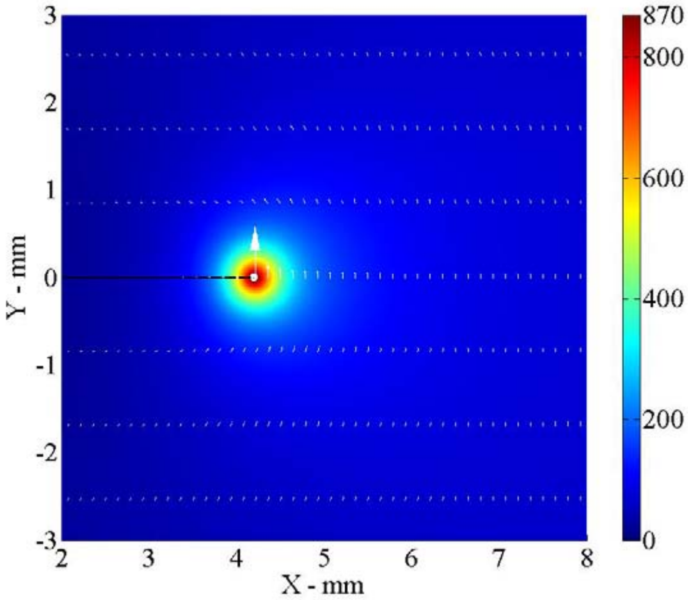

Figure 5.5. Results of the simulation with $j^{\infty} = 4.7\times10^{9}$ A/m^2 and crack tip radius of 20 nm. Arrows indicate current vector and contours indicate temperature in Celsius.

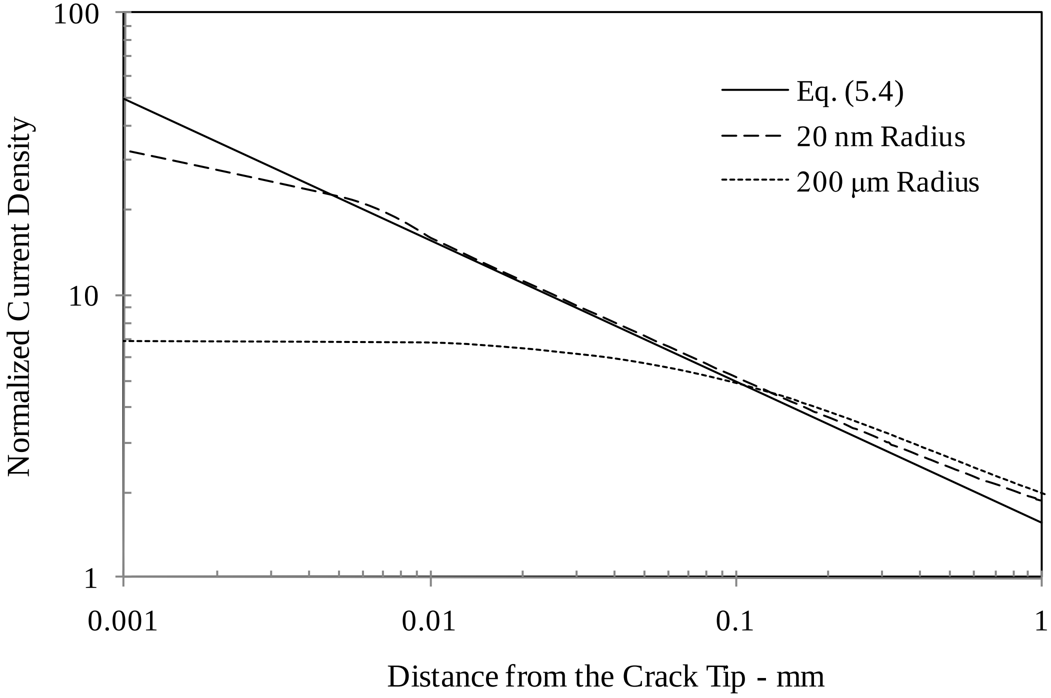

Figure 5.6. Comparison of current density vs. distance from asymptotic analysis and numerical simulations.

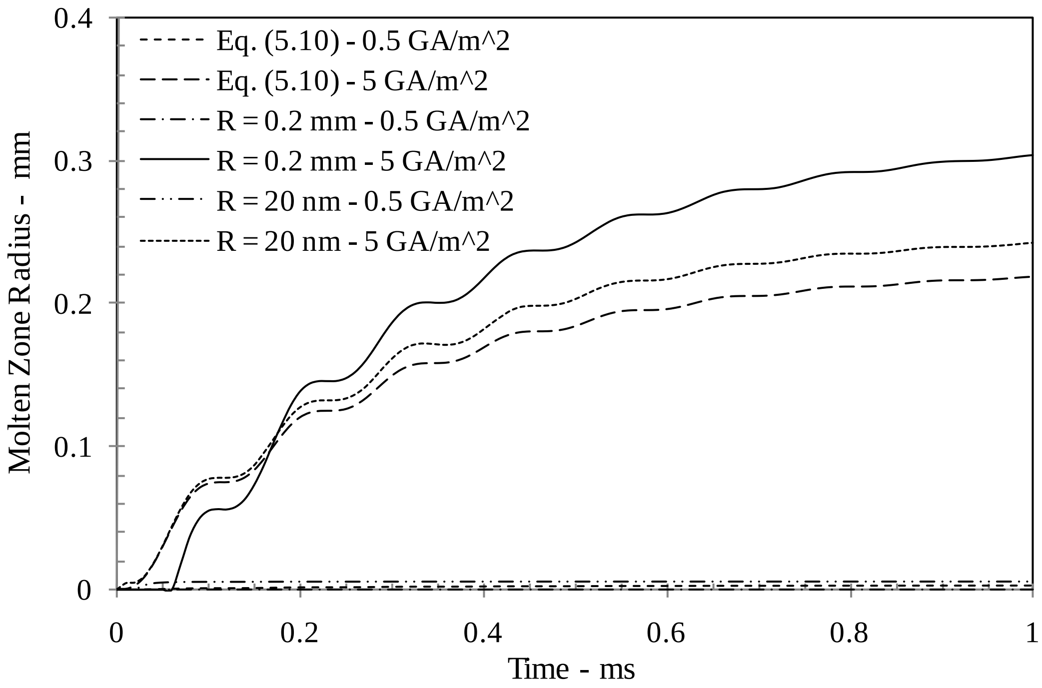

Figure 5.7. Comparison of the time variation of the molten zone radius from asymptotic analysis and numerical simulations.

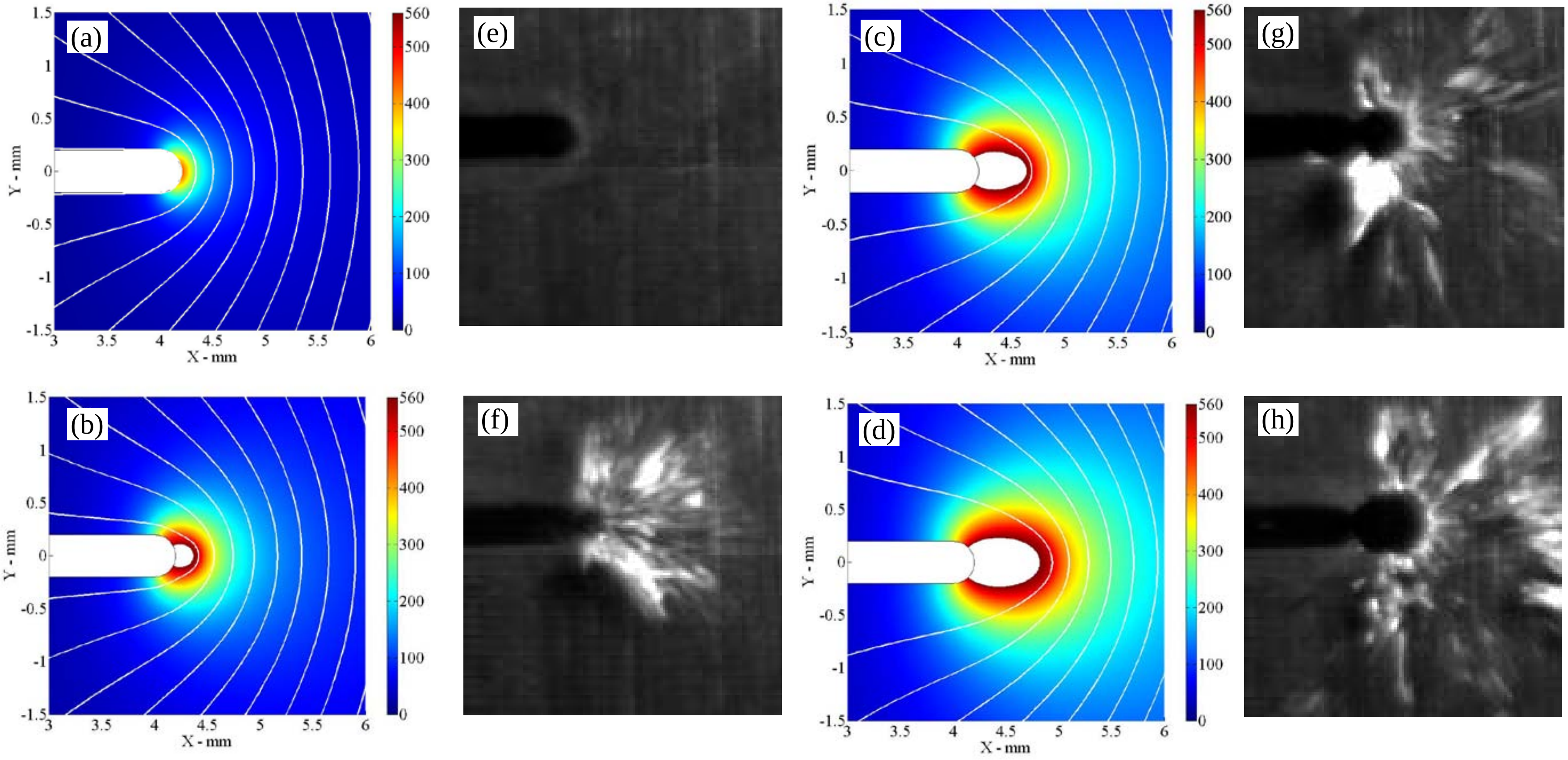

Figure 5.8. Comparison of the progression of crack tip melting as a function of time. Color contours indicate temperature in Celsius; temperatures above the melting point of the aluminum alloy have been rendered white. The material, however, has not been removed in the simulation. Lines indicate contours of constant electric potential.

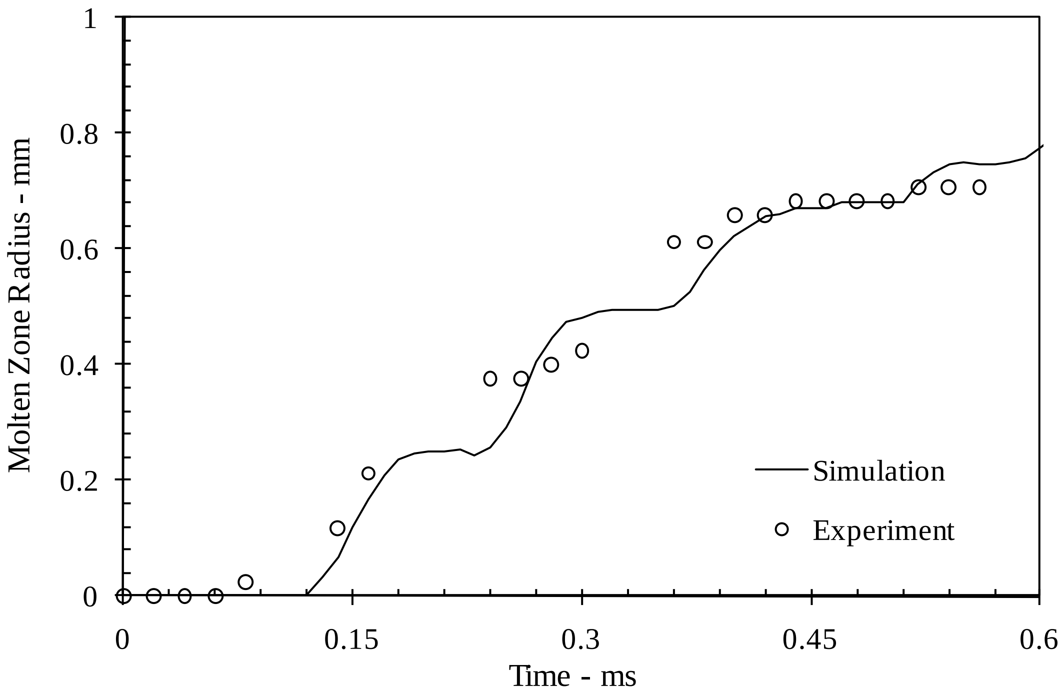

Figure 5.9. Comparison of the time variation of the measured molten zone radius with the numerical simulation.

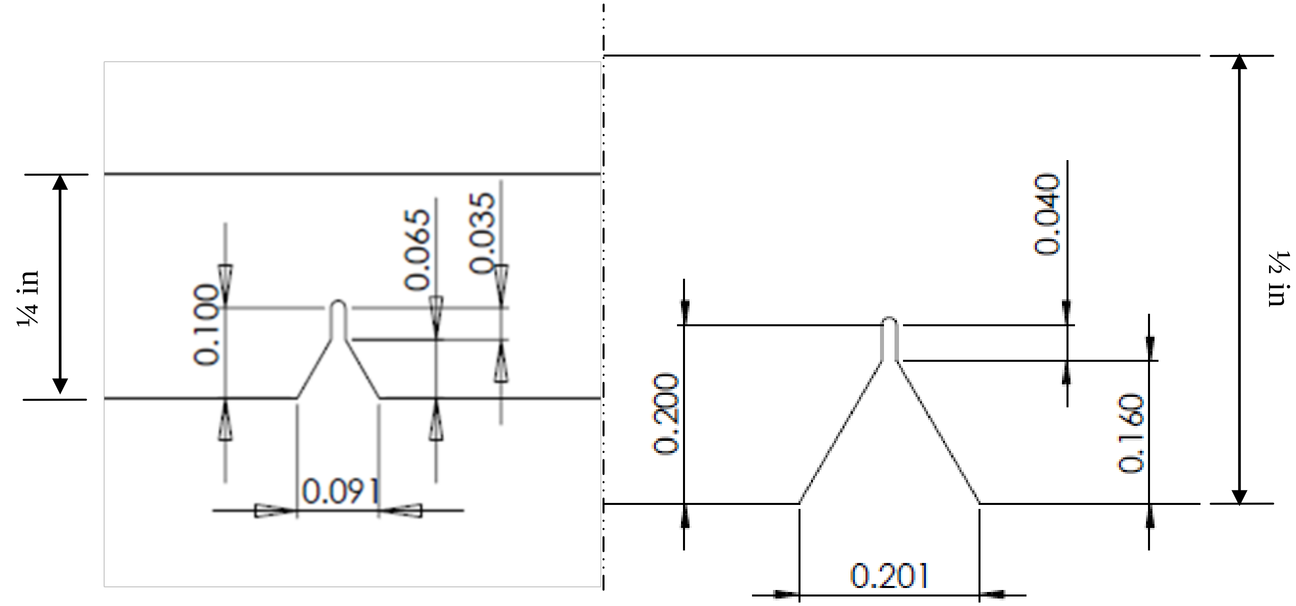

Figure 5.10. Single Edge Notch profiles for the quarter inch side (left) and half inch side (right). The total dept was varied from 40% to 60% of the total thickness for each configuration.

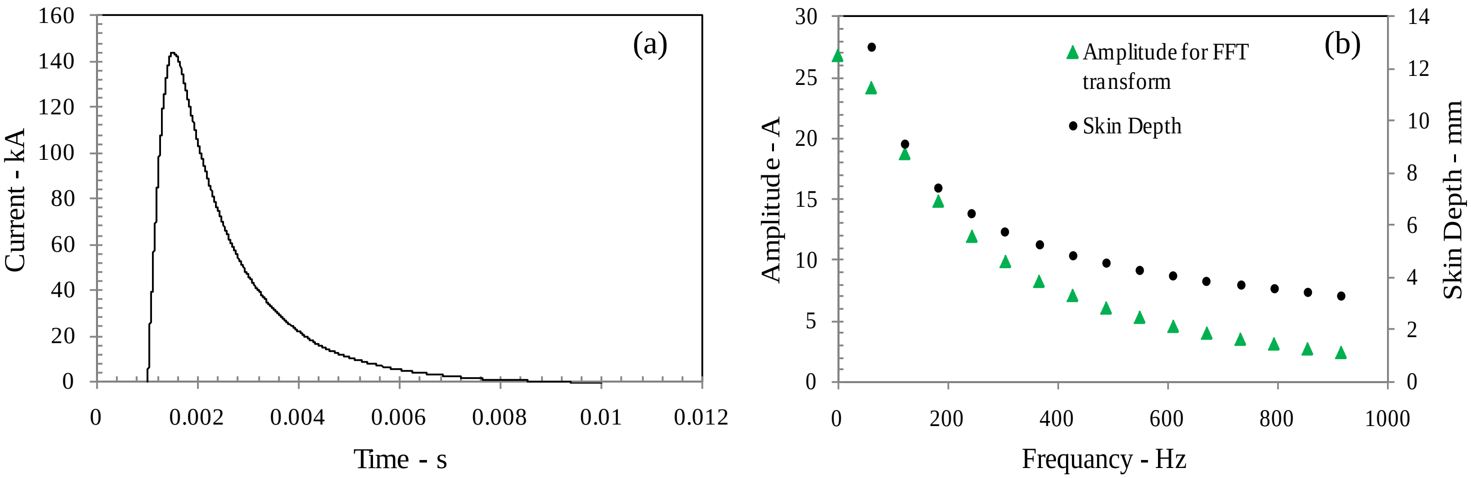

Figure 5.11. The original pulse provided by the new power supply is shown on the left while the amplitude spectrum (green triangle) along with the skin depths (black dots) for the first 16 frequencies is plotted on the right.

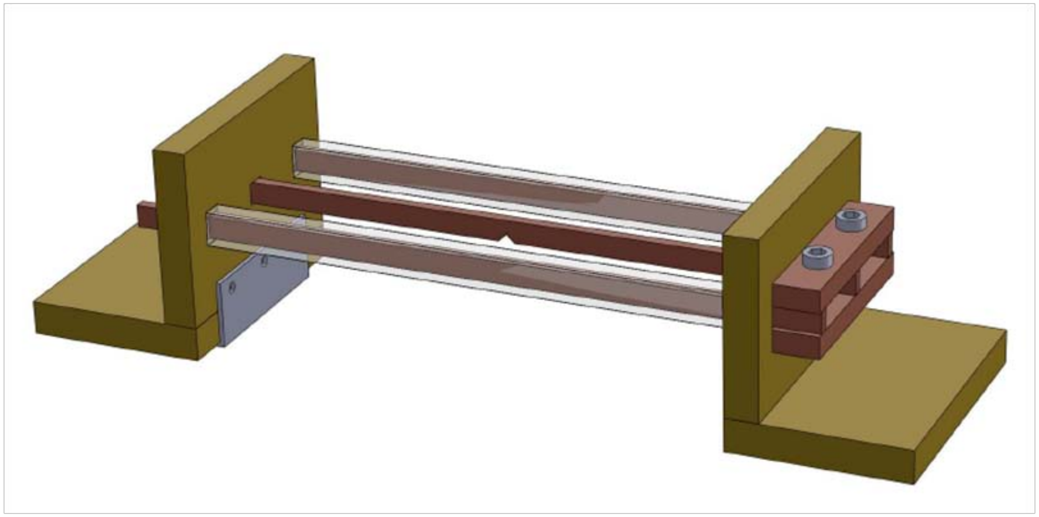

Figure 5.12. Rig designed to test the wider specimens. The specimen is placed at the center and the two side rails close the circuit. The current is fed at the left hand side of the system

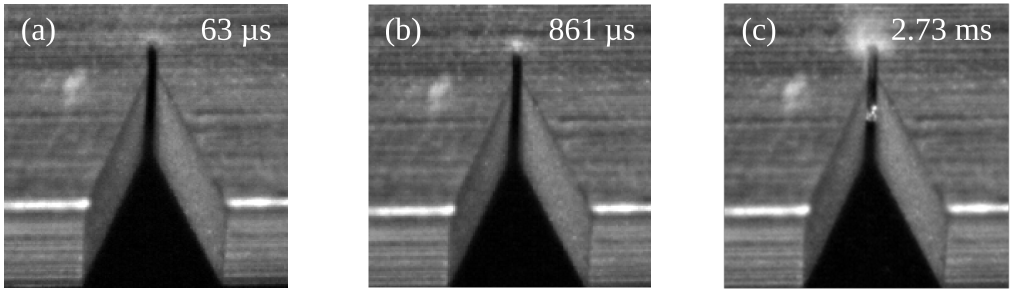

Figure 5.13. Selected images of the crack tip region indicating melting. For this experiment $j_{\max}^{\infty} = 1.9\times10^{9}$ A/m^2; a = 6.3 mm, $\sigma^{\infty} = 0$

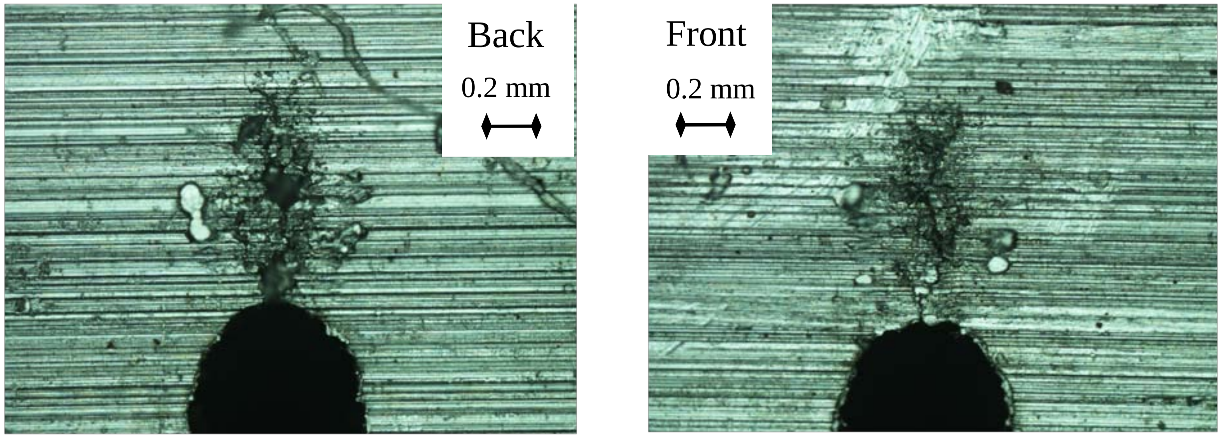

Figure 5.14. Close up view of the melting induced in the crack tip region. The initial crack has a blunt tip. The current pulse melts a small region near the center of the crack; some localized ejection is also observed on the surfaces near the crack tip. This damage however is limited to a depth of 5 microns. Front and back views of the specimen are shown. For this experiment $j_{\max}^{\infty} = 1.9$ 10^9 A/m^2; a = 6.3 mm, $\sigma^{\infty} = 0$

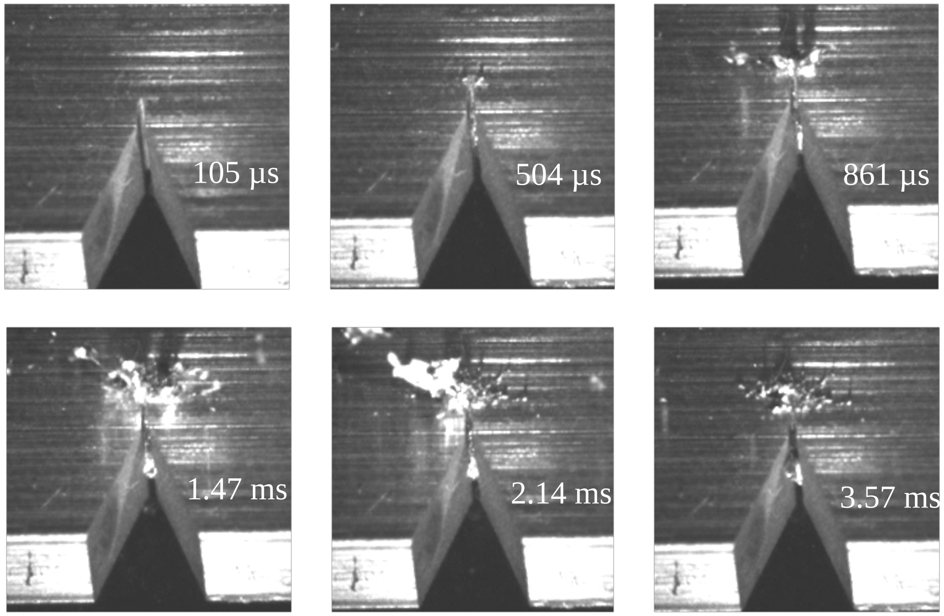

Figure 5.15. Selected images of the crack tip region indicating melting. For this experiment $j_{\max}^{\infty} = 2.1\times10^{9}$ A/m^2; a = 6.3 mm, $\sigma^{\infty} = 0$

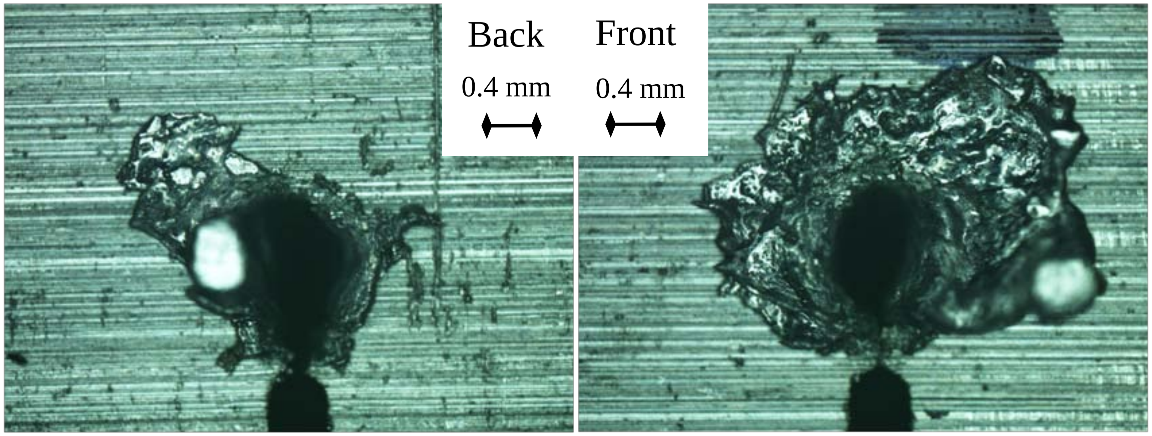

Figure 5.16. Close up view of the melting induced in the crack tip region. The initial crack has a blunt tip. Front and back views of the specimen are shown. For this experiment $j_{\max}^{\infty} = 1.9 \times 10^{9}$ A/m^2; a = 6.3 mm, $\sigma^{\infty} = 0$

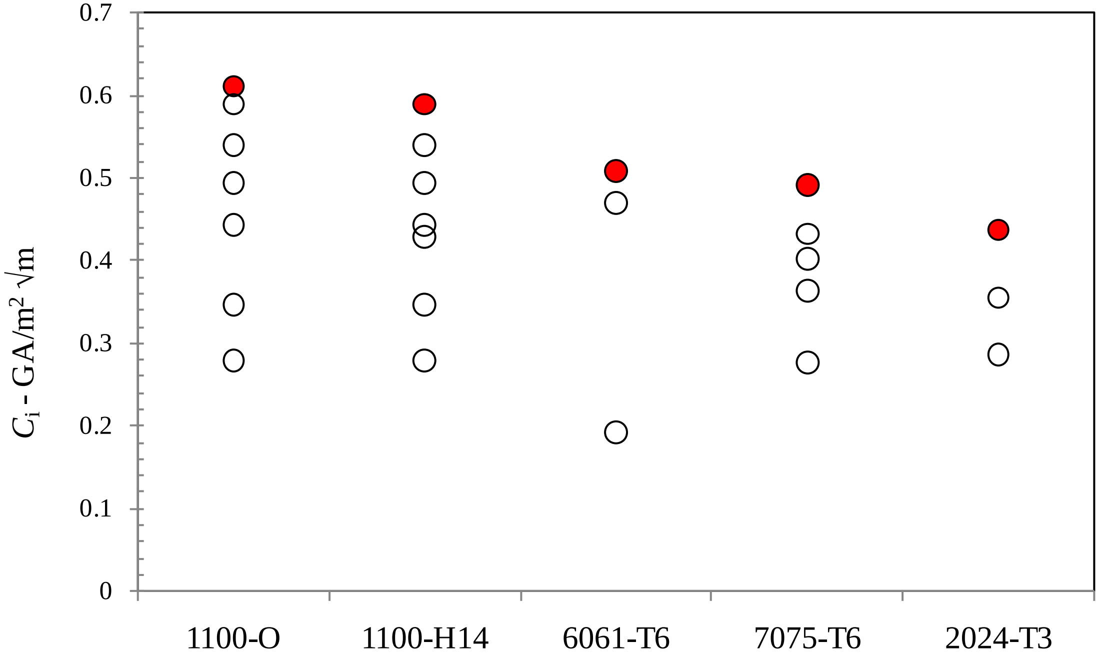

Figure 5.17. Melting threshold for different aluminum alloys. Open circles correspond to pulses at which no melting or ejection was observed. Red filled circles indicate current values at which ejection is first recorded.

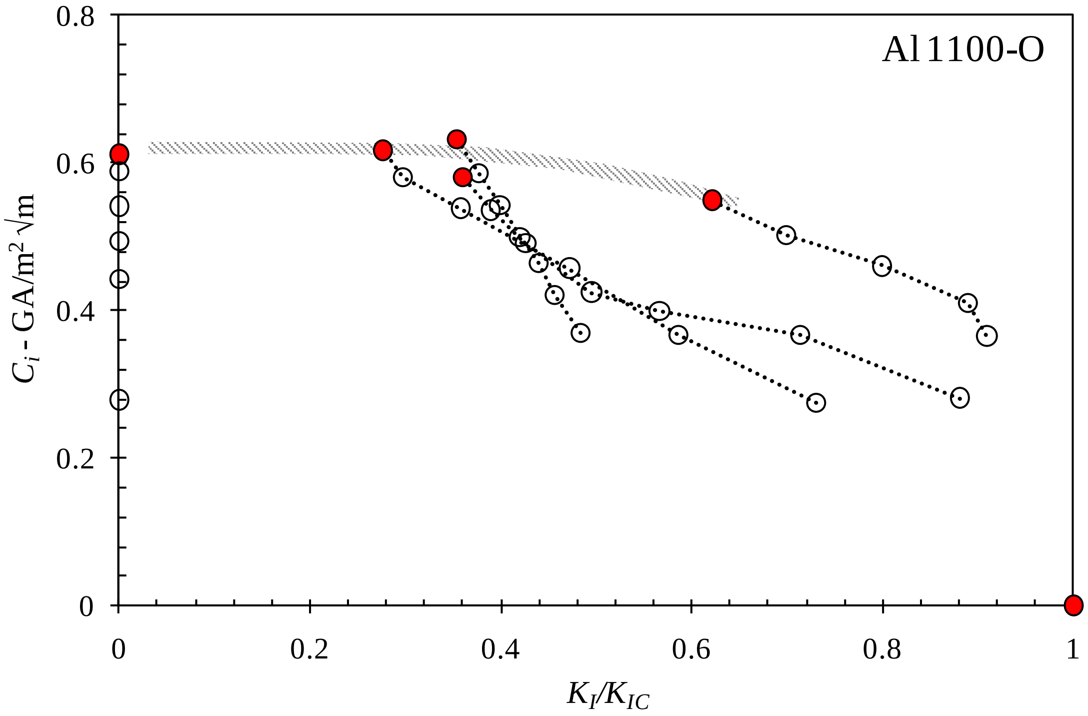

Figure 5.18. Interaction diagram of the critical current intensity factor and the mechanical stress intensity factor at the threshold of melting.

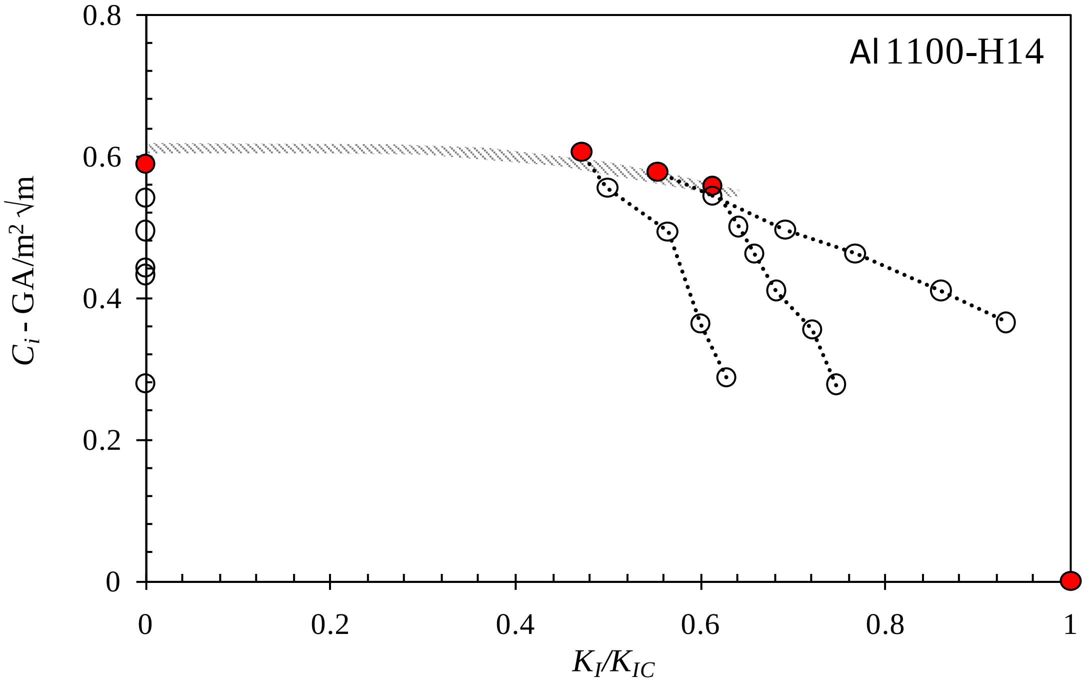

Figure 5.19. Interaction diagram of the critical current intensity factor and the mechanical stress intensity factor at the threshold of melting.

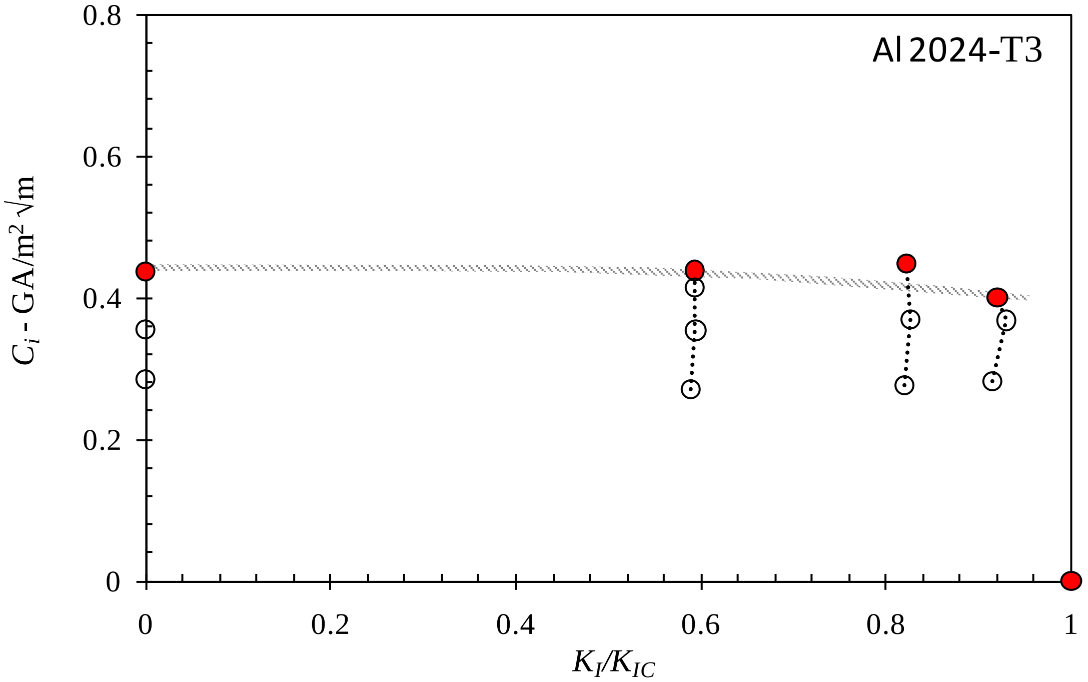

Figure 5.20. Interaction diagram of the critical current intensity factor and the mechanical stress intensity factor at the threshold of melting.

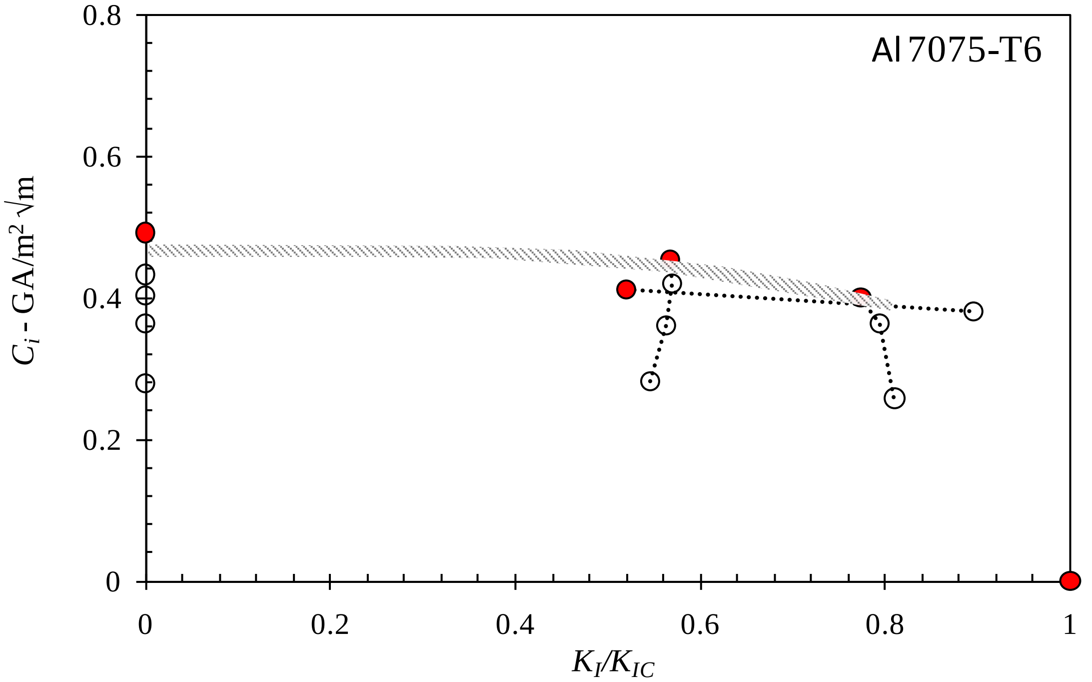

Figure 5.21. Interaction diagram of the critical current intensity factor and the mechanical stress intensity factor at the threshold of melting.

6. CONCLUSIONS

Two materials – Al 6061-T6 and Cu-102 – have been tested with a combination of electrical pulses and mechanical loads to establish the response to those conditions. The temperature rise provoked by the current pulse in the uniform portion of the material was calculated for each test. It was found that for a certain combination of loads and maximum temperatures reached, some plastic accumulation may occur. While specimens were tested in both fixed grip and dead load conditions, each test unveiled a different characteristic of the response. For fixed grips conditions, the plastic accumulation happens almost simultaneously with the increase in temperature due to the quick response of the system to those conditions. The total plastic strain accumulated for this test is limited to less than one percent due to the boundary conditions limiting the overload experienced by the specimen. For dead-load conditions, instead, the accumulation can be much larger thanks to the ability of the specimen to expand freely; however, this accumulation seems to happen at later times. Both the tests were strongly influenced by the dynamic effect associated with the loading apparatus, which drives the maximum load experienced by the specimen. Once the dynamic effects are taken into account, it is shown that a viscoplastic model can be applied to predict the total plastic strain accumulation. The viscoplastic model captures very well the expected plastic strain accumulation without the need of incorporating electroplasticity. Therefore, for temperatures below 0.5 T_M viscoplasticity seems to be the primary contributor to plastic strain accumulation.

The effect of a defects (such as cracks) on a current carrying conductor was successfully observed. This effect was characterized by material melting and ejection from the tip of the crack. A complete multiphysics model was studied to establish the condition at which such damage would occur. This study concluded that necessary condition for material melting and ejection is for the molten zone radius to exceed a certain value. This limiting value was found to be related to the radius of curvature of the crack tip through a factor λ. The threshold condition is summarized in Eq. (5.11) and is a function of the material properties and of the current pulse history.

The factor λ was found to be consistent for different specimen geometries and current pulse histories, but it varied depending on the material being tested. Therefore, it was established that λ depends on material properties. More specifically, if normalized by the heat conduction coefficient for each material, it was found to be consistent across the material range. Tests performed at different mechanical loading conditions establish that the dependence of this threshold on the mechanical loading is very weak and is limited to a region close to the critical stress intensity factor. This dependence was found to be more pronounced for materials with high hardening and larger plastic deformations around the crack tip, such as annealed aluminum. Furthermore, tests performed on wider specimens confirmed the presence of some three-dimensional effects, especially due to skin depth effect. However, the general characteristics of the response seem to be consistent across the range of widths.

Some aspects of plastic strain accumulation associated with heating to temperatures well above 0.5 T_M have not been resolved in the present work. In particular, aspects of “flash-annealing” or “flash-aging” under short duration heat pulses present an interesting method of altering mechanical properties of aluminum alloys and should be explored more completely. The dead-weight experiments present an opportunity for viscoplastic or creep characterization of materials through extremely short duration experiments and should be explored in order to generate efficient material characterization protocols for creep.

Appendices

APPENDIX I: SPECIMEN DIMENSIONS

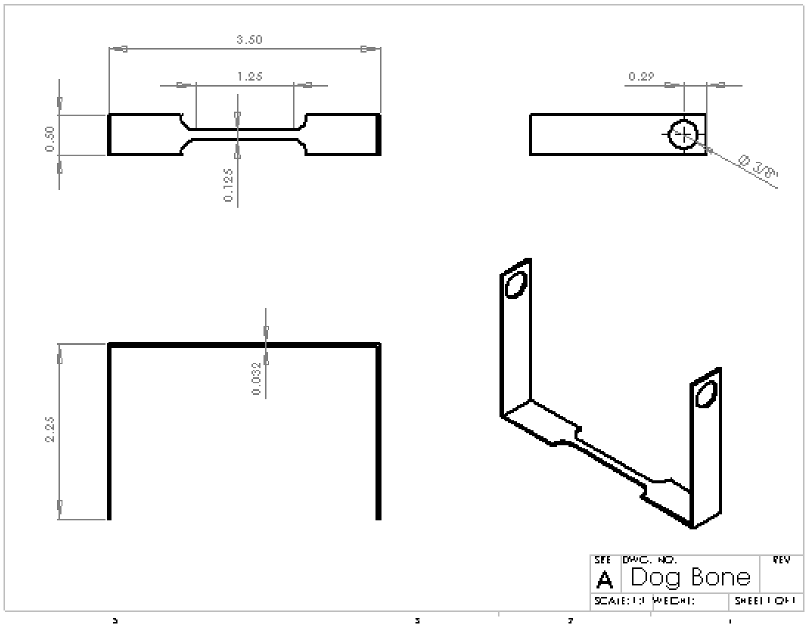

APPENDIX II: STRESS STRAIN AT CONSTANT TEMPERATURE

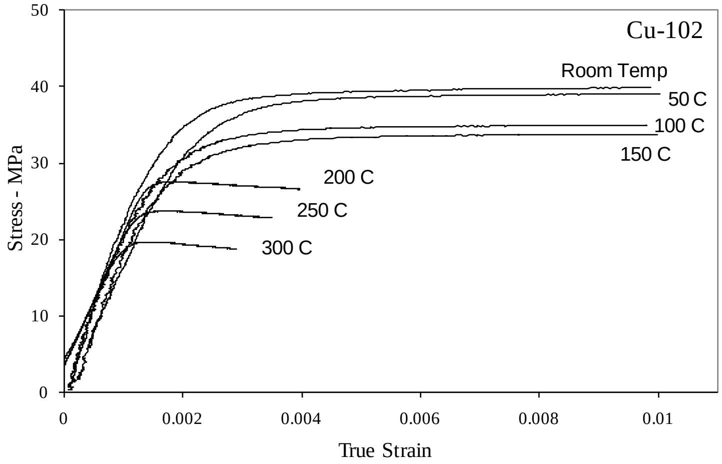

Figure AII-1. Stress-strain curves at constant temperature for Cu-102 (Watkins, 2005). The yield stress is found as the intercept of the 0.2% strain offset for each temperature.

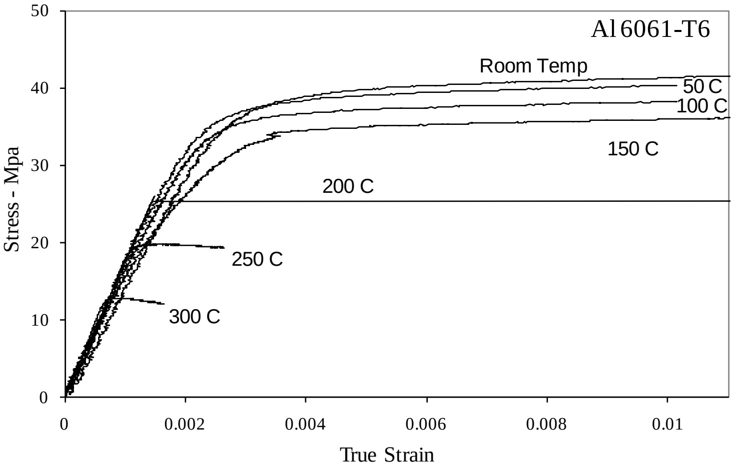

Figure AII-2. Stress-strain curves at constant temperature for Al 6061-T6 (Watkins, 2005). The yield stress is found as the intercept of the 0.2% strain offset for each temperature.

APPENDIX III: DEAD LOAD EXPERIMENTAL RESULTS

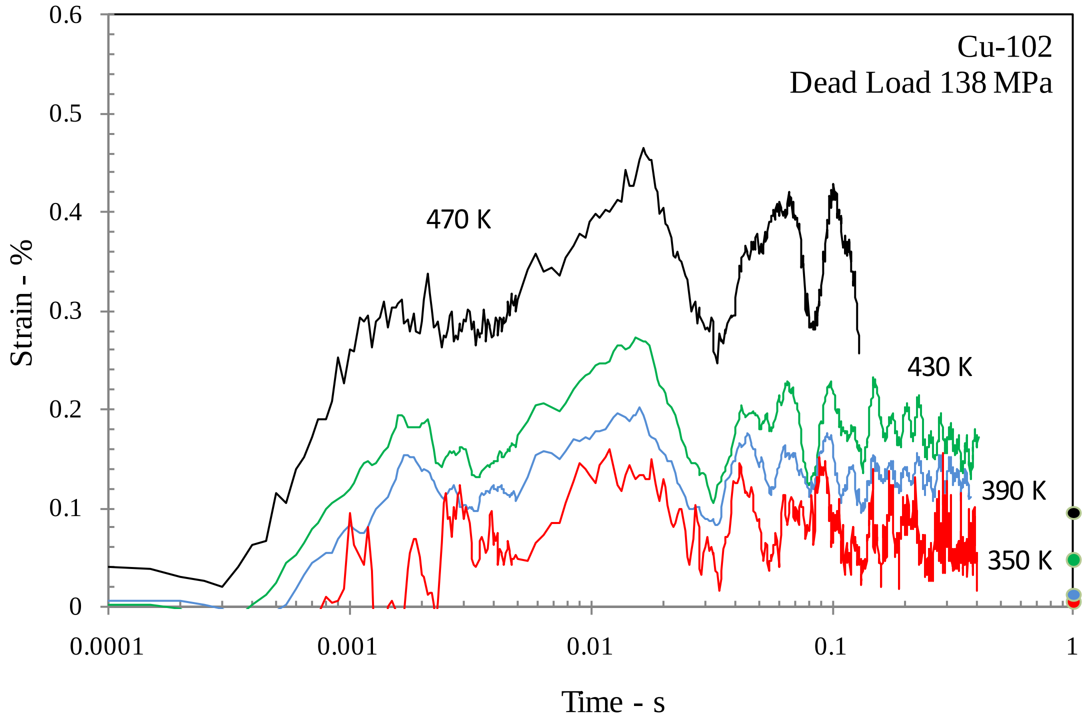

Figure AIII-1. Strain variation as a function of time as calculated from DIC; initial stress $\sigma_i = 138 \text{ MPa} < \sigma_Y$.

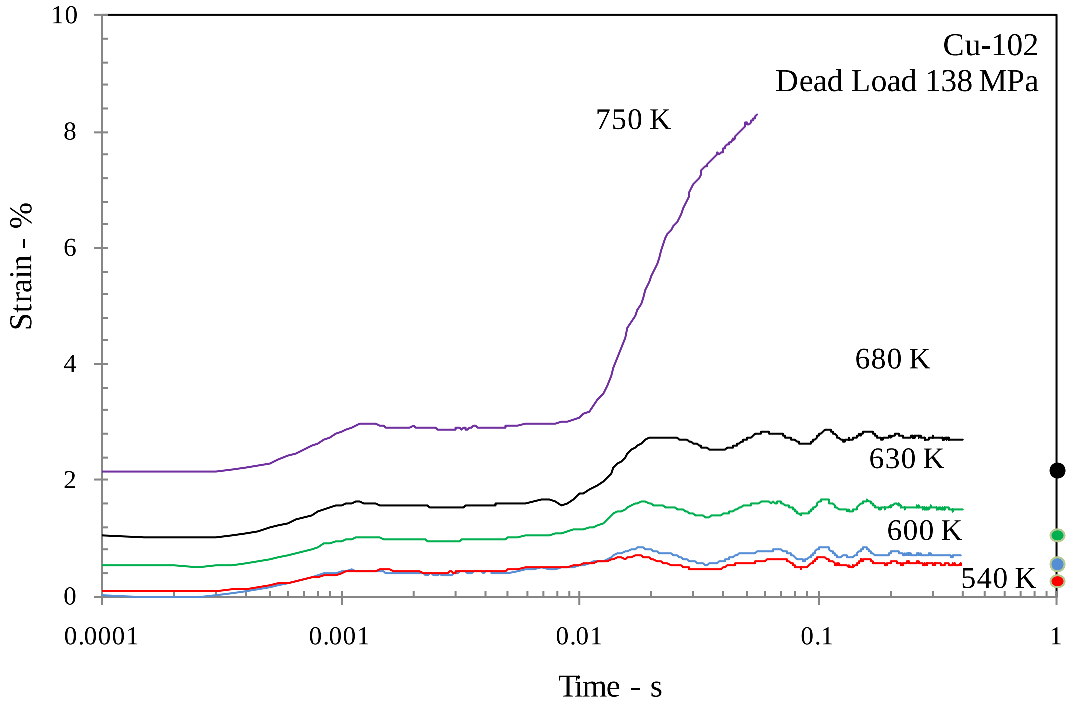

Figure AIII-2. Strain variation as a function of time as calculated from DIC; initial stress $\sigma_i = 138$ MPa $< \sigma_Y$.

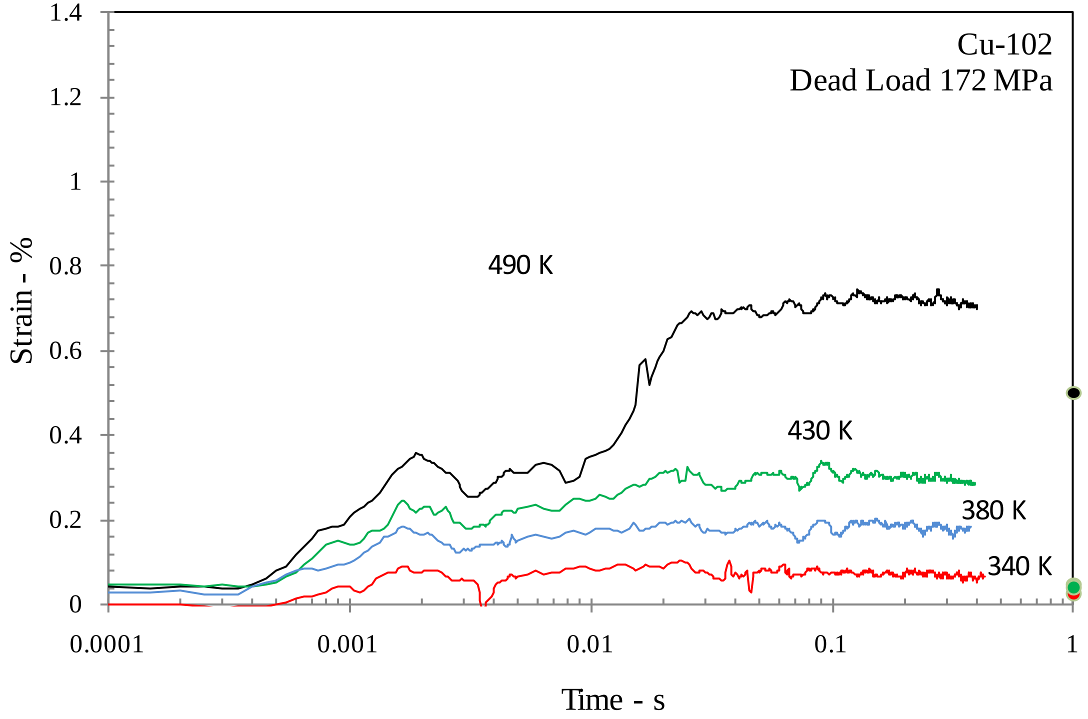

Figure AIII-3. Strain variation as a function of time as calculated from DIC; initial stress $\sigma_i = 192$ MPa $< \sigma_Y$.

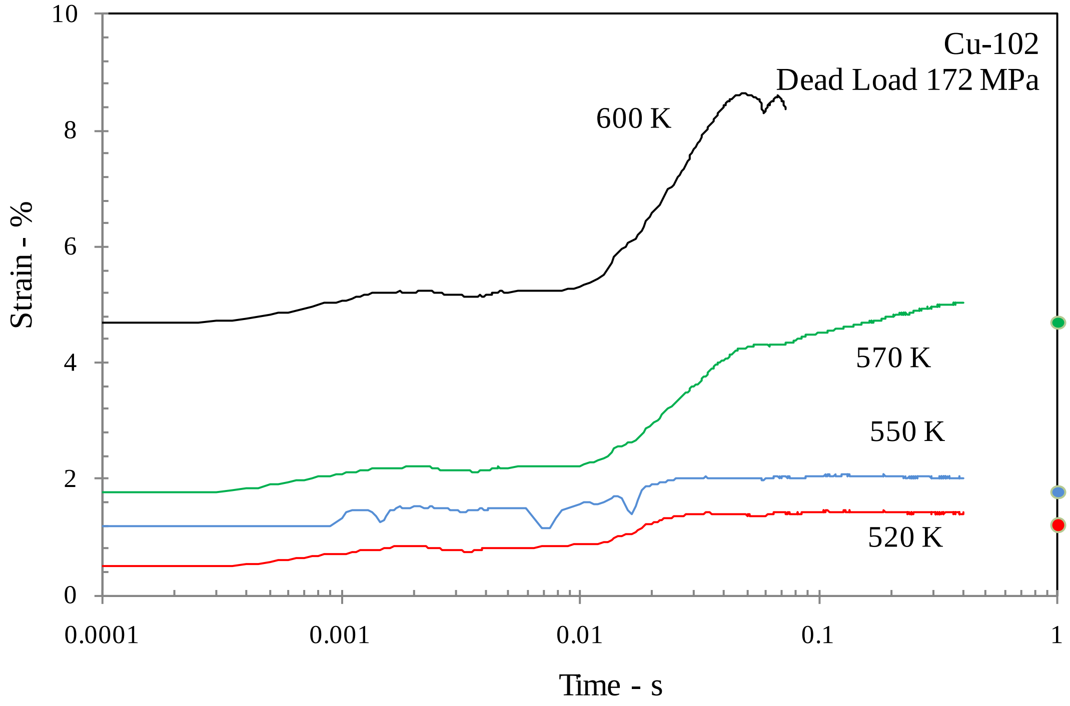

Figure AIII-4. Strain variation as a function of time as calculated from DIC; initial stress $\sigma_i = 192$ MPa $< \sigma_Y$.

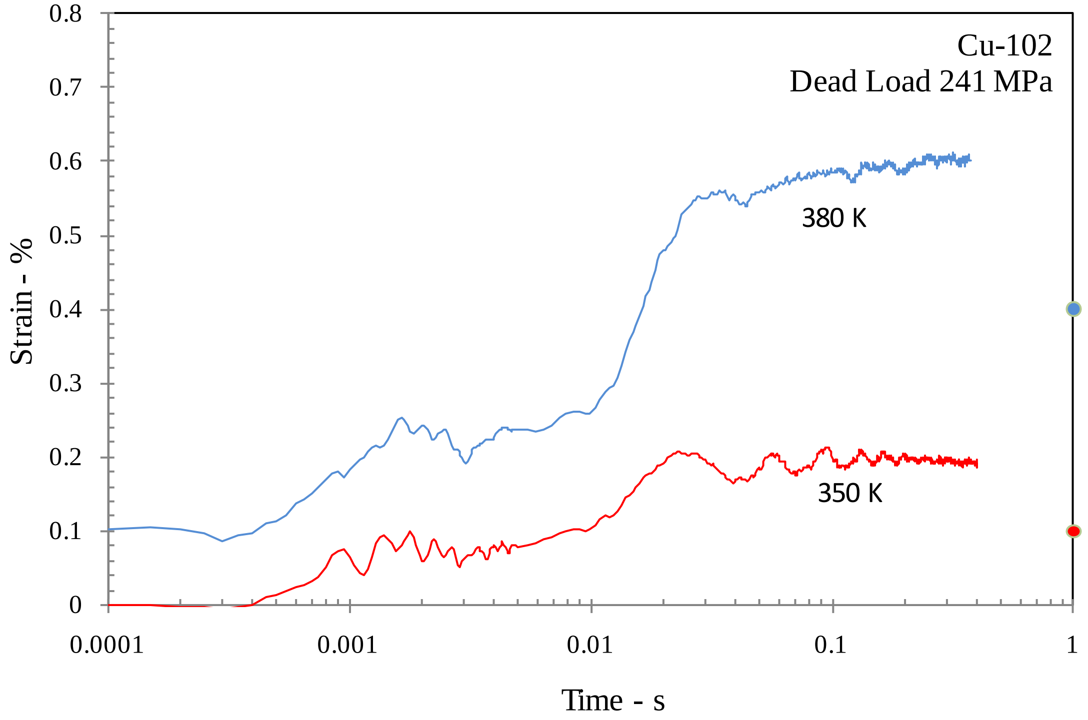

Figure AIII-5. Strain variation as a function of time as calculated from DIC; initial stress $\sigma_i = 241\,\text{MPa} < \sigma_Y$.

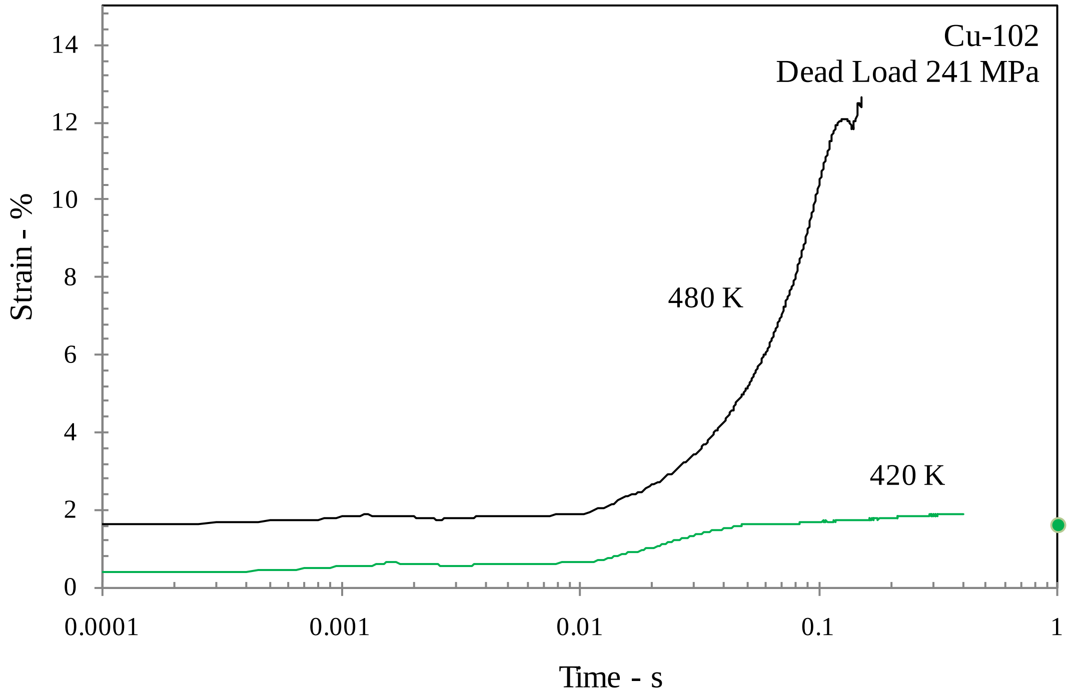

Figure AIII-6. Strain variation as a function of time as calculated from DIC; initial stress $\sigma_i = 241\,\text{MPa} < \sigma_Y$.

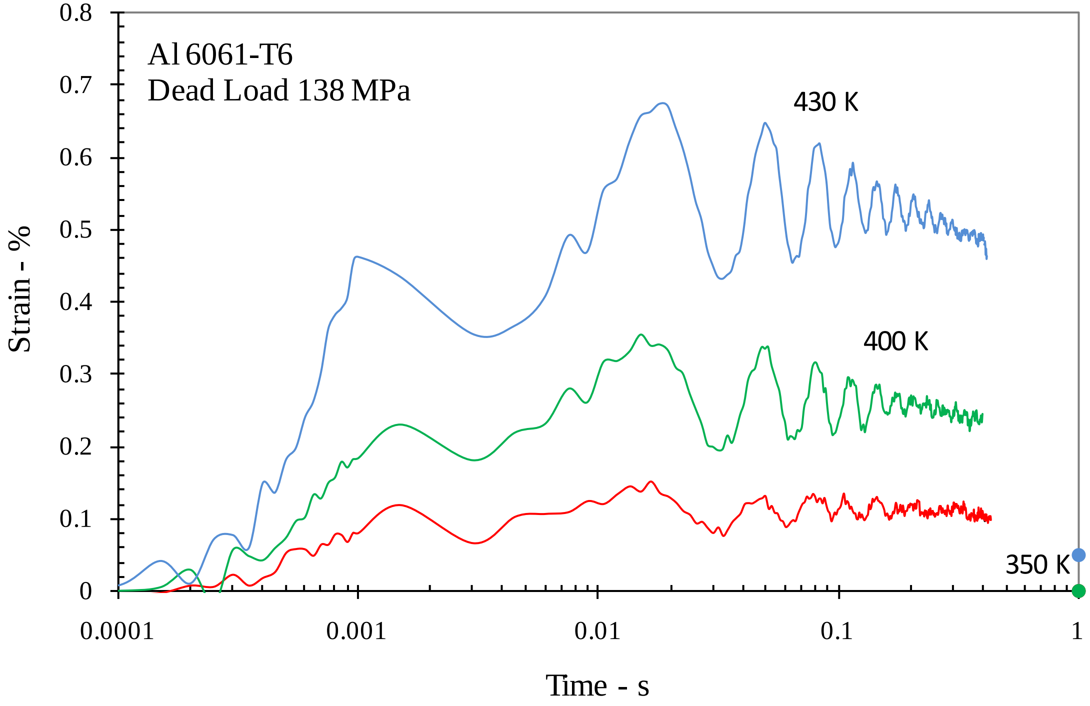

Figure AIII-7. Strain variation as a function of time as calculated from DIC; initial stress $\sigma_i = 138$ MPa $< \sigma_Y$.

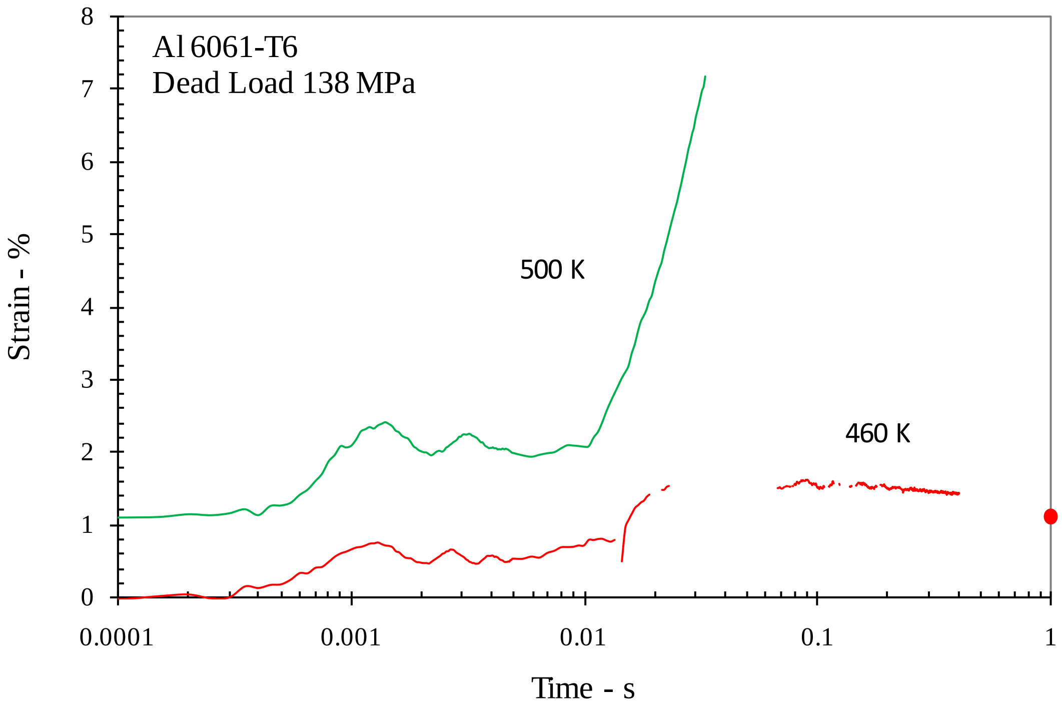

Figure AIII-8. Strain variation as a function of time as calculated from DIC; initial stress $\sigma_i = 138$ MPa $< \sigma_Y$.

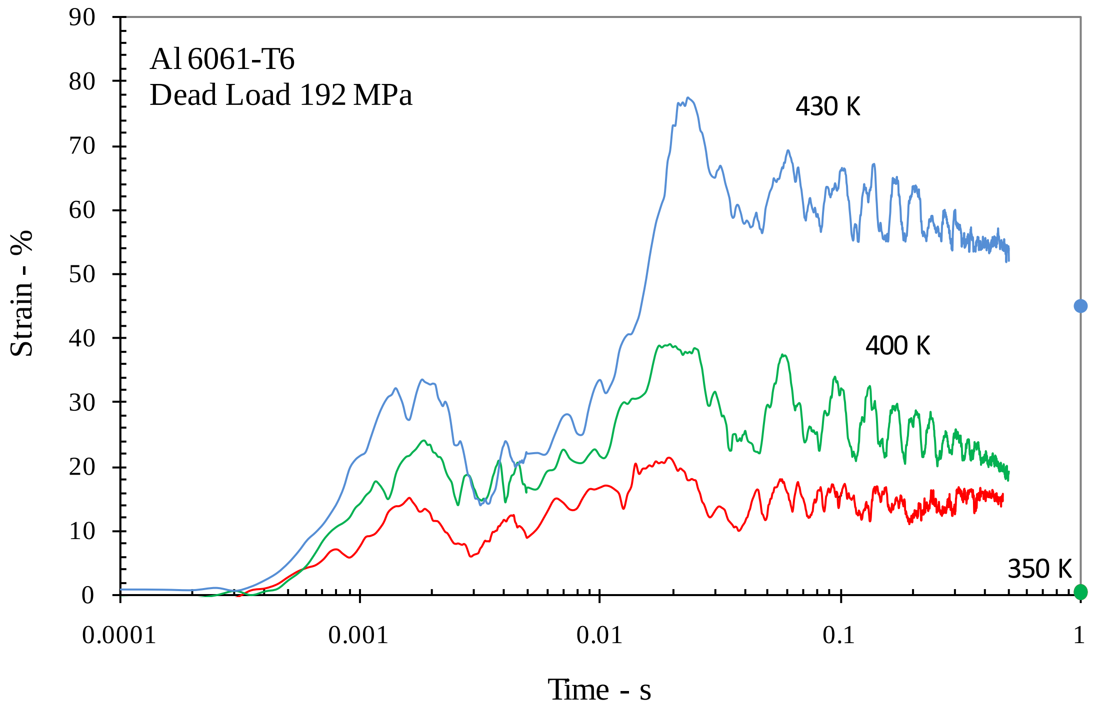

Figure AIII-9. Strain variation as a function of time as calculated from DIC; initial stress $\sigma_i = 192$ MPa $< \sigma_Y$.

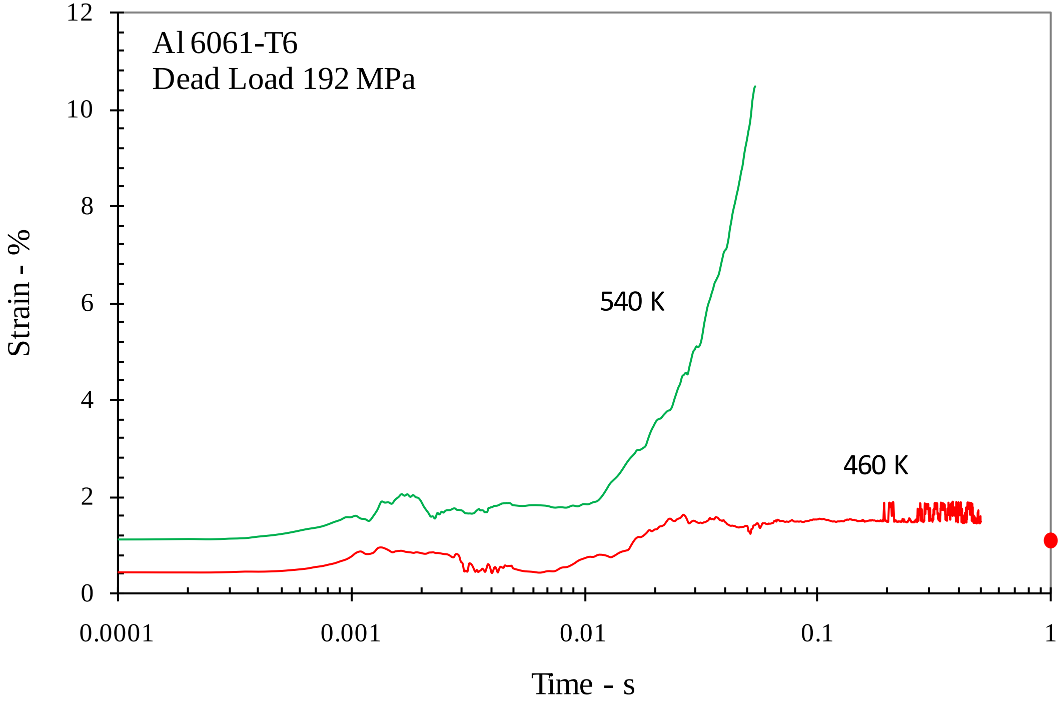

Figure AIII-10. Strain variation as a function of time as calculated from DIC; initial stress $\sigma_i = 192$ MPa $< \sigma_Y$.

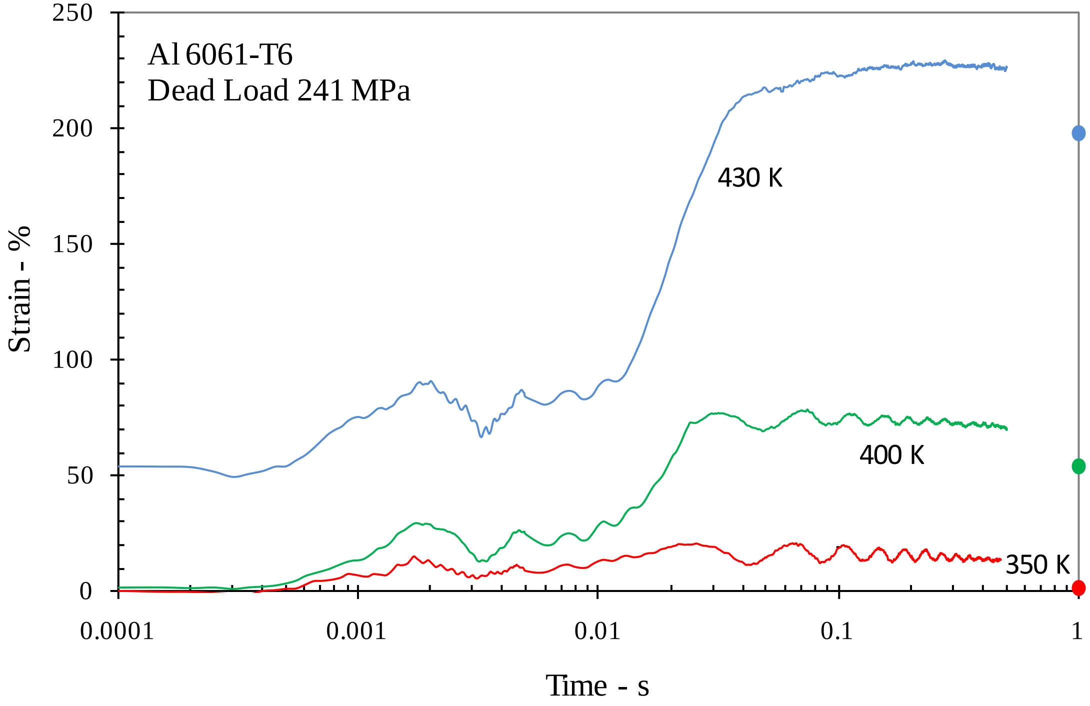

Figure AIII-11. Strain variation as a function of time as calculated from DIC; initial stress $\sigma_i = 241\,\text{MPa} < \sigma_Y$.

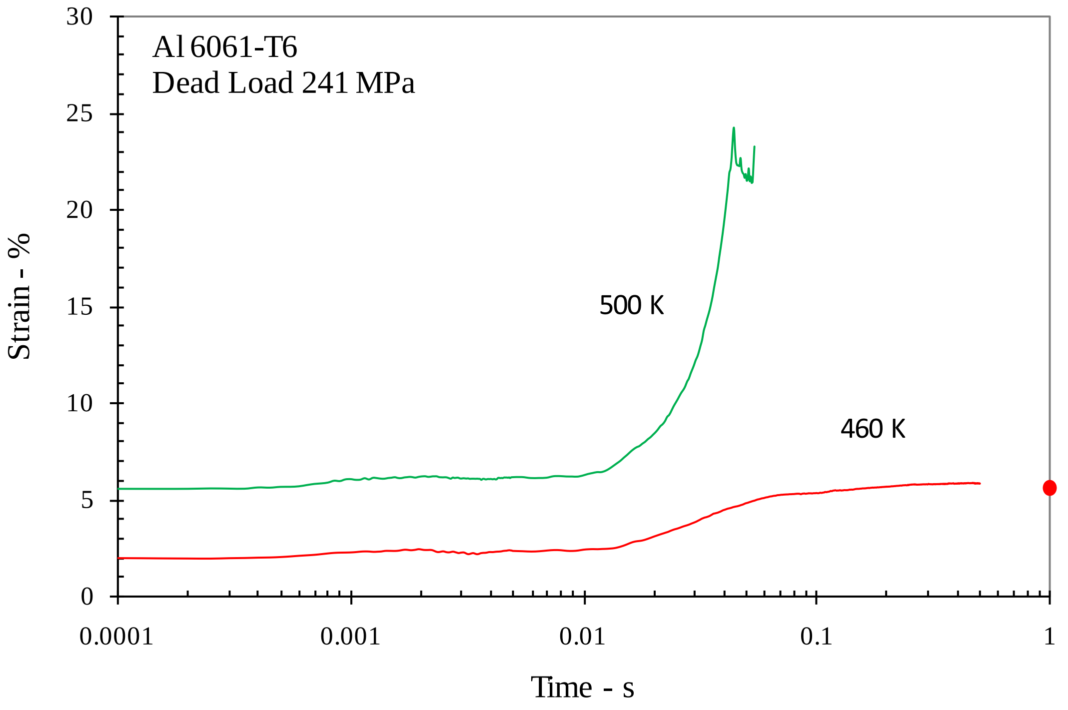

Figure AIII-12. Strain variation as a function of time as calculated from DIC; initial stress $\sigma_i = 241\,\text{MPa} < \sigma_Y$.

Bibliography

Bilyk, S.R., Ramesh. K.T.. and Wright, T.W., Finite deformations of metal cylinders subjected to electromagnetic fields and mechanical forces, *Journal of the Mechanics and Physics of Solids*, **53**, 2005, pp.525-544.

Cao, W., Sprecher, A.F. and Conrad, H., 1989, Effect of strain rate on the electro-plastic effect in Nb, *Scripta Metallurgica*, **23**, pp.151-155.

Conrad, H., 2002, Thermally activated plastic flow of metals and ceramics with an electric field or current, *Materials Science and Engineering*, **A322**, pp.100-107.

Doelp GGS, (1984), Experimental and numerical analysis of electric currents and electromagnetic blunting of cracks in thin plates. *MS Thesis, Cornell University.*

Finkel VM, Golovin YI, and Sletkov AA, (1977), Disintegration of a crack tip with a stron electromagnetic field, *Soviet Physics Doklady*, 22:683-685.

Galligan, J.M. and Pang, C.S. 1979, The electron drag on mobile dislocations in copper and aluminum at low temperatures-strain rate, temperature, and field dependence, *Journal of Applied Physics*, **50**, pp. 6253-6256.

Goldman, P.D., Motowidlo, L.R., and Galligan, J.M., 1981, The absence of an electroplastic effect in lead at 4.2K, *Scripta Metallurgica*, **15**, pp.353-356.

J. D. Jackson, (1978), Classical Electrodynamics, *Wiley Easter Limited.*

Kravchenko, V.Y., 1967, Effect of directed electron beam on moving dislocations, *Soviet Physics - JETP*, **24**, pp.1135-1142.

Landis CM, (2004), Energetically consistent boundary conditions for electromechanical fracture, *International Journal of Solids and Structures*, 41:6291-6315.

Okazaki, K., Kagawa, M., and Conrad, H., 1978, A study of the electroplastic effect in metals, *Scripta Metallurgica*, **12**, pp.1063-1068.

Okazaki, K., Kagawa, M., and Conrad, H., 1979a, Additional results on the electro-plastic effect in metals, *Scripta Metallurgica*, **13**, pp.277-280.

Okazaki, K., Kagawa, M., and Conrad, H., 1979b, Effects of strain rate, temperature and interestitial content on the electroplastic effect in titanium, *Scripta Metallurgica*, **13**, pp.473-477.

Okazaki, K., Kagawa, M., and Conrad, H., 1980, An evaluation of the contributions of skin, pinch and heating effects to the elctroplastic effect in titanium, *Materials Science and Engineering*, **45**, pp.109-116.

Mukherjee S, Morjaria MA, and Moon FC, (1982), Eddy current flows around cracks in thin plates for nondestructive testing, *Journal of Applied Mechanics*, 49:389-392.

NDT Resource Center, (Accessed 9/20/2010), www.ndt-ed.org/EducationResources/CommunityCollege/Materials/Physical_Chemical/Electrical.htm

Satapathy S, Stefani F, and Saenz A, (2005), Crack tip behavior under pulsed electromagnetic loading, *IEEE Transactions on Magnetics*, 41:226-230

Sutton M., (2008), Skin Effect, in Springer Handbook of Experimental Solid Mechanics, *Sharpe Editor*, (2008).

Silveira,V.L.A., Porto,M.F.S., Mannheimer,W.A., 1981, Electroplastic effect in copper subjected to low density electric current, *Scripta Metallurgica*, 15, pp.945-950.

Simmons RO and Baluffi RW, (1959), Measurements of the High-Temperature Electrical Resistance of Aluminum: Resistivity of Lattice Vacancies, *Physical Review*, 117:62-68.

Sprecher, A.F., Mannan, S.L., and Conrad, H., 1986, On the mechanisms for theelectroplastic effect in metals, *Acta Metallurgica*, **34**, pp.1145-1162.

Tada H, Paris PC and Irwin GR, (1973), The Handbook of Stress Intensity Factors, *Del Research Corporation*.

Tang, G., Zhang, J. Zheng, M., Zhang, J., Fang, W., Li, Q., 2000, Experimental study of electroplastic effect on stainless steel wire 304L, *Materials Science and Engineering*, **A281**, pp.263-267.

Timsit, R.S., 1981, Remarks on recent experimental observations of the electroplastic effect, *Scripta Metallurgica*, **15**, pp.461-464.

Troitskii, O.A. and Rozno, A.G., 1970, Electroplastic effect in metals, *Soviet Physics - Solid State*, **12**, pp. 161-166.

Tucker TJ and Toth RP (1975) EBW1: A Computer code for the prediction of the behavior of electrical circuits containing exploding wire elements, *Sandia National Laboratories Report* # SAND-75-0041.

Watkins, R., K. Ravi-Chandar and S. Satapathy, The mechanical behavior of conductors exposed to short-duration thermal loading, *IEEE Transactions on Magnetics*, **41**, 2005, pp.256-261.

Yao, K., Wang, J., Zheng, M., Yu, P., Zhang, H., 2001, A research on electroplastic effects in wire-drawing process of an austenitic stainless steel, *Scripta Meterialia*, **45**, pp.533-539.

Zhang TY, Wang T, and Zhao M, (2003), Failure behavior and failure criterion of conductive cracks (deep notches) in thermally depoled PZT-4 ceramics, *Acta Materialia*, 51:4881-4895.

Zhou, M., and Clifton, R.J., Dynamic ductile rupture under conditions of plane strain, *International Journal of Impact Engineering*, **19**, 1997, pp.189-206

Vita

Federico Gallo was born in Tradate, Italy on December 13, 1981 to Gisella Bassani and Flavio Gallo. He was raised in Gallarate, Italy. He attended Licieo Scientifico Viale dei Tigli in Gallarate where he developed a passion for motorcycles which led to his interest in engineering and science. He attended Politecnico di Milano in Milan where he discovered his enthusiasm for research and teaching. He graduated in July 2003 and attended the University of Texas as an exchange student for the 2003/2004 academic year. There he met his advisor, Dr. Ravi-Chandar, with whom he performed research on composite plates. Inspired by this collaboration, he entered the University of Texas Graduate program in engineering mechanics in January 2005. He received his MS in Engineering Mechanics in 2007 and his PhD in the same discipline in 2010.

Permanent address : 836 Melwood
Houston, Texas, 77009
United States of America
Chicco.ga@mail.utexas.edu

This dissertation was typed by Federico Gallo.